NANYANG
TECHNOLOGICAL
UNIVERSITY
SINGAPORE

HIERARCHICAL NANOSTRUCTURES INCORPORATED WITH DIFFERENT ENHANCEMENT STRATEGIES FOR IMPROVED PHOTOELECTROCHEMICAL PERFORMANCE

WANG ZHIWEI

SCHOOL OF MATERIALS SCIENCE AND ENGINEERING

2020

HIERARCHICAL NANOSTRUCTURES INCORPORATED WITH DIFFERENT ENHANCEMENT STRATEGIES FOR IMPROVED PHOTOELECTROCHEMICAL PERFORMANCE

WANG ZHIWEI

SCHOOL OF MATERIALS SCIENCE AND ENGINEERING

A thesis submitted to the Nanyang Technological University
in partial fulfilment of the requirement for the degree of
Doctor of Philosophy

2020

Statement of Originality

I hereby certify that the work embodied in this thesis is the result of original research, is free of plagiarised materials, and has not been submitted for a higher degree to any other University or Institution.

Jan-10-2020 Wang Zhiwei

Date Wang Zhiwei

Supervisor Declaration Statement

I have reviewed the content and presentation style of this thesis and declare it is free of plagiarism and of sufficient grammatical clarity to be examined. To the best of my knowledge, the research and writing are those of the candidate except as acknowledged in the Author Attribution Statement. I confirm that the investigations were conducted in accord with the ethics policies and integrity standards of Nanyang Technological University and that the research data are presented honestly and without prejudice.

Assoc Prof Alfred Tok

Jan-10-2020
. . . .
Date

. . . .
Alfred Tok Iing Yoong

Authorship Attribution Statement

This thesis contains material from 4 papers published in the following peer-reviewed journals in which I am listed as a first author.

Chapter 4 is published as Z. Wang, X. Li, C.K. Tan, C. Qian, A.C. Grimsdale, A.I.Y. Tok, *Appl. Surf. Sci*. **2019**, *470*, 800-806.
Chapter 5 is published as Z. Wang, G. Yang, C.K. Tan, T.D. Nguyen, A.I.Y. Tok, *Appl. Surf. Sci*. **2019**, *490*, 411-419.
Chapter 6 is published as Z. Wang, X. Li, H. Ling, C.K. Tan, L.P. Yeo, A.C. Grimsdale, A.I.Y. Tok, *Small* **2018**, *14*, 1800395.
Chapter 7 is published as Z. Wang, T.D. Nguyen, L.P. Yeo, C.K. Tan, L. Gan, A.I.Y. Tok, *Small* **2020**, *16*, 1905826.

The contributions of the co-authors are as follows:

- A/Prof Alfred Iing Yoong Tok provided guidance on the experimental design, data analysis, and manuscript preparation.
- I wrote the manuscript drafts. Dr. X. Li, Dr. H. Ling, Dr. G. Yang, Dr. L. Gan, Ms. L. P. Yeo, Ms. C.K. Tan, A/Prof A.C. Grimsdale assisted me in editing the manuscripts.
- I performed all the laboratory work and photoelectrochemical testings.
- I finished the material characterizations and analyzed the data.
- Dr. T.D. Nguyen helped me with TEM analysis.
- Ms. L. P. Yeo helped me with cross-sectional SEM testing.
- Mr. C. Qian helped me with Raman testing.

Jan-10-2020
Date

Wang Zhiwei
Wang Zhiwei

Abstract

Photoelectrochemical (PEC) water splitting makes it possible to harvest solar energy and then convert it to storable hydrogen fuel in a one-step reaction. As the product of hydrogen combustion is water, PEC water splitting offers enormous promise when it comes to reducing carbon emission. Since the investigation into PEC water splitting with TiO_2 thin films as the photoelectrode, various semiconductors with different nanostructures have been developed as photoelectrodes for enhanced PEC performance. An ideal PEC photoelectrode is characterized by an efficient visible absorption, quick charge collection ability, fast charge transfer and high photostability. As a single semiconductor cannot fulfill all of the requirements, several targeted strategies were thus proposed to satisfy more requirements. However, the incorporation of several targeted strategies into one nanostructure to achieve synergistic effects still remains a challenge due to uncertainties in the interaction between these strategies.

Herein, a series of hierarchical nanostructures were reported which incorporate different targeted strategies, such as elemental doping, enlarged surface area, heterojunction formation, surface protection, and increased light scattering ability. Through investigating the interactions between these targeted strategies, synergistic effects were achieved which contributed to an improved PEC performance. Firstly, the heterojunction formation and depressed interface charge recombination strategies were combined in a SnO_2 nanosheets (NSs)/TiO_2 thin film/CdS quantum dots (QDs). The introduced TiO_2 thin film fully covered the porous SnO_2 NSs and the bare FTO glass substrate, resulting in a depression in interface charge recombination. Besides, the introduced TiO_2 thin film has a proper band alignment with SnO_2 and CdS, which is beneficial to the formation of a heterojunction. Thus, porous SnO_2 NSs/TiO_2 thin film/CdS QDs showed a higher photocurrent in the low voltage area and a lower onset potential than SnO_2 NSs/CdS QDs. Secondly, the interaction between the surface area and light penetration was investigated in the WO_3 NSs/CdS nanorods (NRs)/amorphous TiO_2 film photoanode. The large space between adjacent WO_3 NSs provides sufficient areas for the secondary growth of 1D CdS NRs, which can increase the contact area with the electrolyte, favoring the oxidation process. However, excessive loading of CdS NRs occupies all the space, which ends up blocking light penetration to the bottom area. Through morphology tuning, a co-existence of CdS NRs and short CdS NRs on the surface of WO_3 NSs was achieved, reporting a higher photocurrent than pristine short CdS NRs and long CdS NRs. This enhancement results from achieving a balance between the amount of light penetration and the increased surface area. The photostability of CdS NRs is further improved by coating with a thin layer of amorphous TiO_2 film. Thirdly, the interaction between surface area and electron collection was also investigated in the hierarchical FTO inverse opals (IOs)/SnO_2 nanocrystals (NCs)/TiO_2 film photoanode. Although longer SnO_2 NCs can offer larger surface areas, short SnO_2 NCs have lower charge transfer resistance, resulting in better PEC performance. Finally, FTO IOs/CdS NRs/CdSe clusters were fabricated based on previous results. A co-existence of long CdS NRs and short CdS NRs were grown on FTO IOs, which were then coated with narrow bandgap CdSe clusters. Conductive 3D FTO IOs played the role of a quick electron collector, while CdS and CdSe acted as visible light absorbers for charge generation. The CdS/CdSe heterojunction further enhanced the charge separation. Furthermore, the unique 3D/1D hierarchical nanostructure enhanced light scattering ability and thus enabled higher light absorption. Due to the synergistic effects of these different components, FTO IOs/CdS NRs/CdSe clusters showed a higher photocurrent than pristine CdS NRs/CdSe clusters.

This work investigated the interaction between different targeted strategies and their influence on the PEC performance, providing useful guidance on the future fabrication of photoanodes for efficient PEC water splitting.

Lay Summary

In an electrical water splitting process, a minimum voltage of 1.23 V is required to drive oxygen evolution reaction (OER), while in the photoelectrochemical (PEC) water splitting process, a much lower potential can drive OER. The lower potential required is due to an extra photovoltage provided by the photoanode when illuminated with the sunlight. In this way, solar energy becomes involved in the water-splitting process to produce oxygen and hydrogen at the photoanode and the counter electrode, respectively. Solar energy is thus converted to storable hydrogen fuel, which is a high-density energy carrier. Besides, hydrogen fuel is an environment-friendly fuel alternative because the product of hydrogen combustion is simply water.

Photoanode is prepared with n-type semiconductors. However, the existing semiconductor materials cannot fulfill all the requirements of an ideal photoanode, such as high photostability, low cost, and high solar energy conversion efficiency. Thus, the modifications to existing semiconductor materials are proposed to satisfy these demands as much as possible. Several modification methods, such as elementary doping, heterojunction formation, and increasing surface area have been developed. Each technique can improve several properties of a semiconductor. Hence combining techniques should see a vast improvement in the photoanode properties, and thus a higher solar energy conversion efficiency can be achieved. However, these techniques are highly dependent on each other. Improving one property may cause a decrease in other properties. An understanding of the interaction between these techniques is the premise to improving the PEC performance of a photoanode.

This work is focused on investigating the interaction between different techniques through the fabrication of a series of hierarchical nanostructures for the incorporation of different techniques in one. The results showed that depressed interface charge recombination and heterojunction formation can be simultaneously achieved by introducing a thin film between SnO_2 nanosheets and CdS quantum dots. However, improving surface area could

exert a negative impact on electron collection and light penetration, which can be alleviated by morphology tunings. For example, the co-existence of long CdS nanorods and short CdS nanorods on the surface of WO_3 nanosheets yields better performance than only the existence of long CdS nanorods or short CdS nanorods, even though long CdS nanorods have higher surface area than short CdS nanorods. The excessive loading of SnO_2 nanocrystals on the FTO inverse opals could increase surface area, but it would result in the blocking of light penetration. Based on these results, a hierarchical 3D FTO inverse opals/1D CdS nanorods coated CdSe clusters was fabricated as a photoanode with the incorporation of four different techniques that can work synergistically in one nanostructure.

This work demonstrated that while the incorporation of different enhancement techniques in a photoanode may improve PEC performance, morphological tunings can also provide useful insights into the interaction between these techniques, which is essential for achieving of synergistic effects between different components in one photoanode and thus improve its PEC performance.

Acknowledgements

I would like to thank the NTU research scholarship for providing me a valuable chance to study in Singapore and MOE AcRF Tier 2 Grant for funding the chemicals, equipment, and other costs during my Ph.D. study.

Sincere gratitude is conveyed to my supervisor Associate Professor Alfred Iing Yoong Tok. Not only did he provide me with a precious chance to pursue my Ph.D. degree, his gracious manners, sharp insight, and professional guidance helped me greatly in overcoming the challenges and difficulties I faced during my Ph.D. study.

I am very grateful for the suggestions provided by Professor Fan Hongjin and Associate Professor Andrew Clive Grimsdale. Furthermore, a big thank you to all the technicians in our school who provided me with essential equipment training and administrative support.

I would like to thank all my group members. They provided me much useful advice and help on materials characterizations. Dr. Nguyen Duy Tam assisted me in TEM analysis, Dr. Liu Xueyang imparted me the knowledge about hydrothermal reaction, Dr. Li Xianglin taught me the operation of ALD, Dr. Yang Guang, Dr. Gan Lin, Dr. Ling Han, Dr. Manju, Ms. Yeo Loo Pin, Ms. Tan Chiew Kei, Ms. Harpaz Dorin, Mr. Sharma Antareep, and Ms. Zhang Xiaoyu provided me with a lot of suggestions and help on my Ph.D. study. Ms. Yeo Loo Pin and Ms. Tan Chiew Kei also improved the quality of the English for all my manuscripts.

I am also grateful to Dr. Chen Chen, Dr. Chen Benson, Dr. Dai Zhengfei, Dr. Zheng Penglun, Dr. Wang Jie, Dr. Hu Hongwei, Dr. Chen Binbin, Dr. Zhang Zhuo, Dr. Zhang Mengyuan, Dr. Zhao Xin, Mr. Cao Xun, Mr. Qian Chen, Mr. Khang Ngoc Dinh and Ms. Sun Lan for their help on various measurements.

Finally, I would like to express my heartfelt thanks to my family. They gave me the courage and motivation to complete my Ph.D. study. I would also like to thank all my friends in Singapore. The joyful moments come and go, but the good memories stay forever.

Table of Contents

Chapter 3 Experimental Methodology

Chapter 6 3D FTO IOs/SnO_2 NCs/TiO_2 Composite Photoanode for Efficient Photoelectrochemical Water Splitting 91

Chapter 7 Periodic FTO IOs/CdS NRs/CdSe Clusters with Superior Light Scattering Ability for Improved Photoelectrochemical Performance 111

Table Captions

Figure Captions

Figure 3.2 Schematic shown for the forced impregnation method for the fabrication of inverse opals. (a) PS microspheres; (b) PS colloidal crystals; (c) PS colloidal crystals soaked into the methanol solution; (d) connect with a vacuum pump; (e) infiltration of precursors; (f) inverse opals. Reprinted with permission from X. Chen, Z. Li, J. Ye, Z. Zou, Chem. Mater. 22 (2010) 3583-3585. Copyright (2010) American Chemical Society.

Figure 3.3 Schematic shown for the ALD process. Reprinted with permission from L. Wen, M. Zhou, C. Wang, Y. Mi, Y. Lei, Adv. Energy Mater. 6 (2016) 1600468. Copyright (2016) John Wiley& Sons, Inc.

Figure 3.4 (a) Interaction between the specimen and the electron beam; (b) Schematic shown for the SEM. Reprinted with permission from Ni. C, Scanning electron microscopy (SEM). in: Wang Q.J., Chung YW. (eds) Encyclopedia of tribology. Springer, (2013), pp. 2977-2979. Copyright (2013) Springer.

Figure 3.5 (a) Generation of characteristic X-ray photons; (b) Typical EDS characterization results. Reprinted with permission from B. Inkson, Scanning electron microscopy (SEM) and transmission electron microscopy (TEM) for materials characterization, in: Materials characterization using nondestructive evaluation (NDE) methods, Elsevier, 2016, pp. 17-43. Copyright (2016) Elsevier.

Figure 3.6 Schematic shown for TEM. (a) Diffraction mode; (b) Image mode. Reprinted with permission from F.L. Deepak, E. Anumol, J. Li, Advanced electron microscopy techniques toward the understanding of metal nanoparticles and clusters, in: Metal nanoparticles and clusters, Springer, 2018, pp. 219-287. Copyright (2018) Springer.

Figure 3.7 Schematic shown for HRTEM. (a) Diffraction mode; (b) Image mode. Reprinted with permission from E. Abe, E. Abe, Chem. Soc. Rev. 41 (2012) 6787-6798. Copyright (2012) Royal Society of Chemistry.

Figure 3.8 Schematic shown for XRD. Reprinted from R. Gilles, D. Mukherji, M. Hoelzel, P. Strunz, D. Toebbens, B. Barbier, Acta Mater. 54 (2006) 1307-1316. Copyright (2006), Elsevier.

Figure 3.9 Photoelectron effect. Reprinted from R. Gilles, D. Mukherji, M. Hoelzel, P. Strunz, D. Toebbens, B. Barbier, Acta Mater. 54 (2006) 1307-1316. Copyright (2006), with permission from Elsevier.

Figure 4.1 Schematic illustration for the fabrication process of the SnO_2 NSs/TiO_2/CdS QDs.

Figure 4.2 SEM images of: (a) SnO_2 NSs prepared with $SnCl_4$ (40 mg) and C_2H_5NS (40 mg); (b) SnO_2 NSs prepared with $SnCl_4$ (80 mg) and C_2H_5NS (80 mg), (c) SnO_2 NSs prepared with $SnCl_4$ (100 mg) and C_2H_5NS (100 mg); (d) SnO_2 NSs with high magnification; (e) SnO_2 NSs/TiO_2, (f) SnO_2 NSs/TiO_2/CdS QDs.

Figure 4.3 EDS characterization of SnO_2 NSs/TiO_2/CdS QDs.

Figure 4.4 (a) XRD patterns of FTO substrate, SnO_2 NSs, SnO_2 NSs/TiO_2 and SnO_2 NSs/TiO_2/CdS QDs; (b) Raman spectra of FTO substrate, SnO_2 NSs; (c) Raman spectra of SnO_2 NSs/TiO_2 and SnO_2 NSs/TiO_2/CdS QDs; (d) UV-Vis absorbance of SnO_2 NSs/TiO_2 and SnO_2 NSs/TiO_2/CdS QDs.

Figure 4.5 (a) Linear sweep voltammetry measurement of SnO_2 NSs/TiO_2, SnO_2 NSs/CdS QDs and SnO_2 NSs/TiO_2/CdS QDs; (b) Linear sweep voltammetry measurement of SnO_2 NSs/TiO_2, SnO_2 NSs/CdS QDs and SnO_2 NSs/TiO_2/CdS QDs under chopped light illumination.

Figure 4.6 (a) Scheme of band alignment and charge transfer process in the SnO_2 NSs/TiO_2/CdS QDs photoanode. The bandgap of CdS, TiO_2 and SnO_2 are 2.4 eV, 3.2 eV

NS arrays, CdS-NR arrays, and WO_3-NS/CdS-NR arrays. Inset in (d) shows the equivalent circuit.

Figure 5.9 IPCE of WO_3-NS arrays, CdS-NR arrays and WO_3-NS/CdS-NR arrays.

Figure 5.10 (a) Schematic of the formation of a type-II heterojunction between CdS and WO_3; (b) Schematic of the PEC water splitting process in WO_3-NS/CdS-NR arrays photoanode.

Figure 5.11 (a) TEM image of WO_3-NS/CdS-NR arrays/TiO_2-20 cycles. The inset is the HRTEM image of WO_3-NS; (b) TEM image of single CdS-NR coated with 20 ALD cycles of TiO_2. The inset is the HRTEM image of CdS-NR; (c) Linear sweep curves of WO_3-NS/CdS-NR arrays with different ALD cycles of TiO_2; (d) Photostability test of WO_3-NS/CdS-NR arrays and WO_3-NS/CdS-NR arrays/TiO_2-20 cycles.

Figure 5.12 XRD and SEM characterizations of WO_3-NS/CdS-NR arrays/TiO_2 after stability test.

Figure 6.1 Schematic diagram for the fabrication of the FTO IOs/SnO_2 NCs/TiO_2.

Figure 6.2 Top-view SEM images of: (a) FTO IOs; (b)-(d) FTO IOs/SnO_2 NCs; (e) FTO IOs/SnO_2 NCs/TiO_2; (f) Cross-section view of FTO IOs/SnO_2 NCs/TiO_2.

Figure 6.3 EDS of FTO IOs/SnO_2 NCs/TiO_2.

Figure 6.4 (a) TEM image of FTO IOs/SnO_2 NCs/TiO_2; (b) The HRTEM image of FTO IOs/SnO_2 NCs/TiO_2, the inset in (b) shows the SAED patterns; (c) XRD of FTO IOs/SnO_2 NCs and FTO IOs/SnO_2 NCs/TiO_2; (d) Raman spectra of FTO IOs/SnO_2 NCs and FTO IOs/SnO_2 NCs/TiO_2.

Symbols and Abbreviations

ALD	Atomic Layer Deposition
CB	Conduction Band
CdS	Cadmium Sulfide
CdSe	Cadmium Selenide
DI	Deionized
EDS	Energy Dispersive X-ray Spectroscopy
EIS	Electrochemical Impedance Spectroscopy
FTO	Fluorine-doped Tin Oxide
HER	Hydrogen Evolution Reaction
HRTEM	High-Resolution Transmission Electron Microscopy
IOs	Inverse Opals
IPCE	Incident-Photon-to-Current Conversion Efficiency
LSV	Linear Sweep Voltammetry
NBs	Nanobowls
NRs	Nanorods
NWs	Nanowires
NCs	Nanocrystals
OCVD	Open Circuit Voltage Decay
OER	Oxygen Evolution Reaction
PEC	Photoelectrochemical
PS	Polystyrene
RHE	Reversible Hydrogen Electrode
SEM	Scanning Electron Microscopy
STEM	Scanning Transmission Electron Microscope
SILAR	Successive Ionic Layer Adsorption and Reaction
TCOs	Transparent Conducting Oxides
TEM	Transmission Electron Microscopy
VB	Valence Band
XRD	X-ray Diffraction

XPS	X-ray Photoelectron Spectroscopy

E_{CB}	Lowest edge of conduction band
E_{VB}	Highest edge of valence band
E_{FB}	Flat band potential
E_F	Fermi level
E_g	Band gap
η_{abs}	Light absorption efficiency
η_{sep}	Charge separation efficiency
η_{trans}	Charge transfer efficiency

Chapter 1

Introduction

In this chapter, the research background of photoelectrochemical (PEC) water splitting is introduced, followed by the description of a typical PEC cell. The factors that restrict the photocurrent as well as some targeted strategies for the enhancement of photocurrent are elaborated. Then, a hypothesis about the improved PEC performance is proposed. The objective, scopes, and overview of this dissertation are also presented here. Finally, a summary of the findings is listed.

1.1 Research Background

Energy plays an indispensable role in modern society, enabling rapid economic development and industrial advancement. However, the majority of energies used in human society are non-renewable fossil fuels. The reliance upon fossil fuels not only brings about severe environmental pollutions in the current community but will also result in energy shortages in the foreseeable future.[1] Since renewable solar energy received by the land is 3.6 x 10^5 Terawatts per year, which far exceeds the predicted global energy consumption by humankind in 2050 (36 Terawatts per year), providing a promising solution to tackle with both energy crises and environmental pollution.[2] The utilization of solar energy in the form of electrical and thermal energy has already been put into commercial application. However, due to cost and technical constraints, the application of solar power still lagged far behind that of fossil fuels.[3] Photoelectrochemical (PEC) water splitting is considered as a promising technology to acquire hydrogen fuel through the direct conversion of solar energy. Hydrogen fuel is a storable high energy-per-mass energy carrier as well as an essential industry raw material. Furthermore, the main combustion product of hydrogen is water, which can significantly reduce carbon emission and smog formation.[4, 5]

1.2 PEC Cell

Fujishima and Honda conducted the pioneering investigation into PEC water splitting in 1972 by using TiO_2 thin films as the photoelectrode.[6] Following that, numerous researches were devoted to the development of novel materials and nanostructures as photoelectrodes for enhanced PEC performance.[7, 8] In a PEC device, photoanodes fabricated with an n-type semiconductor can achieve the light absorption and oxygen evolution reaction (OER) of water, while photocathodes prepared with p-type semiconductors are used for hydrogen evolution reaction (HER).[1, 9] Since OER is more demanding compared to HER due to the involvement of a four electrons reaction, most research is focused on the oxidation reaction.[10] In this case, the photocathode will be replaced with metal electrodes, such as

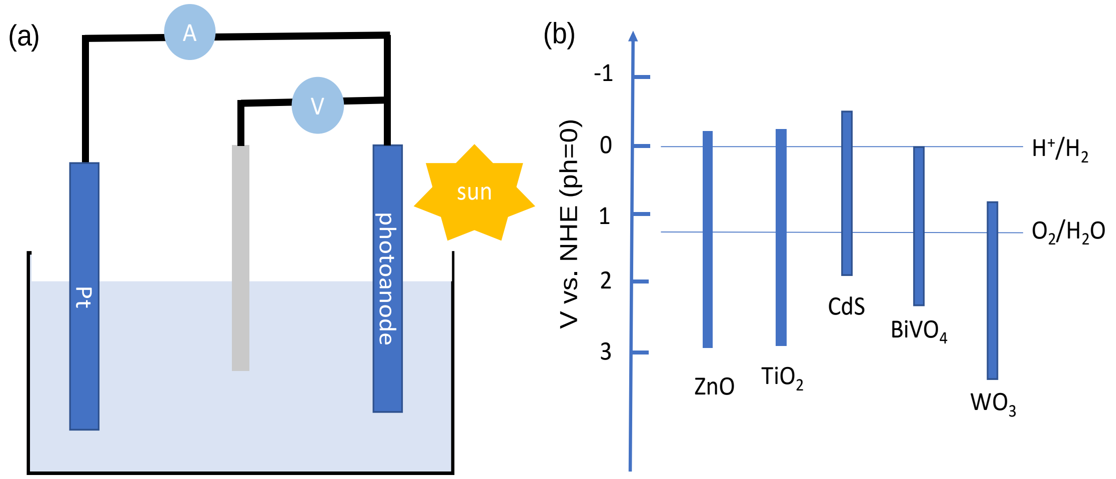

Figure 1.1 (a) Schottky type PEC cell, (b) band edge position of typical photoanode materials.

Pt, to ensure a highly efficient reduction reaction in what is known as a Schottky type PEC cell (Figure 1.1(a)). A typical PEC water splitting process involves charge generation, separation, and transfer. Specifically, (i) the photoanode absorbs the incident light and generates holes and electrons. (light absorption). (ii) The photogenerated holes and electrons are separated due to band bending and then transported towards the surface of the photoanode and counter electrode, respectively (charge separation). (iii) Holes are finally transferred to the photoanode surface for OER. At the same time, electrons are involved in the HER on the counter electrode (charge transfer).[11-13] The PEC performance of a photoanode could be evaluated by measuring water oxidation photocurrent (J_{H2O}), which is determined by the charge transfer efficiency (η_{trans}), charge separation efficiency (η_{sep}), and light absorption efficiency (η_{abs}).[14, 15]

$$J_{H_2O} = J_{max} \times \eta_{abs} \times \eta_{sep} \times \eta_{trans} \qquad (1)$$

J_{max} is determined by the bandgap of a semiconductor. A lower bandgap gives a higher J_{max}. However, the overall water splitting requires G=237.2 kJ mol^{-1} (Gibbs free energy) to produce one mole of hydrogen, corresponding to the bandgap of 1.23 eV, as indicated by the following equations.[11]

$$Semiconductor \overset{hv}{\rightarrow} e_{cb}{}^{-} + h_{vb}{}^{+} \qquad (2)$$

$$e^- + H^+ \rightarrow \frac{1}{2}H_2 \quad E^0_{H^+/H_2} = 0\ V\ vs.RHE \tag{3}$$

$$2h^+ + H_2O \rightarrow \frac{1}{2}O_2 \quad E^0_{O_2/H_2O} = 1.23\ V\ vs.RHE \tag{4}$$

$$H_2O \rightarrow H_2 + \frac{1}{2}O_2\ \ \Delta E = 1.23\ V\ vs.RHE \tag{5}$$

Considering the requirement of overpotential of OER and kinetic limitation, the minimum bandgap should be around 1.8-2.0 eV.[16] Since water splitting is not a thermodynamically favorable process, only when the valence and conduction band edges of a semiconductor straddle redox potential E(H^+/H_2) and E(H_2O/O_2), water splitting could be spontaneously promoted.[17] The bandgap and band edges of some typical semiconductors are shown in Figure 1.1(b). η_{abs} could be increased by prolonging the optical path. A large thickness or higher scattering ability can bring about a longer optical path and thus a higher η_{abs}.[18] η_{sep} is restricted by the bulk charge recombination and interface charge recombination. Severe bulk charge recombination is frequently caused by poor conductivity of majority carrier or short hole diffusion length of the semiconductors, which can be overcome by the enhancement of the electrical conductivity or a decrease in film thickness. The interface charge recombination that occurs on the substrate/semiconductor interface can be attributed to the injection of electrons from the substrate to the electrolyte.[19] η_{trans} is mostly hindered by sluggish OER kinetics of semiconductors or surface charge recombination induced by surface states.[20]

1.3 Targeted Strategies For Improved PEC Performance

Based on the above analysis, an ideal photoanode material should fulfill some basic requirements, such as efficient visible light absorption, high carrier mobility, fast OER kinetics, suitable band edge, long photostability, and low cost and toxicity.[21, 22] However, a single existing semiconductor material can not fulfill all these requirements to date.[23] Apart from exploring new materials, several targeted strategies were proposed to enhance the PEC performance of some existing materials. For example, the carrier mobility can be enhanced by doping with other elements or through the introduction of a conductive skeleton.[24, 25] Semiconductors with a large bandgap can be coated with visible light sensitizers or doped with other ingredients to narrow their bandgap for visible absorption.[26, 27] An ultrathin passivation and protection layer could enhance the photostability and reduce the surface states.[28] The OER kinetics can be accelerated by the incorporation of co-catalyst.[29] Nanostructure engineering of semiconductors can also bring about various advantages, such as the reduction of length for holes diffusion and simultaneously maintain the thickness required for efficient light absorption.[1] Other benefits, such as increased specific surface areas, strong light scattering ability, can also be achieved by the construction of different dimensional nanostructures.[30] Recently, the creation of hierarchical nanostructures with different dimensional nanostructures was considered a possible route to incorporate several targeted strategies into one nanostructure, and thus fulfill more of the requirements of an ideal photoanode.[31-33] However, the interaction between different strategies in one hierarchical nanostructure still needs further investigation to achieve the synergistic effects.

1.4 Hypothesis

Different targeted strategies could be incorporated into one hierarchical nanostructure to enhance its surface area, light absorption or charge collection ability. However, these targeted strategies are constrained by each other. Morphology tuning can be used to optimize different targeted strategies to achieve enhanced PEC performance.

1.5 Objectives and Scope

In this thesis, a series of hierarchical structures will be fabricated for the incorporation of different targeted strategies together. Morphology tuning will be used to investigate the interaction between these strategies. Finally, the optimization of these targeted strategies should be achieved to obtain improved PEC performance. The scope of this thesis is listed below.

a. Highly porous SnO_2 nanosheet arrays (NSs) sandwiched within TiO_2 film and CdS quantum dots (QDs). A two-dimensional (2D) porous SnO_2 NSs/0D CdS QDs hybrid nanostructure was prepared by a combination of hydrothermal reaction and successive ionic layer adsorption and reaction. As the fabrication of SnO_2 nanosheet arrays does not require the seed layer, some areas of bare FTO glass were exposed to the electrolyte, inducing severe interface charge recombination. A TiO_2 thin film was introduced between SnO_2 NSs and CdS QDs. The influence of the introduced TiO_2 thin film on photocurrent was tested by linear sweep voltammetry (LSV) measurement. Higher photocurrent in the low voltage area and lower onset potential were observed after the introduction of TiO_2 thin film. The uniform coating of TiO_2 thin film by ALD insulated bare FTO surface from the electrolyte. Besides, the contribution of the heterojunction between CdS, SnO_2 and TiO_2 was investigated. In this hybrid nanostructure, heterojunction formation and depressed interface charge recombination strategies were achieved by the simple introduction of TiO_2 thin film between CdS NSs and CdS QDs.

b. Amorphous TiO_2 coated hierarchical WO_3 NSs/CdS nanorods (NRs). Increasing the specific surface area is a useful method to increase the PEC performance. 1D CdS NRs were grown on the surface of 2D WO_3 NSs to form a hierarchical nanostructure. The length and amount of CdS NRs were controlled by the change in hydrothermal growth duration and confirmed by SEM characterization. The short CdS NRs with an average length of 50 nm, a co-existence of short CdS NRs and long CdS NRs (400 nm), and even longer CdS NRs (~1μm) were obtained on the surface of WO_3 NSs. The photocurrent of these samples were tested. A higher photocurrent was found in samples with the co-existence of short CdS NRs and long CdS NRs. The connection between the photocurrent, morphology and light penetration was analyzed. Finally, an ultra-thin layer of amorphous TiO_2 layer was introduced on the hierarchical nanostructure, which was then characterized by Transmission Electron Microscopy. The impact of the amorphous TiO_2 layer on photocurrent and photostability was investigated. In this hybrid nanostructure, heterojunction formation, surface protection, and an increase in surface area were incorporated and the interaction between surface area and light penetration was investigated.

c. FTO inverse opals (IOs)/SnO_2 nanocrystals (NCs)/TiO_2 thin film. Porous three-dimensional FTO IOs offer a high surface for secondary growth of photoactive material and multiple light scattering inside the structure, thus acting as an efficient conductive scaffold for the fabrication of hierarchical nanostructures. Herein, SnO_2 NCs were grown on the surface of FTO IOs to achieve a 3D/1D hierarchical nanostructure. The photoactive TiO_2 layer was then coated with the hierarchical nanostructure by a stop-flow ALD mode in order to enhance light absorption. The loading amount of SnO_2 NCs was tuned by changing the precursor concentration, while the length of SnO_2 NCs was tuned according to pH value. The influence of loading amount and length on photocurrent, charge transfer resistance and light absorption was measured. Through morphology tuning, the interaction between the surface area, light absorption, and charge transfer could be investigated. The targeted strategies, including the conductive skeleton, enlarged surface area, increased light scattering, were incorporated in this hybrid nanostructure.

d. Periodic FTO IOs grafted with CdS NRs/CdSe clusters. In a previous study, 3D IOs/0D NCs hierarchical nanostructure was used as a scaffold. To further increase surface area and light scattering ability, photoactive 1D CdS NRs/CdSe clusters were coated on 3D FTO IOs to form a novel hierarchical nanostructure. The co-existence of long CdS NRs and short CdS NRs on the FTO IOs was conceptualized based on previous results. CdSe clusters were then coated on the surface of CdS NRs, which could increase the light absorption range and achieve a heterojunction with CdS. The light scattering abilities of FTO IOs/CdS NRs/CdSe clusters and pristine CdS NRs/CdSe clusters were compared. The introduction of FTO IOs on the flat potential, electrical active surface area, and carrier density was investigated. The enhancement strategies, including heterojunction formation, conductive skeleton, enhancement of light scattering, enhanced visible light absorption, were incorporated in this hybrid nanostructure.

1.6 Dissertation Overview

The thesis is focused on the development of novel hierarchical nanostructures that can incorporate several enhancement strategies together. The interaction between different strategies was also investigated through tuning the components in the hierarchical nanostructure.

Chapter 1 Introduces the background of PEC water splitting, the factors that restrict the PEC performance and the corresponding enhancement strategies and the rationale for the development of hierarchical nanostructures. The hypothesis, scope, outlines and outcomes are also presented in chapter 1.

Chapter 2 is a literature review. The basic concepts related to PEC water splitting are elaborated. Then, the properties of some conventional semiconductors are presented. Finally, the fabrication and development of hierarchical nanostructures for PEC applications are reviewed and summarized.

Chapter 3 describes the principles of different fabrication methods and the application of these methods for the preparation of various nanostructures. The mechanism of typical materials characterization methods is also presented in the chapter.

Chapter 4 is focused on 2D SnO_2 NSs/TiO_2 thin film/0D CdS QDs hybrid nanostructures. The fabrication process, morphology characterization, composition analysis, and optical properties of the hybrid nanostructure are presented. The impact of the introduced TiO_2 thin film on the photocurrent and onset potential is measured and discussed.

Chapter 5 is focused on the amorphous TiO_2 coated hierarchical WO_3 NSs/CdS NRs. The materials characterization of this hierarchical structure was presented. Then, the PEC performance was investigated through the tuning of the morphology of the CdS NRs. Finally, the photostability of this hierarchical structure is investigated and improved.

Chapter 6 is focused on FTO IOs/SnO_2 NCs/TiO_2 thin film hierarchical nanostructure. The hydrothermal growth conditions of SnO_2 NCs on the morphology of hierarchical nanostructure were investigated. Then, TiO_2 thin film was coated on this hierarchical nanostructure and their corresponding PEC performance was measured and discussed.

Chapter 7 is focused on periodic FTO IOs grafted with CdS NRs/CdSe clusters. The fabrication process and some detailed characterizations were presented in the first part. Then the optical properties, including transmission spectra, diffuse reflectance spectra, and absorption spectra are investigated. Finally, the photocurrent, and photostability are tested and discussed.

Chapter 8 is a summary of the different hierarchical nanostructures presented in this thesis. The interaction between different targeted strategies is concluded. This chapter also suggests the research direction for future research.

1.7 Findings and Outcomes

The outcomes of this thesis are listed below:

I. Fabrication of a series of novel hierarchical nanostructures with different dimensional nanostructures, including 2D/0D SnO_2 NSs/TiO_2/CdS QDs, 2D/1D WO_3 NSs/CdS NRs/TiO_2, 3D/0D FTO IOs/SnO_2 NCs/TiO_2, and 3D/1D FTO IOs/CdS NRs/CdSe clusters.

II. Different targeted strategies, such as conductive skeleton, enhancement of light scattering ability, increasing surface area, were incorporated in these hierarchical nanostructures.

III. The co-existence of photoactive long CdS NRs and short CdS NRs on WO_3 NSs are better than long CdS NRs on the surface of WO_3 NSs. Although longer CdS NRs provides higher specific surface area, the aggregation of long CdS NRs blocked the light penetration, while the co-existence of long CdS NRs and short CdS NRs formed the unoccupied space for light penetration.

IV. Although longer SnO_2 NCs provide higher specific surface area, short SnO_2 NCs grafted on the FTO IOs as a scaffold showed a better electron collection ability than long SnO_2 NCs, resulting in a higher photocurrent.

References

[1] J. Joy, J. Mathew, and S.C. George, *Int. J. Hydrogen Energy* **2018**, *43*, 4804-4817.

[2] C. Jiang, S.J.A. Moniz, A. Wang, T. Zhang, J. Tang, *Chem. Soc. Rev*. **2017**, *46*, 4645-4660.

[3] H.L. Wu, X.B. Li, C.H. Tung, L.Z. Wu, *Adv. Sci.* **2018**. *5*, 1700684.

[4] W. Yang, J. Moon, *ChemSusChem* **2018**, *12*, 1889-1899.

[5] D. Bae, B. Seger, P.C. Vesborg, O. Hansen, I. Chorkendorff, *Chem. Soc. Rev*. **2017**, *46*, 1933-1954.

[6] A. Fujishima, K. Honda, *Nature* **1972**, *238*, 37.

[7] Y. Hou, F. Zuo, A. Dagg, P. Feng, *Nano Lett*. **2012**, *12*, 6464-6473.

[8] B. Weng, C.R. Grice, J. Ge, T. Poudel, X. Deng, Y. Yan, *Adv. Energy Mater*. **2017**, *8*, 1701655.

[9] C. Li, Z. Luo, T. Wang, J. Gong, *Adv. Mater*. **2018**, *30*, 1707502.

[10] J. Sun, D.K. Zhong, D.R. Gamelin, *Energy Environ. Sci*. **2010**, *3*, 1252-1261.

[11] S. Kment, F. Riboni, S. Pausova, L. Wang, L. Wang, H. Han, Z. Hubicka, J. Krysa, P. Schmuki, R. Zboril, *Chem. Soc. Rev*. **2017**, *46*, 3716-3769.

[12] S. Choudhary, S. Upadhyay, P. Kumar, N. Singh, V.R. Satsangi, R. Shrivastav, S. Dass, *Int. J. Hydrogen Energy* **2012**, *37*, 18713-18730.

[13] A.G. Tamirat, J. Rick, A.A. Dubale, W.-N. Su, B.-J. Hwang, *Nanoscale Horiz*. **2016**, *1*, 243-267.

[14] L. Zhou, Y. Yang, J. Zhang, P.M. Rao, *ACS Appl. Mater. Interfaces* **2017**, *9*, 11356-11362.

[15] L. Zhou, C. Zhao, B. Giri, P. Allen, X. Xu, H. Joshi, Y. Fan, L.V. Titova, P.M. Rao, *Nano Lett*. **2016**, *16*, 3463-3474.

[16] M.A. Mansoor, M.A. Ehsan, V. McKee, N.-M. Huang, M. Ebadi, Z. Arifin, W.J. Basirun, M. Mazhar, *J. Mater. Chem. A* **2013**, *1*, 5284-5292.

[17] D. Yokoyama, H. Hashiguchi, K. Maeda, T. Minegishi, T. Takata, R. Abe, J. Kubota, K. Domen, *Thin Solid Films* **2011**, 519, 2087-2092.

[18] Y. Zhou, L. Zhang, L. Lin, B.R. Wygant, Y. Liu, Y. Zhu, Y. Zheng, C.B. Mullins, Y. Zhao, X. Zhang, G. Yu, *Nano Lett*. **2017**, *17*, 8012-8017.

[19] I.S. Cho, H.S. Han, M. Logar, J. Park, X. Zheng, *Adv. Energy Mater*. **2016**, *6*, 1501840.

[20] F. Ning, M. Shao, S. Xu, Y. Fu, R. Zhang, M. Wei, D.G. Evans, X. Duan, *Energy Environ. Sci*. **2016**, *9*, 2633-2643.

[21] K. Sivula, F.L. Formal, M. Gratzel, *Chem. Mater*. **2009**, *21*, 2862-2867.

[22] J.Y. Kim, G. Magesh, D.H. Youn, J.-W. Jang, J. Kubota, K. Domen, J.S. Lee, *Sci. Rep*. **2013**, *3*, 2681.

[23] G. Segev, C.-M. Jiang, J.K. Cooper, J. Eichhorn, F.M. Toma, I.D. Sharp, *Energy Environ. Sci*. **2018**, *11*, 904-913.

[24] H.-Y. Wang, H. Yang, L. Zhang, J. Chen, B. Liu, *ChemNanoMat* **2016**, *2*, 660-664.

[25] Z. Zhang, L., T. Yu, Y. Hu, W. Luo, W. Zhu, G. Fu, Z. Li, H. Gao, F. Li, Z. Zou, *ACS Appl. Mater. Interfaces* **2015**, *7*, 26482-26490.

[26] G. Ai, H. Li, S. Liu, R. Mo, J. Zhong, *Adv. Funct. Mater*. **2015**, *25*, 5706-5713.

[27] R. Boppella, S.T. Kochuveedu, H. Kim, M.J. Jeong, F. Marques Mota, J.H. Park, D.H. Kim, *ACS Appl. Mater. Interfaces* **2017**, *9*, 7075-7083.

[28] R. Wang, L. Wang, Y. Zhou, Z. Zou, *Appl. Catal. B-Environ*. **2019**, *255*, 117738.

[29] L. Cai, J. Zhao, H. Li, J. Park, I.S. Cho, H.S. Han, X. Zheng, *ACS Energy Lett*. **2016**, *1*, 624-632.

[30] S.K. Karuturi, C. Cheng, L. Liu, L. Tat Su, H.J. Fan, A.I.Y. Tok, *Nano Energy* **2012**, *1*, 322-327.

[31] H. Chen, S. Yang, *Nanoscale Horiz*. **2016**, *1*, 96-108.

[32] Z. Li, S. Feng, S. Liu, X. Li, L. Wang, W. Lu, *Nanoscale* **2015**, *7*, 19178-19183.

[33] Y. Liu, Z. Kang, H. Si, P. Li, S. Cao, S. Liu, Y. Li, S. Zhang, Z. Zhang, Q. Liao, *Nano Energy* **2017**, *35*, 189-198.

Chapter 2

Literature Review

This chapter describes some basic concepts, such as space charge layer, flat-band position and photovoltage in the PEC water splitting process. Typical parameters than can indicate the PEC performance are also introduced here. Then, the properties of some typical photoanode materials are presented. Finally, the literature about various nanostructured semiconductors with the incorporation of different targeted strategies is summarized and discussed.

2.1 Basic Concepts in PEC Process

2.1.1 Band Bending

The energy levels and electron properties are described by the energy band theory, which is shown in Figure 2.1(a). The valence band (VB) is filled with electrons and its upper edge is E_{VB}, while the conduction band (CB) is empty and its lowest edge is E_{CB}. E_g is the bandgap. E_F is the Fermi level, which locates in a few kT from the CB level for the n-type semiconductor and indicates the electrons` electrochemical potential. In a redox electrolyte, Nernst expression can be used to describe the electrochemical potential of electrons based on equation (1).[1]

$$U_{redox} = U^{\ominus}_{redox} + \frac{kT}{e} ln\left(\frac{C_{ox}}{C_{red}}\right) \qquad (1)$$

Where kT is the thermal energy, C_{red} and C_{ox} are the activities of the oxidized and reduced elements. $U^{\ominus}_{redox}$ is the standard redox potential when C_{red} and C_{ox} are equal. The Fermi level E_{redox} of the electrons in the electrolyte can be calibrated to the vacuum reference by the following equation (2).

$$E_{redox} = -4.5\ eV - eU^{\ominus}_{redox} \qquad (2)$$

As shown in Figure 2.1(b), before contact, the E_F of an n-type semiconductor is usually higher as compared to the E_{redox} of an electrolyte.[2] When semiconductors are immersed in the electrolyte, the thermal equilibrium is established by aligning the Fermi levels. Specifically, electrons flow from the higher E_F to the E_{redox} until E_F equals to E_{redox}. During thermal equilibrium, electrons from the donor impurities are consumed while ionized donors remain, resulting in the formation of a depletion layer (space charge layer) I near the semiconductor side, as shown in Figure 2.1(c). On the solution side, a Helmholtz layer II with a thickness of around 0.3-0.5 nm and a Gouy diffuse layer III is formed.[3] The potential drop across the double layers causes an upward band bending, which is essential for the charge separation.[4]

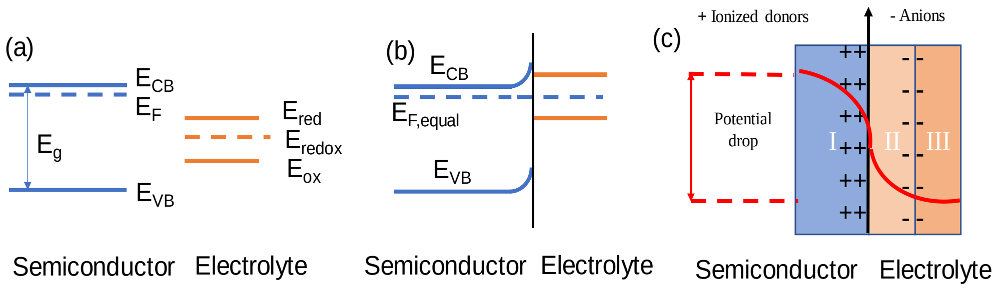

Figure 2.1 (a) Energy level of semiconductor and electrolyte before contact; (b) The energy level of electrolyte and semiconductor after contact; (c) Formation of the space charge region.

2.1.2 Flat Band Potential

As the conductivity of the semiconductor is lower than the electrolyte, the potential drop at the depletion layer is much higher than that at the electrolyte side. Hence, most of the applied external voltage would be exerted on the depletion layer and thus influence the band bending in the depletion layer.[3] Applying a negative voltage (V_A) would result in a decrease in the depletion layer and the reduction of band bending, as shown in Figure 2.2(a). When the band bending is reduced to zero, the corresponding applied potential is the flat band potential (V_{FB}), as shown in Figure 2.2(b), which can be utilized to estimate the position of the Fermi level of a semiconductor.[5] The flat-band position can also be reflected by the onset potential of the photocurrent.[6] When the applied potential is larger than V_{FB}, the depletion layer could be formed and thus drive the separation of the photogenerated carriers. However, the practical onset potential may be much more positive than the flat potential. Yongbo Kuang et.al reported that the onset potential of Ta_3N_5 was 0.6 V vs. RHE while its flat-band potential was smaller than 0.1 eV.[7] The difference between the practical onset potential and flat-band potential is caused by the slow OER kinetics, charge recombination in the depletion layer or the existence of surface defects. As V_{FB} is close to the CB edges, it can be used to evaluate the position of E_{CB}.[8] Another frequently used method to determine V_{FB} is the Mott-Schottky analysis, which will be introduced in Chapter 3.

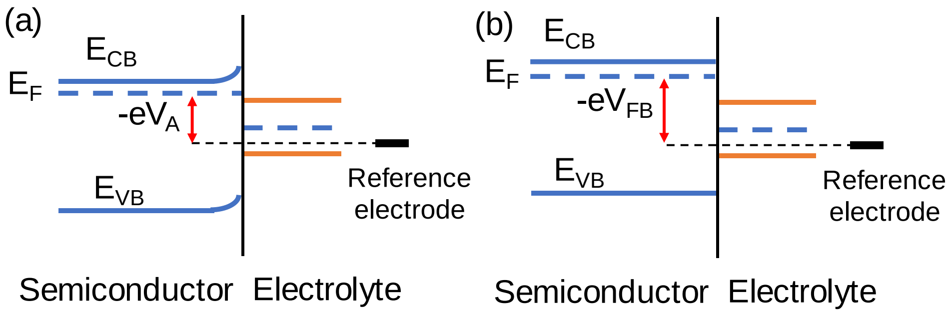

Figure 2.2 (a) The decrease in band bending by applying a negative voltage; (b) The band bending decreases to zero when the flat band potential is applied.

2.1.3 Quasi-Fermi Level and Photovoltage

As shown in Figure 2.3(a), upon the steady-state illumination, holes and electrons are generated and cause the upward shift of the Fermi level. These non-equilibrium electron and hole populations are described by the quasi-Fermi level through equation (3) and (4).[5]

$$n = n_0 + \Delta n = N_C\, e^{-(E_C - E^*_{F,n})/\mathrm{kT}} \qquad (3)$$

$$p = p_0 + \Delta p = N_V\, e^{-(E^*_{F,p} - E_V)/\mathrm{kT}} \qquad (4)$$

Where n_0 and p_0 are the concentrations of electrons and holes in the dark condition. After illumination, both the carrier concentrations increase by Δn and Δp. Since n_0 is much larger than p_0 in an n-type semiconductor, $E_{F,n}$ remains horizontal but $E_{F,p}$ shifts downward, which produces an open voltage (V_{ph}). At the same time, the band bending is reduced. The maximum V_{ph} is determined by the difference between the E_{redox} of the electrolyte and the flat-band potential of the semiconductor, so it can reflect the thermodynamic ability of a semiconductor for HER.[3] To drive a water-splitting reaction, V_{ph} must be large than 1.23 V. A high V_{ph} is essential to the PEC water splitting, and this value can be determined experimentally by measuring the open-circuit potentials under illumination and dark conditions.

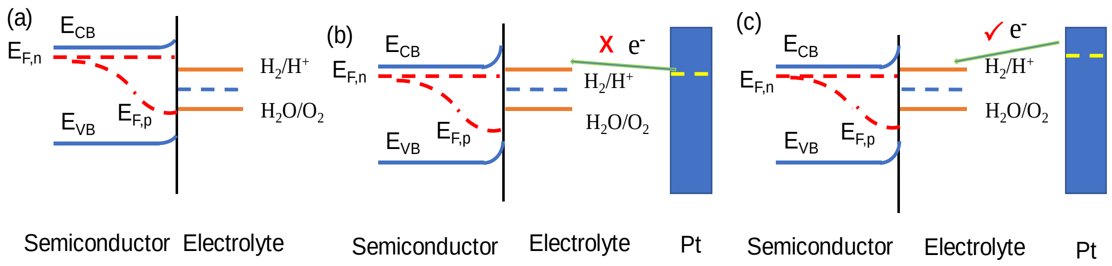

Figure 2.3 (a) Formation of photovoltage; (b) the applied potential is smaller than the onset potential; (c) the applied potential is larger than the onset potential.

Truong Thi Hien et al. investigated the impact of an applied potential on band bending and lifting of the E_F of the counter electrode.[2] When the applied potential is lower than the onset potential, the external potential is mainly distributed to form a depletion layer at the electrolyte/semiconductor interface, as shown in Figure 2.3(b). When the applied potential is larger than the onset potential, as shown in Figure 2.3(c), it would be mostly distributed to the lifting up of E_F of counter electrode until it becomes higher than the $E(H_2/H^+)$. The continuously increasing potential consumed on the electrolyte/semiconductor junction would accelerate the electrons injection and thus enhance charge separation, resulting in an exponential rise in the photocurrent.

2.1.4 Photocorrosion

When photogenerated holes accumulated the surface, the semiconductor oxidizes itself rather than the water, resulting in photocorrosion and thus decrease the photostability of the semiconductor. For the n-type semiconductor materials, the anodic oxidation is shown in equation (5).[5]

$$M_xO_y + \frac{2y}{x}h^+ \xleftrightarrow{electrolyte} xM_{aq}^{\frac{2y}{x}} + \frac{y}{2}O_2 \qquad (5)$$

The photostability of a semiconductor can be predicted by comparing its energy level for anodic decomposition potential E_d with $E(H_2O/O_2)$.[9] As shown in Figure 2.4(a), semiconductors with an E_d position more positive than $E(H_2O/O_2)$ are stable because

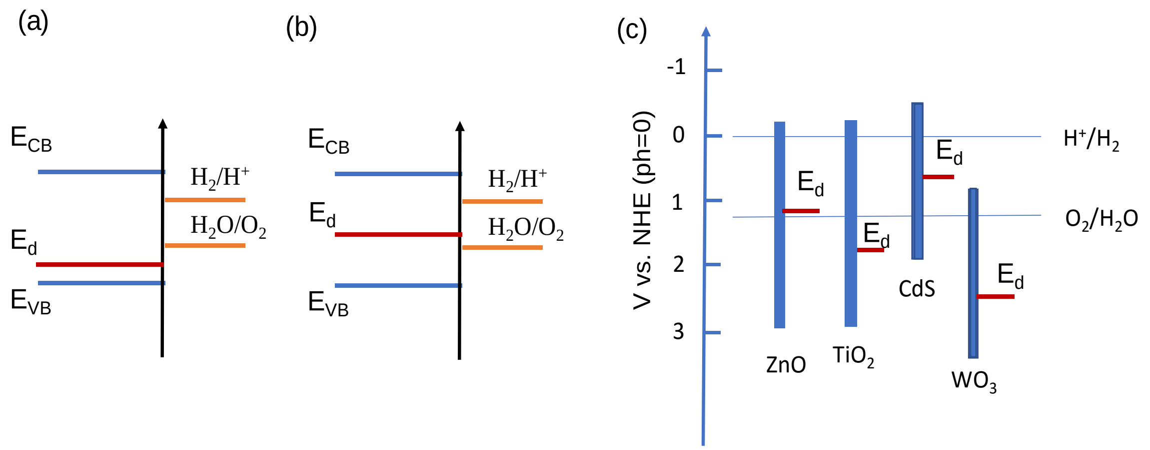

Figure 2.4 (a) A semiconductor that can resist photo-corrosion due to its low level of E_d. (b) A semiconductor that suffers from photo-corrosion due to its high level of E_d; (c) The E_d position of some typical semiconductors.

photogenerated holes would prefer to join OER. When E_d of a semiconductor is more negative than $E(H_2O/O_2)$, as shown in Figure 2.4(b), self-decomposition of the semiconductor is more easily achieved by the photogenerated holes than the oxidation of water. The anodic decomposition potential of some typical semiconductors is shown in Figure 2.4(c). It can be found that WO_3 and TiO_2 are stable while CdS and ZnO are susceptible to photo-corrosion. To alleviate the photo-corrosion, the photogenerated holes should be consumed quickly. Using scavengers as the electrolyte or loading of co-catalyst could extend the lifetime of the semiconductors under illumination for PEC applications.[10]

2.2 Photoanode Materials

2.2.1 TiO_2

Titanium dioxide (TiO_2) has been investigated for its high stability, suitable CB and VB edges and low toxicity.[11] However, the PEC performance of TiO_2 is mainly restricted by its wide optical bandgap, short hole diffusion lengths (L = 10-100 nm), and poor electron mobility (0.1-1 $cm^2\ V^{-1}\ S^{-1}$).[12] Two different phases of TiO_2 materials, including anatase and rutile phase, have been reported for PEC applications. TiO_2 nanorods (NRs) obtained through the hydrothermal growth usually have a rutile phase, while anatase TiO_2 nanostructures, existing mainly in the form of a film, can be obtained by atomic layer deposition.[13, 14] The bandgap of rutile and anatase phases of TiO_2 is 3.0 eV and 3.2 eV respectively, indicating that TiO_2 can only respond to UV light. However, UV light accounts for only 4% of total solar energy. Furthermore, poor electron collection will also lead to severe charge recombination during the migration from the photoanode to the counter electrode.[15]

2.2.2 CdS

Cadmium sulfide (CdS) has a narrow bandgap of around 2.4 eV, making it possible to harvest visible light. Moreover, the CB edge of CdS is more positive than many other semiconductors, which is favorable for heterojunction formation.[16] However, CdS suffers from serious photocorrosion during the PEC process as reflected in Figure 2.4(c). Besides, Cd^{2+} is highly toxic, which hinders its extensive application. CdS quantum dots (QDs) can be fabricated with a successive ionic layer adsorption and reaction method, while CdS NRs can be fabricated by a hydrothermal reaction.

2.2.3 CdSe

The bandgap of cadmium selenide (CdSe) is 1.7 eV, so its absorption edge can be expanded to around 720 nm.[17] As the minimum bandgap of a single semiconductor is around 1.8-2 eV, CdSe nanomaterials were extensively used as visible sensitizers with other wide bandgap semiconductors. Chemical bath deposition was frequently used to prepare CdSe nanostructures, such as CdSe clusters and CdSe films.

2.2.4 WO_3

Tungsten oxide (WO_3) has high chemical stability in acid solution and it can be resistive to photocorrosion due to its more positive anodic decomposition potential compared to $E(H_2O/O_2)$. WO_3 has a good electron collection ability and a moderate minority

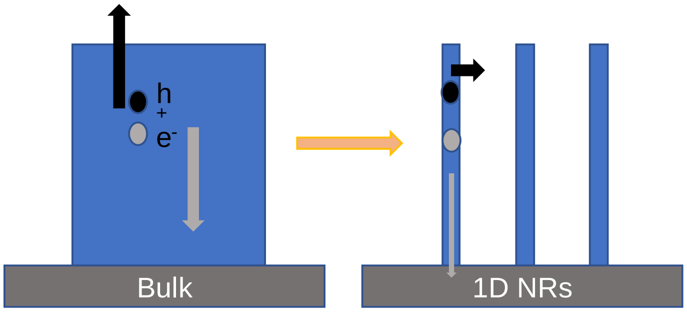

Figure 2.5 The reduced hole diffusion length in the 1D NRs.

diffusion length of 150 nm.[18] Besides, the bandgap of WO_3 is around 2.7 eV, which is capable of visible light absorption.[19] However, the CB edge of WO_3 is more positive than $E(H^+/H_2)$, so it cannot support spontaneous HER and additional overpotential is needed during the PEC process.[20] The sluggish charge transfer and surface defect induced charge recombination also limit the PEC applications of WO_3. The WO_3 thin films can be obtained by electrical deposition or sol-gel method,[21] while other nanostructures, such as WO_3 nanowires (NWs)[22] and WO_3 nanoneedles,[23] can be obtained by hydrothermal reaction.

2.2.5 Transparent Conductive Materials

Many semiconductor materials, such as Fe_2O_3[24] and $BiVO_4$,[25] suffer from low electron mobility, which induces low charge transport efficiency and serious charge recombination. Using transparent conducting oxides (TCOs) as the host scaffold is a good choice as they enable better collection of electrons generated in the guest materials and has high transparency in the visible region.[26] To date, some TCOs, such as antimony-doped tin oxide (ATO),[27] fluorine-doped tin oxide (FTO),[18] Nb-doped SnO_2 (NTO),[28] tin-doped indium oxide (ITO),[29] and aluminum-doped zinc oxide (AZO),[30] have been reported for the fabrication of host/guest photoanodes. Except for AZO, other TCOs have chemical stability in both acid and alkaline solutions, which further expands their application range.

2.3 Nanostructured Semiconductors

Compared to bulk materials, nanostructured materials have many superior properties, such as a tunable bandgap, enlarged specific surface area, and reduced hole diffusion length, as shown in Figure 2.5.[31] Herein, some reported nanostructured photoanodes are summarized by their different dimensions and properties.

2.3.1 1D Nanostructure and 1D Based Hybrid Nanostructures

2.3.1.1 Pristine 1D NRs

1D nanostructures include nanofibers, NRs or NWs, and nanotubes. Among these nanostructures, NRs or NWs could be grown on the FTO glass via a one-step hydrothermal reaction. The reaction parameters, such as the precursor concentrations and reaction durations, have been investigated. Yun Jeong Hwang et al. reported that the length of TiO_2 NWs increased linearly with prolonged hydrothermal growth duration.[32] However, the photocurrent showed a non-linear relationship with the increased length. The photocurrent increased sharply from 0.125 mA cm^{-2} to 0.61 mA cm^{-2} when the length increased from 0.28 μm to 0.9 μm, while the photocurrent only increased by 0.12 mA cm^{-2} when the length was further prolonged to 1.8 μm. This non-linear change was induced by the competition between the change of light absorption efficiency and charge collection efficiency associated with the longer nanowires.

2.3.1.2 Bandgap Engineering

Pristine 1D nanostructures alone cannot alleviate some intrinsic drawbacks of semiconductor materials, such as wide bandgap, low electron collection ability and low light scattering ability. The bandgap and the position of band edges of a semiconductor can be tuned by doping with other elements, as shown in Figure 2.6. Son Hoang reported that nitrogen-modified TiO_2 NWs could be achieved by post-annealing in NH_3 flow.[33] The substitutional N formed N 2p states, which hybridized with O 2p and made the VB edge shift upward. Thus, the N-modified TiO_2 NWs showed an extended absorption range compared to pristine TiO_2 NWs. However, the upshift of VB edge also decreased the oxidation ability of holes, thus lowering the charge transfer efficiency. This effect can be

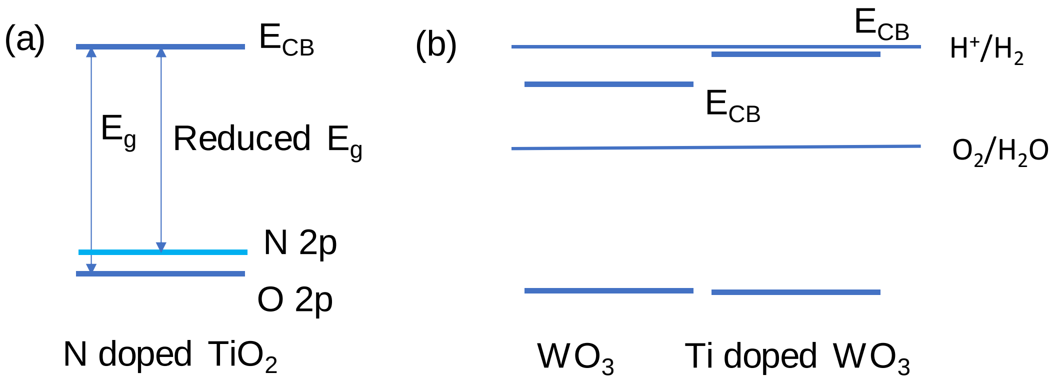

Figure 2.6 Bandgap engineering. (a) Reduce the bandgap; (b) The upward shift of E_{CB}.

alleviated by coating with co-catalysts. Doping can also change the CB edge position. Shankara S. Kalanur reported that in Ti-doped WO_3 NRs, the upwards shift of CB edge makes it close to the $E(H^+/H_2)$, which is responsible for the 3.5 times higher photocurrent produced by the Ti-doped WO_3 NRs than that of pristine WO_3 NRs.[23]

2.3.1.3 1D NRs/Cocatalyst

Many semiconductors have a large kinetic barrier for OER on the surface, resulting in the accumulation of photogenerated holes. The accumulated holes can induce serious charge recombination and thus the lower photocurrent.[34] Besides, the accumulated photogenerated holes may lead to the photocorrosion of some semiconductors, such as CdS. To avoid the accumulation of the photogenerated holes, known as charge transfer process, sacrificial reagents or hole scavengers, such as Na_2SO_3 solution, can be used to consume photogenerated holes due to the quick reaction between them.[35] However, the consumption of hole scavengers is irreversible. Another method to accelerate the charge transfer process is the loading of some appropriate electrocatalytic catalysts on the 1D nanostructures to enhance OER kinetics. Fanyu Ning et al. reported that NiFe-layered double hydroxide (LDH) could be introduced on the 1D TiO_2 NRs with reduced graphite oxide (rGO) as a connector.[36] In this hybrid nanostructure, TiO_2 NRs played the role of a light absorption, rGO enabled quick charge transport process and LDH acted as a cocatalyst to accelerate the charge transfer process. As a result, the photocurrent of 1D TiO_2 NRs/rGO/LDH was determined to be larger than 1D TiO_2 NRs/rGO and 1D TiO_2 NRs.

2.3.1.4 1D NRs/Protection layer

Among these 1D semiconductor nanostructures, CdS is one of the materials that suffered from serious photo-corrosion problems. As mentioned in the previous discussion, the photo-corrosion is caused by the positive decomposition potential compared to the O_2/H_2O potential and the accumulation of photogenerated holes on the surface. One method is using a co-catalyst or sacrificial reagent to quickly consume photogenerated holes. Guanjie Ai et al. reported that the coating of Co-Pi nanoparticles on the surface of TiO_2 NRs/CdS QDs could reduce hole transfer barriers and accelerate surface oxidation, resulting in a decreased rate of self-decomposition of CdS.[37] Although the use of co-catalyst and sacrificial reagent can relieve the photocorrosion, CdS remain stable in the long run when exposed to illumination. Thus, the introduction of a protection layer was important. Wang Ruyi et al. reported the coating of an amorphous TiO_2 thin layer on the surface of Al-doped ZnO/CdS core/shell NRs by ALD.[38] The thickness is controlled by varying the number of ALD cycles. The photocurrent of Al-doped ZnO/CdS core/shell NRs decreased to 52.6% after an illumination duration of 1800s, which was denoted as the reference lifetime. The lifetimes of Al-doped ZnO/CdS core/shell NRs coated with 30 ALD cycles, 60 ALD cycles and 150 ALD cycles of TiO_2 were 2700 s, 6500 s and more than 8000 s, respectively. The introduced TiO_2 amorphous layer can achieve the isolation of the photoanode from the surrounding electrolyte, the lowering of surface states, and storing of the photogenerated holes, resulting in an enhanced photostability. It should be mentioned that the continuous increase in the thickness of the TiO_2 amorphous layer would eventually block holes transfer and reduce light absorption, causing a decrease of the photocurrent. Thus, a balance between photostability and photocurrent should be taken into consideration.

2.3.1.5 1D Core/Shell NRs

In the core/shell nanostructures, the exterior material has a lower bandgap, which can

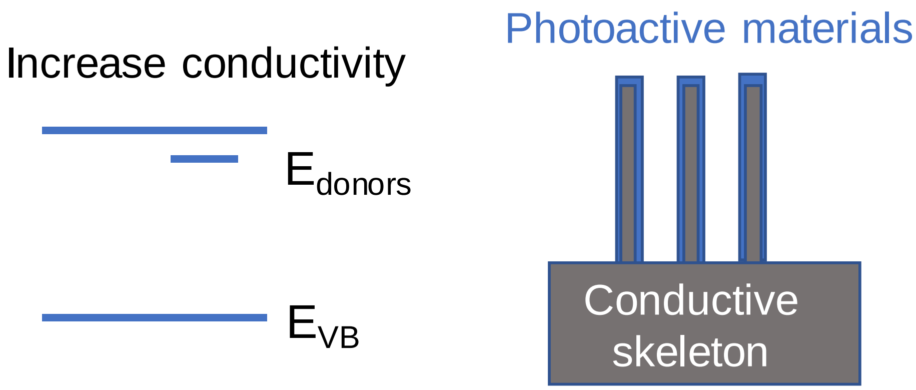

Figure 2.7 Improve charge transport by doping of coating on a conductive skeleton.

absorb more visible light. The CB and VB edges of a core material and a shell material should be well matched to accelerate charge separation. Haijin Li et al. reported that WO_3/CdS core/shell NWs could be fabricated by coating of a thin CdS shell on the surface of WO_3 NWs, which can increase visible light absorption and enhance charge separation due to the heterojunction formation between CdS and WO_3.[39] WO_3 NWs as the core provided a direct path for the transport of photogenerated electrons. A similar design can also be found in the CdS/CdSe core/shell NRs,[23] WO_3/$BiVO_4$ core/shell NRs.[25]

2.3.1.6 Improve Charge Transport

The charge collection ability of 1D nanostructures can be improved by two methods, through increasing the conductivity of the materials or coating of semiconductors on a 1D TOCs scaffold, as shown in Figure 2.7. The conductivity of a semiconductor can be improved by doping with other elements or introducing oxygen vacancy sites. Hsin-Yi Wang reported that 0.25% of Nb-doped TiO_2 NRs showed a 65% higher photocurrent than pristine TiO_2 NRs due to improved charge transport.[40] Gongming Wang et al. reported that hydrogen-treated TiO_2 NWs have newly-formed electron donor states near the CB edge due to the oxygen vacancy sites, resulting in an enhanced donor density by 3 orders of magnitudes. Thus, due to the enhanced charge transfer and separation, hydrogen treated TiO_2 NWs showed a higher photocurrent than pristine TiO_2 NWs and a lower photocurrent saturation potentials.[41]

Besides, the use of 1D TOCs NRs as a conductive skeleton can also enhance the collection of electrons generated in the guest semiconductors due to the quick electron transport path provided by them. Lite Zhou et al. reported that at potentials of 1.23 V vs. RHE, ATO NRs/$BiVO_4$ demonstrated a charge separation efficiency that is 4 times higher than that of planar $BiVO_4$ films and 1.2 times higher than that of SnO_2 NRs/$BiVO_4$.[27]

2.3.1.7 1D Branched NRs

1D branched NRs are fabricated by a two-step growth method. The obtained 1D NRs act as a template where the secondary short NRs can be grown. An additional seed layer might be necessary for the formation of branched NRs. In Sun Cho et al. reported that the photocurrent of branched TiO_2 NRs was more significant than that of pristine TiO_2 NRs. Compared to the pristine TiO_2 NRs, the surface area of branched TiO_2 NRs increased by 4 times. Furthermore, charge separation within the secondary grown short TiO_2NRs was faster than the long TiO_2 NRs.[42] Jae-Hyeok Kim et al. reported that additional heterojunctions could be formed by the coating of $BiVO_4$ films on branched WO_3 NRs.[43]

2.3.2 2D Nanostructure and 2D Based Hybrid Nanostructures

2D nanostructures mainly consist of nanosheets (NSs) and nanobowls (NBs). The NSs can be directly grown on the FTO substrate by a hydrothermal reaction or chemical vapor deposition process, while the growth of NBs usually requries a sacrificial template. Pristine 2D NSs have been reported for PEC water splitting applications due to their large active surface areas as well as efficient transport paths with low densities of grain boundaries.[44]

2.3.2.1 Heterojunctions

Similar to the 1D nanostructures, pristine 2D nanostructures suffer from some intrinsic disadvantages in PEC applications, which can be alleviated through some common enhancement strategies. The modifications of 2D nanostructures are schematically shown in Figure 2.8. Canjun Liu et al. reported that the enhanced visible light absorption and

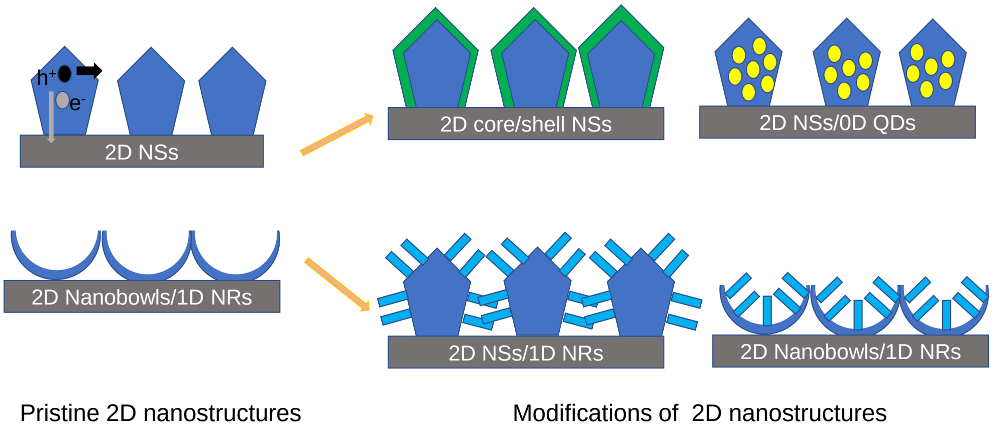

Figure 2.8 Schematic of 2D nanostructures and the modifications of 2D nanostructures.

charge separation can be accomplished through the construction of 2D heterojunctions WO_3 NSs/CdS QDs.[15] Besides, the bandgap tuning can be combined with heterojunction in one hybrid nanostructure. Kaiping Yuan et al. reported that WO_{3-x}/TiO_{2-x} core/shell NSs with oxygen-deficiency showed 8 times higher photocurrent (3.2 mA cm^{-2}) than pristine WO_3 NSs (0.41 mA cm^{-2}) at 1.23 V vs. RHE.[19] The oxygen vacancies introduced by the hydrogen thermal treatment act as shallow electron donors, resulting in enhanced charge transport. Furthermore, the extended visible light absorption was caused by the narrow bandgap due to the self-doping of Ti^{3+} and W^{5+}.

2.3.2.2 2D Nanostructures/1D NRs

Hierarchical 2D/1D structures were fabricated by the grafting of 1D NRs on the surface of 2D NSs or 2D NBs. Compared to branched 1D NRs, hierarchical 2D/1D structures are reported to have better light utilization efficiency and higher light scattering ability. Yichong Liu et al. investigated the light absorption of 2D/1D structures and branched 1D NRs by Finite-difference time-domain (FDTD) simulation.[16] The light absorption was represented by the electric-field intensity. 2D/1D structures showed an efficient and evenly distributed light absorption across the NRs from the upper zone to the bottom zone of the structure, while branched 1D NRs only demonstrated light absorption in the upper zone.

The increased light utilization efficiency can be explained by the enlarged space between two adjacent NSs, which was beneficial to light penetration.

The increased light scattering ability was reported in the hierarchical 2D nanobows/1D NRs nanostructures. Wenhui Wang et al. reported that 2D TiO_2 NBs/1D TiO_2 NRs can be fabricated by a combination of hydrothermal reaction and interfacial nanosphere lithography.[14] The 1D NRs grown on the patterned nanobowls acted as multiple light scattering centers, which exhibited a maximum reflectance of 51%, while pristine 1D NRs only presented a maximum reflectance of around 28% in the visible region. This enhanced light scattering ability resulted in increased light absorption by 2D TiO_2 nanobowls/1D TiO_2 NRs in the UV region as TiO_2 can only absorb UV light. Besides, the large surface area provided by the 2D/1D nanostructures increased the contact area with the electrolyte and the phase junction between anatase/rutile facilitated charger separation. Due to the contribution by these factors, 2D TiO_2 nanobowls/1D TiO_2 NRs showed a photocurrent 1.24 mA cm^{-2} at 1.23 V vs. RHE, while the pristine TiO_2 NRs only showed a photocurrent of 0.68 mA cm^{-2}.

2.3.3 3D Nanostructure and 3D Based Hybrid Nanostructures

3D porous nanostructures mainly consist of various periodic 3D inverse opals, which are shell structure replicated from face-centered-cubic opals. The typical fabrication method includes the formation of periodically arranged spheres as a template, the subsequent filling of precursors in the voids and then the removal of the template by post-annealing or chemical etching.[45] Due to the periodic structure, 3D IOs can enhance light-matter interactions due to their light trapping effect and slow-photon effect. The light-trapping effect is induced by multiple light scattering, which can prolong the optical path length, while slow-photon effect exists when the absorption edge of materials overlaps with the stopband of the IOs.[46] As IOs have a high specific surface area and periodic pores inside the structure, secondary materials can be easily coated on their surface to form a core/shell IOs or hierarchical 3D/1D nanostructures, as shown in Figure 2.9.

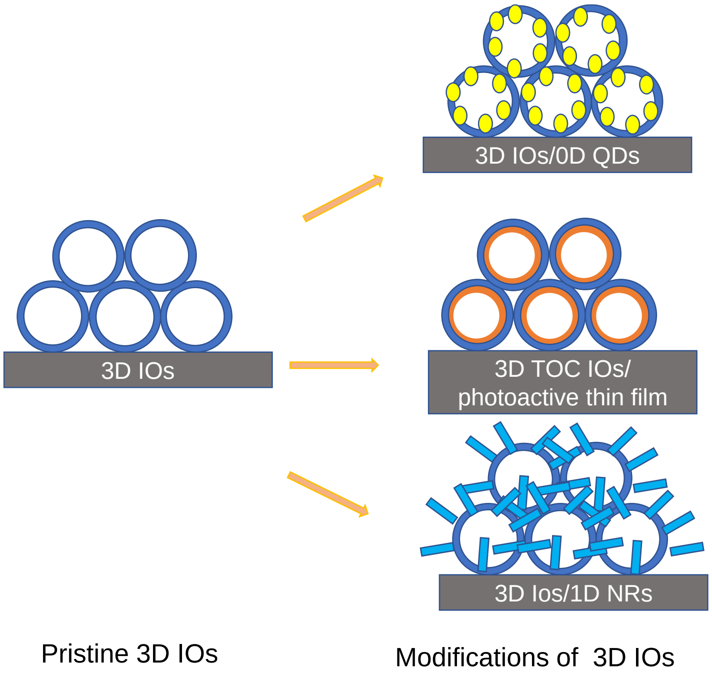

Figure 2.9 Schematic shown of 3D IOs and the modifications of 3D IOs.

2.3.3.1 Core-Shell IOs

Preparing core/shell IOs or loading of narrow bandgap semiconductors on the wide bandgap IOs is a promising strategy to improve the charge separation and light absorption simultaneously. Chuanwei Cheng et al. reported that TiO_2 IOs coated with CdS QDs could extend their absorption edge from 350 nm to 550 nm.[45] The heterojunction formation between TiO_2 and CdS could further enhance charge separation. Besides, the impact of the diameter of polystyrene (PS) microspheres on the final photocurrent was investigated. The utilization of 288 nm PS microspheres produced higher photocurrent than that of 510 nm and 900 nm, which was attributed to the enlarged surface area in smaller diameter microspheres. To achieve a fully visible-light-driven IOs, Haifeng Zhang et al. reported WO_3/$BiVO_4$ core/shell IOs as a photoanode. $BiVO_4$ shell was coated on the surface of WO_3 IOs by an electrical deposition method.[47] In the core/shell IOs, WO_3 IOs provided fast electron transport pathways to collect electrons generated in the external $BiVO_4$ films. The heterojunction formation and slow-photon effect also contributed to the charge separation and charge generation respectively. Thus, at 1.4 V vs. AgCl, $WO_3/BiVO_4$ core/shell IOs presented a higher photocurrent of 2.5 mA cm^{-2} than that of pristine WO_3 IOs (0.5 mA cm^{-2}).

2.3.3.2 TOCs Based Hybrid IOs

The fabrication of TOCs IOs has also been reported for PEC applications. Similar to the 1D TOCs nanostructures, TOCs IOs could improve the charge transport process and thus lower bulk charge recombination. Liwu Zhang et al. reported that conductive AZO IOs could quickly collect the electrons generated in the external $BiVO_4$ film.[30] The composite IOs showed a threefold higher photocurrent (1.5 mA cm^{-2} at 1.23 V vs. RHE) than pristine $BiVO_4$ IOs. Besides, the heterojunction can be combined with TOCs IOs by preparing a three-layer composite IOs. Haifeng Zhang et al. reported that TiO_2 and $BiVO_4$ films could be subsequentially coated on chemically stable FTO IOs to form composite IOs.[55] At 1.23 V vs. RHE, this composite photoanode showed a photocurrent of 4.11 mA cm^{-2} due to $TiO_2/BiVO_4$ heterojunctions and fast electron pathways provided by FTO IOs.

2.3.3.3 3D IOs/1D NRs

3D IOs/1D NRs were fabricated by the secondary growth of 1D NRs on 3D IOs, which can simultaneously achieve higher contact area with the electrolyte, more loading of visible sensitizer and enhanced light scattering ability compared to the pristine 3D IOs. Siva Krishna Karuturi et al. reported that ZnO NWs grown on the surface of TiO_2 IOs can form a hierarchical 3D nanostructure for the loading of CdS QDs.[49] To achieve the growth of ZnO NWs across the TiO_2 IOs, a ZnO seed layer was first coated on their surface by ALD due to its high infiltration ability. The length of ZnO NWs could be adjusted by tuning the reaction duration while the thickness of the hierarchical nanostructures could be controlled by the opal pore size. The high disorder resulted from the secondary growth of ZnO NWs in the hierarchical nanostructures induced the broadband diffuse scattering, contributing to the improved light scattering ability. Because of the unique structure of 3D IOs/1D NRs, TiO_2 IOs/ZnO NWs/CdS QDs showed a more significant photocurrent density of 6.2 mA cm^{-2} at 0 V vs. Ag/AgCl than TiO_2 IOs/CdS QDs (3.6 mA cm^{-2}) and ZnO NWs/CdS QDs (2.9 mA cm^{-2}).

References

[1] K. Rajeshwar, *Encyclopedia of electrochemistry*, **2007**, *6*, 1-53.
[2] T.T. Hien, N.D. Quang, C. Kim, D. Kim, *Nano Energy* **2019**, *57*, 660-669.
[3] C. Ding, J. Shi, Z. Wang, C. Li, *ACS Catal*. **2016**, *7*, 675-688.
[4] S. Kment, F. Riboni, S. Pausova, L. Wang, L. Wang, H. Han, Z. Hubicka, J. Krysa, P. Schmuki, R. Zboril, *Chem. Soc. Rev*. **2017**, *46*, 3716-3769.
[5] R. Van de Krol, *Springer* **2012**, 13-67.
[6] S.J. Hong, S. Lee, J.S. Jang, J.S. Lee, *Energy Environ. Sci*. **2011**, 4, 1781-1787.
[7] Y. Kuang, T. Yamada, K. Domen, *Joule* **2017**, 1, 290-305.
[8] M. Macias-Montero, S. Askari, S. Mitra, C. Rocks, C. Ni, V. Svrcek, P.A. Connor, P. Maguire, J.T.S. Irvine, D. Mariotti, *Nanoscale* **2016**, *8*, 6623-6628.
[9] L.-J. Guo, J.-W. Luo, T. He, S.-H. Wei, S.-S. Li, *Phys. Rev. Appl*. **2018**, *10*, 064059.
[10] W. Wu, G. Liu, Q. Xie, S. Liang, H. Zheng, R. Yuan, W. Su, L. Wu, *Green Chem*. **2012**, *14*, 1705-1709.
[11] C. Gao, T. Wei, Y. Zhang, X. Song, Y. Huan, H. Liu, M. Zhao, J. Yu, X. Chen, *Adv. Mater*. **2019**, *31*, 1806596.
[12] C. Li, H. Zhang, C. Cheng, *RSC Adv*. **2016**, *6*, 37407-37411.
[13] M.P. Suryawanshi, U.V. Ghorpade, S.W. Shin, M.G. Gang, X. Wang, H. Park, S.H. Kang, J.H. Kim, *ACS Catal*. **2017**, *7*, 8077-8089.
[14] W. Wang, J. Dong, X. Ye, Y. Li, Y. Ma, L. Qi, *Small* **2016**, *12*, 1469-1478.
[15] Q. Peng, B. Kalanyan, P.G. Hoertz, A. Miller, D.H. Kim, K. Hanson, L. Alibabaei, J. Liu, T.J. Meyer, G.N. Parsons, *Nano Lett*. **2013**, *13*, 1481-1488.
[16] Y. Liu, Y. Cui, F. Huang, X. Yang, *RSC Adv*. **2016**, *6*, 16668-16672.
[17] M. Wang, J. Jiang, J. Shi, L. Guo, *ACS Appl. Mater. Interfaces* **2013**, *5*, 4021-4025.
[18] Y. Wang, W. Tian, L. Chen, F. Cao, J. Guo, L. Li, *ACS Appl. Mater. Interfaces* **2017**, *9*, 40235-40243.
[19] K. Yuan, Q. Cao, H.-L. Lu, M. Zhong, X. Zheng, H.-Y. Chen, T. Wang, J.-J. Delaunay,

W. Luo, L. Zhang, Y.-Y. Wang, Y. Deng, S.-J. Ding, D.W. Zhang, *J. Mater. Chem. A* **2017**, *5*, 14697-14706.

[20] S.S. Kalanur, I.-H. Yoo, H. Seo, *Electrochim. Acta* **2017**, *254*, 348-357.

[21] W.L. Kwong, N. Savvides, C.C. Sorrell, *Electrochim. Acta* **2012**, *75*, 371-380.

[22] J. Su, X. Feng, J.D. Sloppy, L. Guo, C.A. Grimes, *Nano Lett*. **2011**, *11*, 203-208.

[23] T. Jin, P. Diao, Q. Wu, D. Xu, D. Hu, Y. Xie, M. Zhang, *Appl. Catal. B-Environ*. **2014**, *148*, 304-310.

[24] M. Ji, J. Cai, Y. Ma, L. Qi, ACS *Appl. Mater. Interfaces* **2016**, *8*, 3651-3660.

[25] B. Zhang, L. Wang, Y. Zhang, Y. Ding, Y. Bi, *Angew. Chem. Int. Ed*. **2018**, *57*, 2248-2252.

[26] I. Kondofersky, H.K. Dunn, A. Muller, B. Mandlmeier, J.M. Feckl, D. Fattakhova-Rohlfing, C. Scheu, L.M. Peter, T. Bein, *ACS Appl. Mater. Interfaces* **2015**, *7*, 4623-4630.

[27] L. Zhou, C. Zhao, B. Giri, P. Allen, X. Xu, H. Joshi, Y. Fan, L.V. Titova, P.M. Rao, *Nano Lett*. **2016**, *16*, 3463-3474.

[28] M. Stefik, M. Cornuz, N. Mathews, T. Hisatomi, S. Mhaisalkar, M. Gratzel, *Nano Lett*. **2012**, *12*, 5431-5435.

[29] Z. Zhang, C. Gao, Y. Li, W. Han, W. Fu, Y. He, E. Xie, *Nano Energy* **2016**, *30*, 892-899.

[30] L. Zhang, E. Reisner, J.J. Baumberg, *Energy Environ. Sci.* **2014**, *7*, 1402-1408.

[31] J. Joy, J. Mathew, S.C. George, *Int. J. Hydrogen Energy* **2018**, *43*, 4804-4817.

[32] Y.J. Hwang, C. Hahn, B. Liu, P. Yang, *ACS Nano* **2012**, *6*, 5060-5069.

[33] S. Hoang, S. Guo, N.T. Hahn, A.J. Bard, C.B. Mullins, Nano Lett. **2011**, *12*, 26-32.

[34] X.T. Xu, L. Pan, X. Zhang, L. Wang, J.J. Zou, *Adv. Sci*. **2019**, *6*, 1801505.

[35] Z. Haider, Y.S. Kang, ACS *Appl. Mater. Interfaces* **2014**, *6*, 10342-10352.

[36] F. Ning, M. Shao, S. Xu, Y. Fu, R. Zhang, M. Wei, D.G. Evans, X. Duan, *Energy Environ. Sci*. **2016**, *9*, 2633-2643.

[37] G. Ai, H. Li, S. Liu, R. Mo, J. Zhong, *Adv. Funct. Mater*. **2015**, *25*, 5706-5713.

[38] R. Wang, L. Wang, Y. Zhou, Z. Zou, *Appl. Catal. B-Environ*. **2019**, *255*, 117738.

[39] H. Li, Y. Zhou, L. Chen, W. Luo, Q. Xu, X. Wang, M. Xiao, Z. Zou, *Nanoscale* **2013**, *5*, 11933-11939.

[40] H.-Y. Wang, H. Yang, L. Zhang, J. Chen, B. Liu, *ChemNanoMat* **2016**, *2*, 660-664.

[41] G. Wang, H. Wang, Y. Ling, Y. Tang, X. Yang, R.C. Fitzmorris, C. Wang, J.Z. Zhang, Y. Li, *Nano Lett*. **2011**, *11*, 3026-3033.

[42] I.S. Cho, Z. Chen, A.J. Forman, D.R. Kim, P.M. Rao, T.F. Jaramillo, X. Zheng, *Nano Lett*. **2011**, *11*, 4978-4984.

[43] J.-H. Kim, D.H. Kim, J.W. Yoon, Z. Dai, J.-H. Lee, ACS *Appl. Energy Mater*. **2019**, *2*, 4535-4543.

[44] M. Zhou, X.W.D. Lou, Y. Xie, *Nano Today* **2013**, *8*, 598-618.

[45] C. Cheng, S.K. Karuturi, L. Liu, J. Liu, H. Li, L.T. Su, A.I. Tok, H.J. Fan, *Small* **2012**, *8*, 37-42.

[46] M. Curti, J. Schneider, D.W. Bahnemann, C.B. Mendive, *J. Phys. Chem. Lett*. **2015**, *6*, 3903-3910.

[47] H. Zhang, W. Zhou, Y. Yang, C. Cheng, *Small* **2017**, *13*, 1603840.

[48] H. Zhang, C. Cheng, *ACS Energy Lett*. **2017**, *2*, 813-821.

[49] S.K. Karuturi, J. Luo, C. Cheng, L. Liu, L.T. Su, A.I. Tok, H.J. Fan, *Adv. Mater*. **2012**, *8*, 244157-4162.

Chapter 3

Experimental Methodology

This chapter describes the principle of some typical fabrication methods, including atomic layer deposition, self-assembly, hydrothermal reaction, forced dip-coating and chemical bath deposition. Following that, the application of these methods in the preparation of various nanostructures is also described. The mechanism of conventional PEC measurement methods is also presented in this chapter. Finally, the principles and applications of typical material characterization methods, such as SEM, TEM, XRD and XPS, are elaborated.

3.1 Fabrication methods

3.1.1 Self-assembly

Solvent evaporation-induced self-assembly method has been extensively used to prepare three-dimensional ordered colloidal crystals from one-dimensional nanoparticles or nanorods.[1] In this thesis, the solvent evaporation-induced self-assembly method was used to prepare polystyrene (PS) opals. As shown in Figure 3.1, PS microspheres are floating on the water surface due to the evaporation of the solvent. In the initial nucleation process, PS microspheres form smaller ordered areas due to the capillary force. With the convective flow and electrostatic repulsion, PS microspheres are aggregated around these nucleations, creating larger and multiple layers of ordered area. In the practical experiments, a glass substrate is placed inside the solvent at a small titled angle. Thus, the colloidal crystals can be transferred to the glass due to the solvent evaporation. The fabrication process of PS opals is shown in Chapter 6 and Chapter 7.

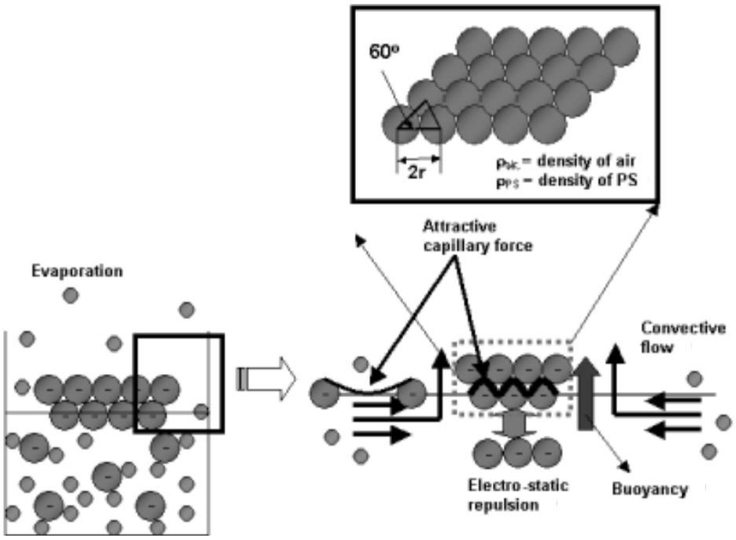

Figure 3.1 Schematic shown for the self-assembly of PS microspheres. Reprinted with permission from S.H. Im, Y.T. Lim, D.J. Suh, O.O. Park, Adv. Mater. 14 (2002) 1367-1369. Copyright (2002) John Wiley& Sons, Inc.

3.1.2 Forced Impregnation

A forced impregnation was reported to prepare inverse opals (IOs) with PS colloidal crystals as a template, as shown in Figure 3.2.[2] The PS colloidal crystals are soaked into absolute methanol solution to achieve sufficient filling of methanol into the voids inside the colloidal crystals. PS colloidal crystals are then transferred to the precursors under vacuum condition. As the boiling point of methanol is lower than that of the precursors, methanol will be evacuated under the vacuum condition and form a negative pressure inside the voids, promoting the filling of external precursors into the void areas. Finally, the template can be removed by a post-annealing treatment.

In this thesis, forced impregnation was used to prepare FTO IOs. The fabrication process is described in Chapter 6 and Chapter 7.

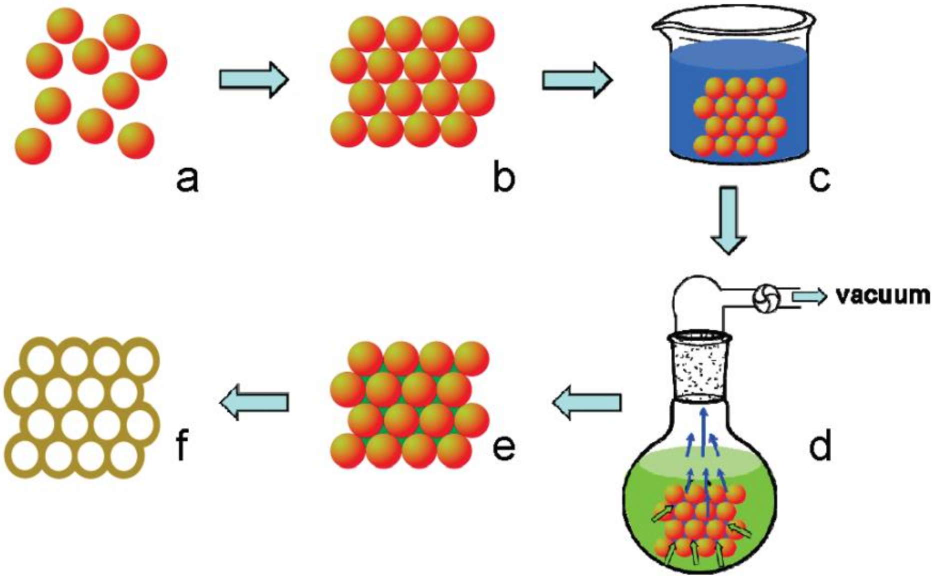

Figure 3.2 Schematic shown for the forced impregnation method for the fabrication of inverse opals. (a) PS microspheres; (b) PS colloidal crystals; (c) PS colloidal crystals soaked into the methanol solution; (d) connect with a vacuum pump; (e) infiltration of precursors; (f) inverse opals. Reprinted with permission from X. Chen, Z. Li, J. Ye, Z. Zou, Chem. Mater. 22 (2010) 3583-3585. Copyright (2010) American Chemical Society.

3.1.3 Hydrothermal Reaction

The hydrothermal reaction is one of the most common methods to prepare various nanocrystals (NCs), nanorods (NRs), and nanosheets (NSs). Typically, the precursors and a substrate are loaded into a sealed Teflon vessel and then reacted at a high temperature and pressure. The hydrothermal reaction can be described as a dissolution and crystallization process.[3] Some precursors are highly stable at low temperatures. However, they can be dissolved under high temperatures and pressures. The reaction between precursors forms the numerous nuclei, acting as growth sites for the following reaction. During this process, some capping agents may be necessary for the formation of specific nanostructures.[4]

Hydrothermal reaction was used to prepare SnO_2 NSs (Chapter 4), WO_3 NSs (Chapter 5), WO_3 NSs/CdS NRs (Chapter 5), FTO IOs/ SnO_2 NSs (Chapter 6), and FTO IOs/CdS NRs (Chapter 7).

3.1.4 Atomic Layer Deposition

Atomic layer deposition (ALD) is a common method to produce metal oxide thin film, which involves a self-limiting reaction with two different gas compounds as the reaction precursors. The metal precursor is usually highly active, which can react with surface hydroxyl groups. If the vapor pressure of the metal precursors at the room temperature is too low, additional heating will be necessary to ensure the transfer of metal precursors into the chamber. The precursor providing oxygen is usually water or ozone. A typical ALD process contains four steps, as shown in Figure 3.3.[5] Firstly, the metal precursor is introduced to the chamber and then absorbed onto the substrate through a chemisorption reaction. Due to the limited active sites on the substrate, only a small amount of metal precursors will be absorbed. In the second step, an inert gas, such as N_2 or Ar, is used to remove excessive precursors and byproducts. Thirdly, the oxygen precursor is pulsed

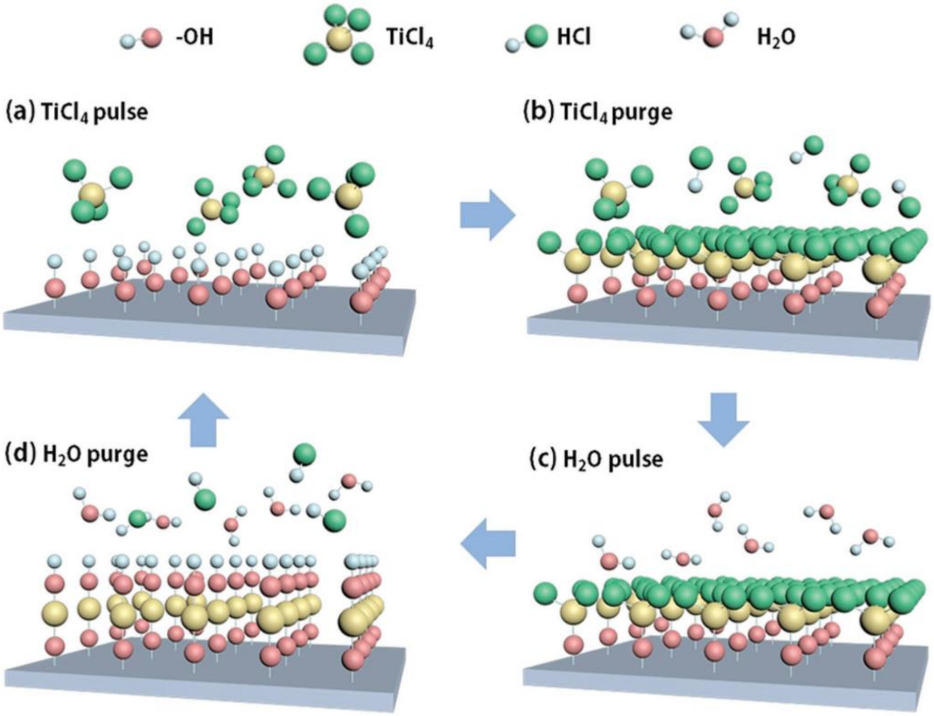

Figure 3.3 Schematic shown for the ALD process. Reprinted with permission from L. Wen, M. Zhou, C. Wang, Y. Mi, Y. Lei, Adv. Energy Mater. 6 (2016) 1600468. Copyright (2016) John Wiley& Sons, Inc.

into the chamber, which can react with the absorbed metal precursors on the substrate and thus forms a layer of metal oxide. Due to the limited metal precursors, excessive oxygen precursors will not be consumed and remain in the chamber. Finally, an inert gas is introduced to chamber again to remove excess oxygen precursors and byproducts. These four steps make up one cycle and through repeating these cycles, a metal oxide film can be obtained. Due to this self-limiting property, ALD can achieve a continuous and conformal film on various substrates.

A customized ALD in our lab has two different modes. The regular continuous flow mode is suitable for flat substrates, while a stop-flow mode ALD is suitable for porous substrates. In a continuous flow mode, the chamber is connected with a vacuum pump. The precursor will flow through the chamber and reach to the vacuum line directly. The pressure in the chamber is close to the vacuum state. In the stop-flow mode, the connection between the chamber and the vacuum pump is controlled by a valve. Once the precursor is introduced, the chamber will be disconnected from the vacuum pump. The pressure of the chamber can be increased by adding inert gas. With higher pressure, precursors are able to penetrate into the bottom of the porous structures, ensuring the uniform coating all across the porous nanostructures.

In this thesis, ALD was used to fabricate TiO_2 thin films on SnO_2 NSs (Chapter 4), WO_3 NSs/CdS NRs (Chapter 5), FTO IOs/SnO_2 NCs (Chapter 6).

3.1.5 Chemical Bath Deposition

Chemical bath deposition has been extensively used to prepare various semiconductor thin films, which involves the direct reaction between metal ions and sulfide, hydroxide, and selenide ions.[6] The morphology and the thickness can be adjusted by the reaction duration, temperature, and concentration.

Successive ionic layer adsorption and reaction (SILAR) is a variation of chemical bath deposition. The substrate is immersed in an ionic solution and an anionic solution separately. After each immersion, the substrate needs to be rinsed with water to remove unreacted chemicals. Through the control of the cycles, the thickness of the film can be tuned.[7]

3.2 PEC measurement

3.2.1 Photocurrent

Linear sweep voltammetry (LSV) is extensively used to measure the current between the photoanode and the counter electrode.[8] The current measured under light is called photocurrent because it is induced by the conversion of solar energy. The photocurrent is usually tested under AM 1.5 100 mW cm^{-2}, and it linearly increases with the irradiated surface. Thus, photocurrent density can be utilized to represent the PEC performance of a photoanode. A higher photocurrent density indicates higher solar energy conversion efficiency. The current that is measured without light illumination is called a dark current. The dark current of a photoanode is nearly zero when the applied voltage is smaller than 1.23 V, which corresponds to the minimum potential for the OER in the electrical water splitting. However, if there is contact between the conductive substrate and the electrolyte or some other oxidation process that exists, the dark current would be larger than zero, indicating the existence of charge recombination or photo-corrosion. The chopped photocurrent is measured under fixed light on and light off conditions, which can demonstrate the light response of the photoanode. Due to the accumulation of holes on the photoanode surface or surface defects induced charge recombination, the photocurrent transients could be observed.[9] Besides, the onset potential corresponds to the potential where the current equals to zero, which can be directly read from the LSV curves. The onset potential is determined by the difference between open-voltage and kinetic overpotential.

3.2.2 IPCE

The PEC performance of a photoanode can also be reflected through measuring incident photon-to-current efficiency (IPCE), which is the ratio between the number of photogenerated electrons and that of incident photons, as shown in equation (1).[10]

$$\mathrm{IPCE} = \frac{\frac{n_{\mathrm{electron}}}{\mathrm{s\,cm^2}}}{\frac{N_{\mathrm{photon}}}{\mathrm{s\,cm^2}}} = \frac{\frac{\mathrm{I(mA/cm^2)}}{\mathrm{e}}}{\frac{\mathrm{P(mW/cm^2)}}{\mathrm{hc/\lambda}}} = \frac{\mathrm{I(mA/cm^2)}}{\mathrm{P(mW/cm^2)}} \times \frac{\mathrm{hc/\lambda}}{\mathrm{e}} = \frac{\mathrm{I(mA/cm^2)}}{\mathrm{P(mW/cm^2)}} \times \frac{1240}{\lambda} \quad (1)$$

Where P is the power density of the incident light at a different wavelength, I is the photocurrent density, and λ is the wavelength of the incident light. A higher IPCE indicates more incident photons could be absorbed to generate electrons.

3.2.3 EIS

Electrochemical impedance spectroscopy (EIS) is conducted to analyze the charge transfer resistance at the semiconductor/electrolyte interface across a double charged layer, which could be determined through the diameter of the middle frequency (1-10^5 Hz) semicircle shown in the Nyquist plots.[11] It can also be determined through equivalent circuit simulation. The smaller charge resistance represents a faster collection of charge carriers and accelerated electron-hole separation.

3.3 Materials Characterization methods

Field-emission scanning electron microscope (SEM), transmission electron microscope (TEM), High-resolution TEM (HRTEM), scanning transmission electron microscope (STEM) and energy-dispersive X-ray spectroscopy (EDS), X-ray diffraction (XRD), X-ray photoelectron spectroscopy (XPS) could be used to investigate the microstructure, morphology, crystalline phase, and the elemental composition of the as-prepared samples.

3.3.1 SEM and EDS

SEM uses a highly focused electron beam as the primary electrons to investigate the morphology and elementary composition of a specimen. As shown in Figure 3.4(a), when a specimen is under electron beam irradiation, different types of signals will be excited, such as secondary electrons and characteristic X-ray photons.[12] These signals contain information about the top surface morphology and atomic number, which are collected by different detectors and then converted to images on the screen.

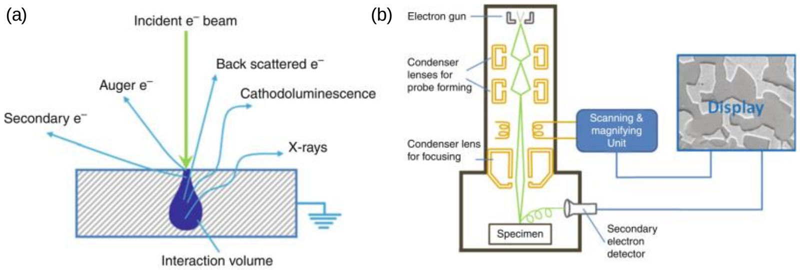

Figure 3.4 (a) Interaction between the specimen and the electron beam; (b) Schematic shown for the SEM. Reprinted with permission from Ni. C, Scanning electron microscopy (SEM). in: Wang Q.J., Chung YW. (eds) Encyclopedia of tribology. Springer, (2013), pp. 2977-2979. Copyright (2013) Springer.

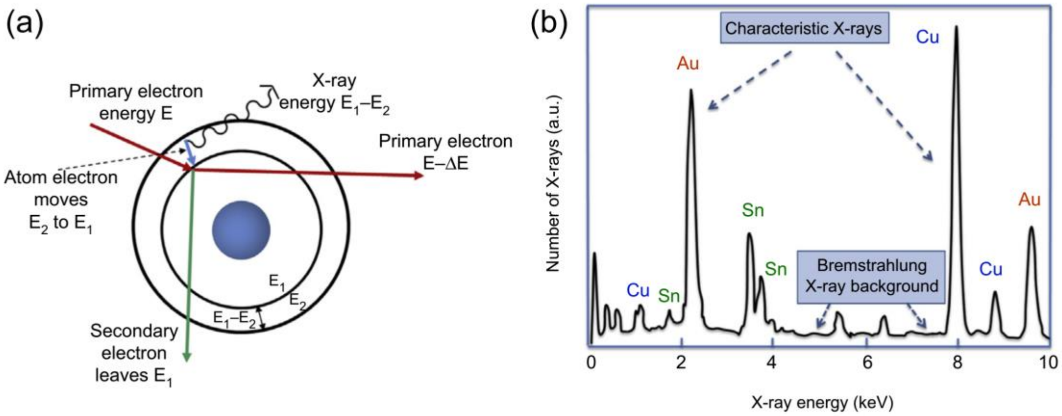

Figure 3.5 (a) Generation of characteristic X-ray photons; (b) Typical EDS characterization results. Reprinted with permission from B. Inkson, Scanning electron microscopy (SEM) and transmission electron microscopy (TEM) for materials characterization, in: Materials characterization using nondestructive evaluation (NDE) methods, Elsevier, 2016, pp. 17-43. Copyright (2016) Elsevier.

Secondary electrons with kinetic energy lower than 50 eV are produced by the ionization of the specimen atoms due to the incident primary electron beam. As secondary electrons are excited from near-surface features (5-10 nm), they can reflect the surface morphology of the specimen. As shown in Figure 3.4(b), the detector can collect the secondary electrons, which can be converted to topographical images on the screen. To obtain a high-quality SEM image, a conductive path is needed for the transfer of static electric charges from the specimen to the ground. The negative static electric charge would result in the flipping of secondary electrons from the specimen surface.[13]

EDS measurements are performed with the characteristic X-ray photons, which are caused by the electron transition. As shown in Figure 3.5(a), the secondary electron in the inner shell is knocked by the incident electron beam, leaving a vacancy in the electron orbit. The electron from the external shell will move to this vacancy, resulting in the generation of the X-ray photon.[14] As the difference between the external and the inner energy level of an atom determines the energy of the X-ray photon, it can be used to identify the elements in the specimen. Figure 3.5(b) shows some typical elements and their corresponding characteristic X-ray photon energies. Through the EDS analysis, the elementary compositions of a specimen can be obtained.

3.3.2 TEM

When a thin specimen is under electron beam irradiation, some electrons can penetrate the specimen and reach the detector. TEM is dependent on these transmitted electrons to reveal the internal microstructure of the sample. A typical TEM system consists of the imaging systems, illumination system, and the lens. To help electrons pass through the specimen, the accelerated voltage is around 200 kV. Two fundamental TEM operations are shown in Figure 3.6.[15] In the diffraction mode, the intermediate lens is focused on the back-focal plane of the objective lens, while it is focused on the image plane in the image mode. Through the selection of different TEM modes, the morphology, microstructural features, electron diffraction pattern and elementals distribution of the specimen can be obtained.

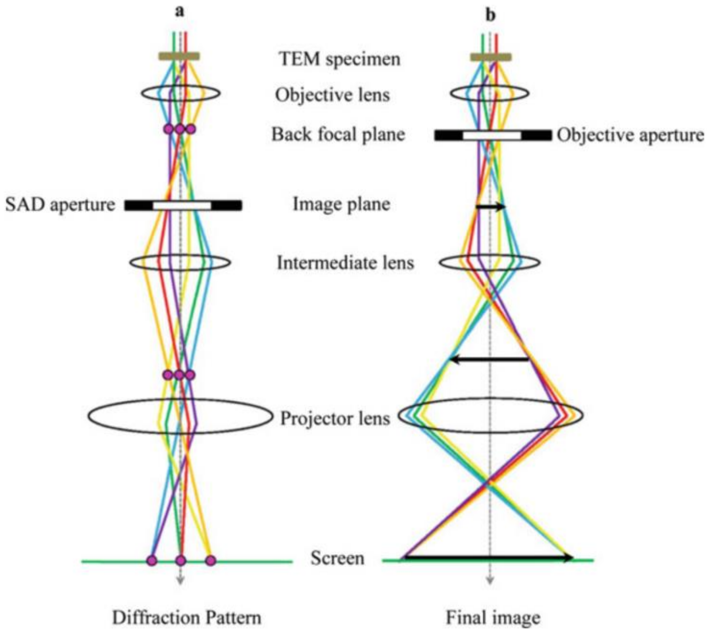

Figure 3.6 Schematic shown for TEM. (a) Diffraction mode; (b) Image mode. Reprinted with permission from F.L. Deepak, E. Anumol, J. Li, Advanced electron microscopy techniques toward the understanding of metal nanoparticles and clusters, in: Metal nanoparticles and clusters, Springer, 2018, pp. 219-287. Copyright (2018) Springer.

3.3.2.1 Bright-field imaging

When using the objective aperture to block scattered electrons, the detectors can only collect unscattered electrons. The bright-field imaging uses these unscattered electron to form a bright contrast in an image. In some areas of the specimen, the electrons scattering is more active than electron penetration, a lower amount of electrons can be collected, forming a dark contrast in the image. Many factors, such as large thickness, grain boundaries, crystal orientation, can contribute to the electron scattering. Thus, this information in a specimen can be reflected by their dark contrast in an image.

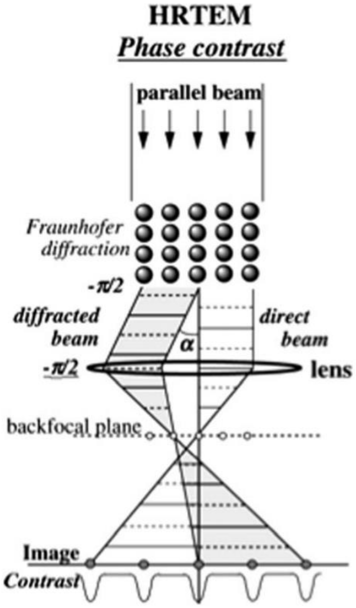

Figure 3.7 Schematic shown for HRTEM. (a) Diffraction mode; (b) Image mode. Reprinted with permission from E. Abe, Chem. Soc. Rev. 41 (2012) 6787-6798. Copyright (2012) Royal Society of Chemistry.

3.3.2.2 HRTEM

Phase contrast, also known as HRTEM, can be used to obtain a higher resolution image of lattice for crystalline materials with a periodic lattice structure. When the sample is very thin, usually less than 100 nm, the amplitude of transmitted electrons remains unchanged.

However, there is a big phase difference between the transmitted and diffracted beam. As simply illustrated in Figure 3.7, phase contrast is obtained with a transmitted beam and a diffraction beam.[16] These interference patterns can be magnified and shown on the screen through the imaging system. Under some conditions, the atoms can be directly investigated by HRTEM.

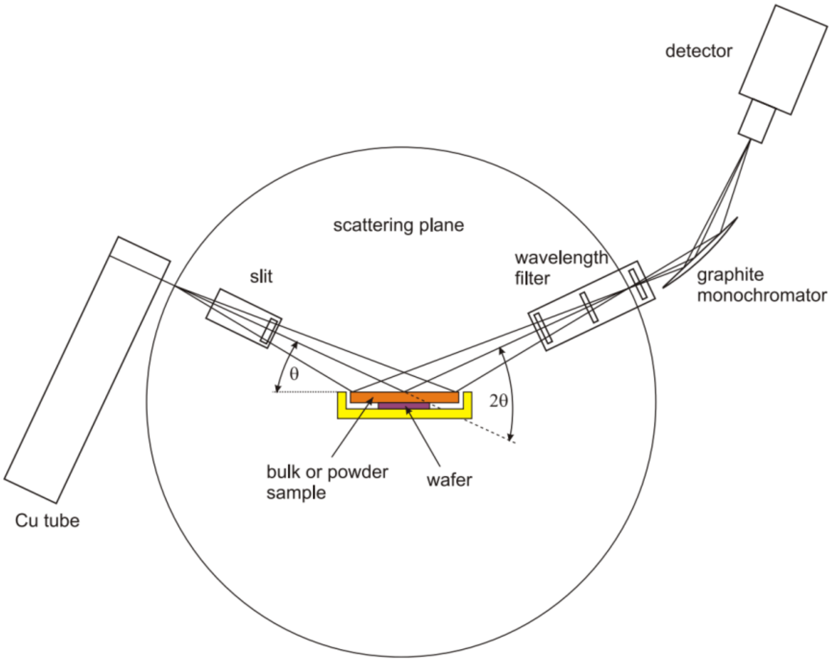

Figure 3.8 Schematic shown for XRD. Reprinted from R. Gilles, D. Mukherji, M. Hoelzel, P. Strunz, D. Toebbens, B. Barbier, Acta Mater. 54 (2006) 1307-1316., Copyright (2006), Elsevier.

3.3.3 XRD

As an effective analysis method, X-ray diffraction (XRD) has been extensively utilized in material science, condensed matter physics, inorganic chemistry and even in archaeology for their strong performance in quantitative and qualitative identification of chemical compounds, crystal structure, and solid phase.[17, 18] As shown in Figure 3.8, an XRD equipment consists of a Cu tube, slit, and a detector. Cu tube is used for the generation of X-rays and the detector is for the collection of the diffracted X-rays after the interaction with the specimen. The slit can reduce the divergence of the incident X-ray. The correlation between the interplanar spacing of a specimen and the diffraction direction of the X-ray is described by the Bragg`s equation ($2d_{hkl} \sin\theta = \lambda$). Thus, diffraction occurs only when the incident angle of the X-ray and the lattice space satisfies the Bragg`s equation. Through measuring the diffraction intensity at different angles, XRD patterns can be obtained. Since the discovery of the Bragg`s equation, a large number of research has been done to acquire different diffraction patterns for various materials. To date, five primary Crystallography databases have been established, such as the Cambridge Structural Database and the Inorganic Crystal Structural Database. In addition, some XRD analysis softwares, such as HighScore, and Jade, have been developed. Therefore, with the help of these databases and software, the XRD pattern obtained in the experiment can be easily discerned through comparison with the standard diffraction pattern.

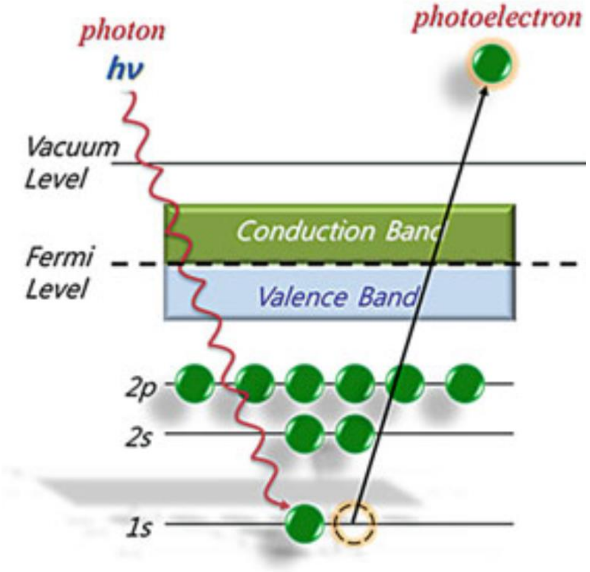

Figure **3.9** Photoelectron effect. Reprinted from R. Gilles, D. Mukherji, M. Hoelzel, P. Strunz, D. Toebbens, B. Barbier, Acta Mater. 54 (2006) 1307-1316. Copyright (2006), with permission from Elsevier.

3.3.4 XPS

XPS is a useful surface analysis method with an analysis depth around 5 nm, which can provide quantitative information of elemental composition, electronic and chemical states of the specimen surface.[19, 20] The core parts of an XPS equipment are the X-ray source and electron energy analyzer. As shown in Figure 3.9, when a specimen is irradiated with an X-ray beam, the core electrons are ejected from the atom. By measuring the difference between the energy of incident photons (hv) and the emitted electrons (E_K), the binding energy (E_B) relative to the Fermi level of a specimen can be calculated by the following equation (4).[21]

$$E_K = hv - E_B - \varphi \qquad (4)$$

φ is the constant work function, which is around 4.5 eV and can be artificially compensated. Besides, the number of ejected photoelectrons is determined by the amount of the elements, thus enabling XPS to be used for quantitative analysis.

References

[1] S.H. Im, Y.T. Lim, D.J. Suh, O.O. Park, *Adv. Mater*. **2002**, *14*, 1367-1369.

[2] X. Chen, Z. Li, J. Ye, Z. Zou, *Chem. Mater*. **2010**, *22*, 3583-3585.

[3] C. Chen, J. Cheng, S. Yu, L. Che, Z. Meng, *J. Cryst. Growth* **2006**, *291*, 135-139.

[4] W. Xiao, W. Liu, X. Mao, H. Zhu, D. Wang, *J. Mater. Chem. A* **2013**, *1*, 1261-1269.

[5] L. Wen, M. Zhou, C. Wang, Y. Mi, Y. Lei, *Adv. Energy Mater*. **2016**, *6*, 1600468.

[6] M. Ortega-López, A. Avila-Garcıa, M. Albor-Aguilera, V.S. Resendiz, *Mater. Res. Bull*. **2003**, *38*, 1241-1248.

[7] H. Pathan, C. Lokhande, *Bull. Mater. Sci*. **2004**, *27*, 85-111.

[8] G.V. Govindaraju, G.P. Wheeler, D. Lee, K.-S. Choi, *Chem. Mater*. **2016**, 29, 355-370.

[9] A. Kafizas, Y. Ma, E. Pastor, S.R. Pendlebury, C. Mesa, L. Francàs, F. Le Formal, N. Noor, M. Ling, C. Sotelo-Vazquez, *ACS Catal*. **2017**, *7*, 4896-4903.

[10] X. Li, J. Yu, J. Low, Y. Fang, J. Xiao, X. Chen, *J. Mater. Chem. A* **2015**, *3*, 2485-2534.

[11] J. Li, N. Wu, *Catal. Sci. Technol*. **2015**, *5*, 1360-1384.

[12] Ni C. Springer **2013**, 2977-2979.

[13] K.H. Kim, Z. Akase, T. Suzuki, D. Shindo, *Mater. Trans*. **2010**, 1005171076-1005171076.

[14] B. Inkson, Elsevier **2016**, 17-43.

[15] F.L. Deepak, E. Anumol, J. Li, Springer **2018**, 219-287.

[16] E. Abe, *Chem. Soc. Rev*. **2012**, *41*, 6787-6798.

[17] A. Chauhan, P. Chauhan, *J. Anal. Bioanal. Tech*. **2014**, 5, 1-5.

[18] R. Talero, *J. Mater. Civ. Eng*. **1990**, *2*, 106-115.

[19] R. Gilles, D. Mukherji, M. Hoelzel, P. Strunz, D. Toebbens, B. Barbier, *Acta Mater*. **2006**, *54*, 1307-1316.

[20] W.J. Oh, J.S. Jang, Y.S. Lee, A. Kim, K.J. Kim, *Appl. Surf. Sci*. **2018**, *432*, 72-77.

[21] S. Almheiri, A.A. Ahmad, B. Le Droumaguet, R. Pires, *Langmuir* **2020,** 36, 74-83.

[22] W. Doh, V. Papaefthimiou, S. Zafeiratos, Springer **2015**, 317-366.

Chapter 4*

Highly Porous SnO_2 Nanosheet Arrays Sandwiched within TiO_2 and CdS Quantum Dots for Efficient Photoelectrochemical Water Splitting

This chapter reports a porous SnO_2 *nanosheets/*TiO_2*/CdS quantum dots (*SnO_2 *NSs/*TiO_2*/CdS QDs) sandwich structure as a "host-guest" photoanode for efficient solar water splitting applications. In this novel photoanode design, the highly porous* SnO_2 *NSs serve as the host skeleton for efficient electron collection, while CdS QDs serve as efficient visible light absorbers. A thin interlayer of* TiO_2 *is introduced for band alignment and reduction of charge recombination. Enhanced photoelectrochemical performance of the as-fabricated photoanode is observed with the introduction of the* TiO_2 *interlayer. The optimized host-guest* SnO_2 *NSs/*TiO_2*/CdS QDs photoanode shows a photocurrent density as high as 4.7 mA* cm^{-2} *at 0 V versus Ag/AgCl, which is 7 times higher than that of the* SnO_2 *NSs/*TiO_2 *reference photoanode (0.7 mA* cm^{-2}*). Furthermore, it also shows a lower charge recombination rate compared to the* SnO_2 *NSs/CdS QDs reference photoanode. Due to the high porosity and transparency of the as developed* SnO_2 *NSs arrays host, it has great potential in various applications, such as solar energy conversion and energy storage.*

---

*This section is published substantially as Z. Wang, et al. *Appl. Surf. Sci*. **2019**, *470*, 800-806.

4.1 Introduction

Photoelectrochemical (PEC) water splitting is an effective method to harvest unlimited solar energy and then convert it into clean and storable chemical energy-hydrogen.[1-3] Recently, the host-guest type nanostructured photoelectrodes have attracted much attention due to their efficient light absorption, high charge collection ability, and effective charge separation.[4-7] For such structures, the host skeletons generally have high conductivity and large specific surface area, while the photoactive guest materials coated on the host skeleton surface would have high visible light absorption efficiency. Various host-guest photoelectrodes, such as WO_3 nanorod/$BiVO_4$,[8] antimony-doped SnO_2 macropore/Fe_2O_3-nanorod[9] and Al-doped ZnO inverse opals/$BiVO_4$,[10] have been reported for PEC water splitting. A host with high conductivity and specific surface area coupled with an efficient light-absorber guest as well as having proper interface band alignment are essential for fabricating efficient host-guest photoelectrodes.[11-15] In PEC water splitting applications, the energy conversion efficiency of the host-guest photoelectrode-based devices could be further enhanced by increasing the electron mobility of the host, light absorption, and decreasing charge recombination rate at the interface.[16-19]

Due to its abundance on earth, high stability, high transparency, and potential for doping with fluorine or antimony, SnO_2 has been considered an ideal host material for photoelectrodes.[20-24] For example, antimony-doped SnO_2 nanorods have reportedly boosted the PEC performance of $BiVO_4$ based photoanode.[25] A fluorine-doped SnO_2/TiO_2 based composite inverse opal structure photoanode has been reported with enhanced PEC performance for solar water splitting applications.[26] Recently, 3D porous SnO_2 nanosheets (NSs) coated on carbon fiber cloth have been applied as lithium batteries and electrocatalyst due to the high specific surface area.[27, 28] SnO_2 NSs grown on transparent conduction oxide, such as fluorine-doped tin oxide (FTO), can be an ideal host skeleton for host-guest type photoelectrodes because of the high stability, high specific surface area as well as the excellent transparency of SnO_2. CdS quantum dots (QDs) have also been extensively employed as absorber guests in various hybrid photoanodes for PEC applications due to their suitable bandgap as well as efficient visible light absorption.[19, 29-

32] The uniform dispersion of CdS QDs on three-dimensional SnO_2 host skeletons, such as screw-like SnO_2 nanostructures/CdS QDs, has been reported for PEC water splitting.[33] However, the energy conversion efficiency of SnO_2/CdS host-guest photoanodes is greatly limited by the high charge recombination rate at the host/guest interface. TiO_2 has been introduced by researchers to reduce the charge recombination at the SnO_2/CdS host-guest interface.[34, 35]

In this work, a 3D SnO_2 NSs/TiO_2/CdS QDs structure was reported as a host-guest photoanode. Uniform and transparent SnO_2 NSs were grown on the FTO glass substrate through a hydrothermal reaction followed by a calcination process. Thin TiO_2 interlayer was conformally coated on SnO_2 NSs by atomic layer deposition (ALD), while CdS QDs were assembled on SnO_2 NSs surface by successive ionic layer adsorption and reaction (SILAR) method. The obtained SnO_2 NSs/TiO_2/CdS QDs host-guest photoanode showed a better PEC performance than SnO_2 NSs/TiO_2 and SnO_2 NSs/CdS QDs reference photoanodes. The enhanced PEC performance of the SnO_2 NSs/TiO_2/CdS QDs can be attributed to intense visible light absorption from CdS QDs, large specific surface area and light trapping effect of the transparent host as well as the excellent band alignment from the ALD TiO_2 interlayer.

4.2 Experimental Section

4.2.1 Materials

Tin (IV) chloride pentahydrate ($SnCl_4 \cdot 5H_2O$), thiourea (C_2H_5NS), isopropanol, cadmium nitrate tetrahydrate and sodium sulfide nonahydrate were purchased from Sigma-Aldrich. FTO substrates (8 Ω/sq) were ordered from Pilkington.

4.2.2 Synthesis of SnO_2 NSs

FTO substrates (1.5 cm x 5 cm) were sequentially sonicated in acetone, methanol, ethanol and deionized (DI) water and dried with nitrogen flow. The precursor solution was prepared based on existing literature with $SnCl_4$ (100 mg), C_2H_5NS (100 mg) and isopropanol (25 ml).[27, 28] Then, four pieces of clean FTO substrates were placed standing at opposing walls of a 100 ml Teflon autoclave containing the as-prepared precursor solution. After sealing, the autoclave was transferred to an oven and kept at 200 °C for 24 h. The obtained SnS_2 nanosheet samples were rinsed with DI water and annealed in an atmospheric environment at 500 °C for 2 h to convert them into SnO_2.

4.2.3 ALD TiO_2

A homebuilt ALD system was utilized to coat a thin film of TiO_2 on the surface of SnO_2 NSs at 80 °C.[36] $TiCl_4$ and water were selected as the Ti and O precursors, respectively. A total of 400 ALD cycles were performed to deposit ~15 nm TiO_2 conformal layers on the SnO_2 NSs. After ALD of TiO_2, the as-prepared samples were annealed at 500 °C in air for 1 hour for the crystallization of TiO_2.

4.2.4 Preparation of CdS QDs

The CdS QDs were coated on SnO_2 NSs/TiO_2 by a SILAR method.[37, 38] Specifically, a SnO_2 NSs/TiO_2 sample was immersed into cadmium nitrate methanol solution for 1 minute and then rinsed with methanol for another minute, followed by drying with nitrogen flow. Next, the sample was immersed into the sodium sulfide solution for 1 minute and rinsed with ethanol solution for another minute, followed by drying with nitrogen flow. The entire procedure was repeated 15 times. Finally, the sample was heated at 400 °C for 30 minutes under argon protection.

4.2.5 Materials Characterization

Field-emission scanning electron microscope (SEM), JEOL, 7600F was utilized to observe the morphology of the as-prepared samples. X-ray diffraction (XRD) pattern was carried out on a Bruker D8 X-ray diffractometer, equipped with Cu Kα radiation source. UV-Vis diffuse reflectance spectra were collected on a Varian, Cary 5000 spectrum system. Raman spectra were collected on a Renishaw in Via Raman system using 477 and 532 nm as the excitation wavelengths.

4.2.6 PEC Measurement

The PEC performance of the as-prepared samples was measured under AM 1.5G simulated sunlight illumination. The photocurrent was collected on an Autolab 270 workstation with a three-electrode electrochemical system. The as-prepared photoanodes were used as the working electrode, Ag/AgCl (3M KCl) were used as the reference electrode, and the platinum mesh was used as the counter electrode. The electrolyte was 0.25 M Na_2SO_3 and 0.35 M Na_2S mixed solution.

4.3 Result and discussion

4.3.1 Fabrication and Characterization

The fabrication process of SnO_2 NSs/TiO_2/CdS QDs photoanodes is schematically shown in Figure 4.1. Firstly, SnS_2 nanosheet arrays are grown on the FTO substrates through a hydrothermal reaction. After calcination, the as-grown SnS_2 nanosheet arrays are converted into 3D vertically aligned SnO_2 NSs. Next, conformal TiO_2 films are deposited on the surface of SnO_2 NSs by ALD. Finally, CdS QDs are deposited on the surface of TiO_2 through the SILAR method.

The amount of chemicals used in the precursor solution played an important role in the coverage of as-grown SnO_2 NSs on FTO substrates, as shown in Figures 4.2(a)-(c). When 40mg of $SnCl_4$ and 40 mg of C_2H_5NS were used for preparing the precursor solution, the SnO_2 NSs coverage of the final product was very poor where a few clusters of SnO_2 NSs were sparsely grown on the FTO surface as shown in Figure 4.2(a). Figures 4.2(b) and 4.2(c) show the SEM images of the SnO_2 NSs samples grown with 80 mg of $SnCl_4$ and C_2H_5NS each and 100 mg of $SnCl_4$ and C_2H_5NS each, respectively. Figure 4.2b clearly shows that the more clusters of SnO_2 NSs were grown on the FTO substrate with an

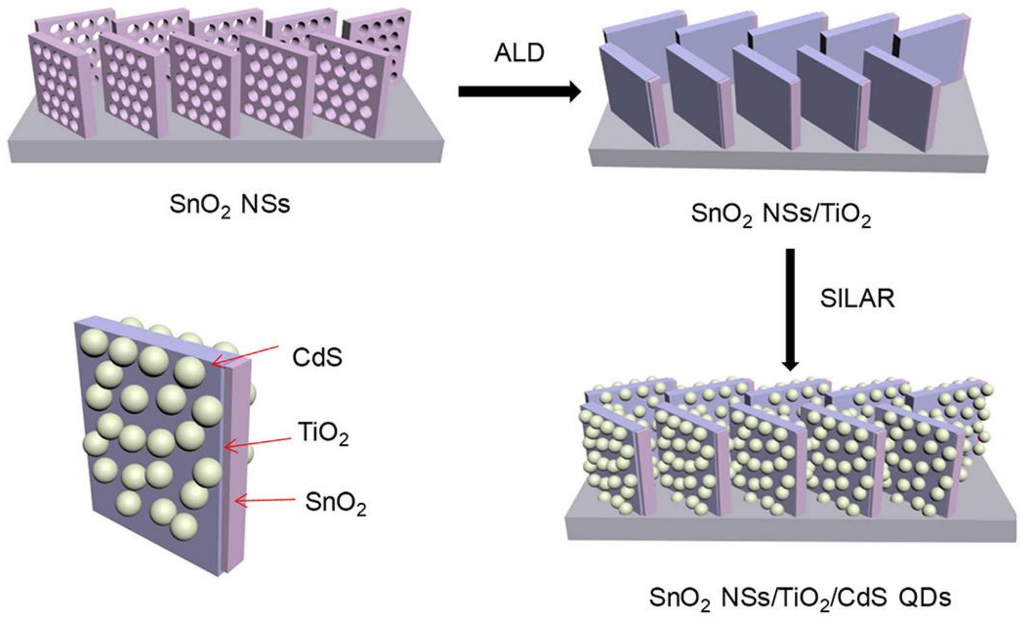

Figure 4.1 Schematic illustration for the fabrication process of the SnO_2 NSs/TiO_2/CdS QDs.

increased amount of chemicals used in the precursor solution. Full coverage of SnO_2 NSs on FTO was achieved when 100 mg of $SnCl_4$ and C_2H_5NS each were used in the precursor solution, as shown in Figure 4.2(c). The SnS_2 NSs would partially peel off from the FTO substrate after rinsing with DI water when even more $SnCl_4$ and C_2H_5NS were used. Before the thermal conversion of SnS_2 NSs to SnO_2 NSs, SnS_2 NSs were adhered to the FTO, indicating that the mechanism for the increased coverage of SnS_2 NSs may involve heterogeneous nucleation and the following growth and aggregation.[39] In the early stage of the hydrothermal reaction, some SnS_2 nuclei were formed on the FTO substrate due to the heterogeneous nucleation. Through the ion-by-ion process, more nuclei would form subsequently, providing sites for the growth of the SnS_2 NSs. When low concentrations of precursors were used, the small density of nuclei with large sizes formed on the FTO substrate, thus only a few clusters of SnS_2 NSs were obtained. With higher concentrations of precursors, a higher density of nuclei of smaller sizes was formed and more SnS_2 NSs were grown on the FTO substrate, which would be converted to SnO_2 NSs after calcination.

The as-prepared SnO_2 NSs nanosheets stand vertically on the FTO substrate, instead of

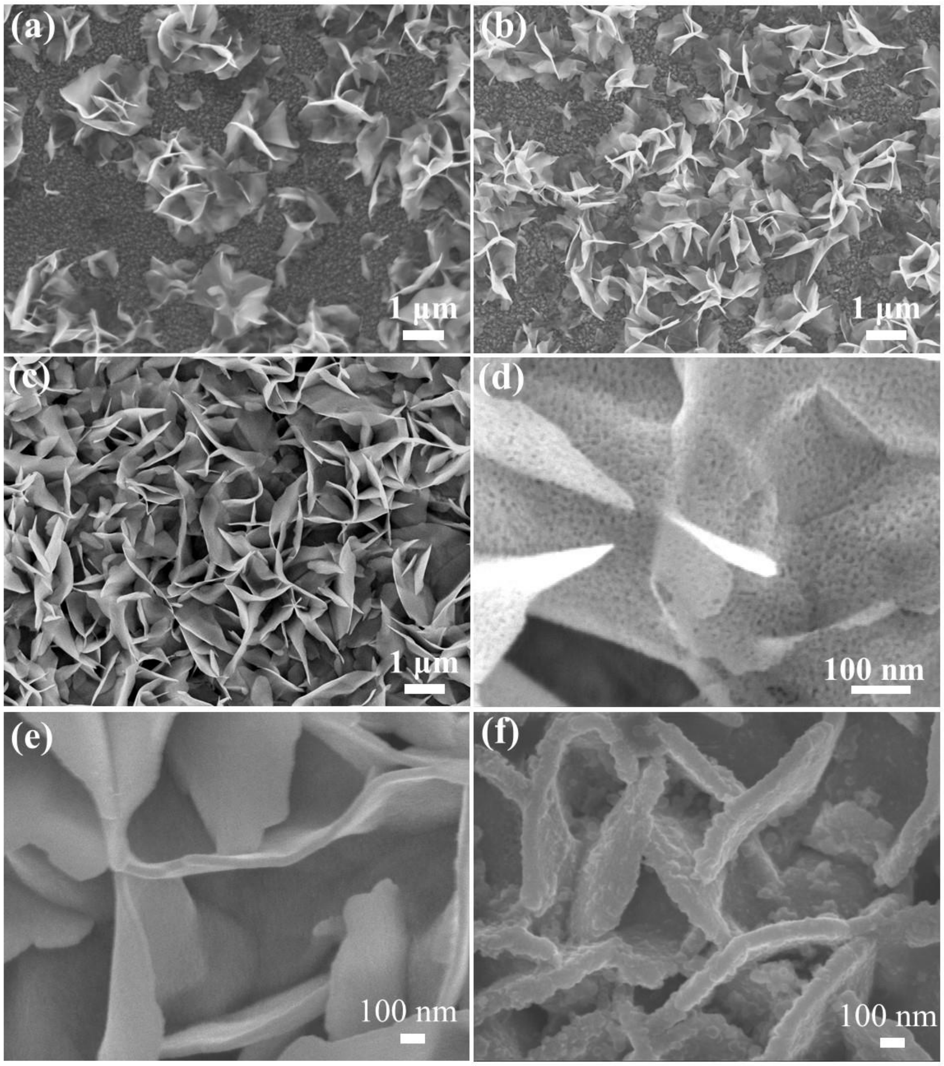

Figure 4.2 SEM images of: (a) SnO_2 NSs prepared with $SnCl_4$ (40 mg) and C_2H_5NS (40 mg); (b) SnO_2 NSs prepared with $SnCl_4$ (80 mg) and C_2H_5NS (80 mg); (c) SnO_2 NSs prepared with $SnCl_4$ (100 mg) and C_2H_5NS (100 mg); (d) SnO_2 NSs with high magnification; (e) SnO_2 NSs/TiO_2; (f) SnO_2 NSs/TiO_2/CdS QDs.

being randomly stacked together, which is beneficial for the loading of photoactive guest materials. The vertical growth of SnS_2 NSs can be ascribed to the formation of metal-thiourea complex, which can decrease the number of free metal ions and sulfur ions, favoring for the oriented growth of SnS_2 NSs.[40] Figure 4.2(d) shows the magnified SEM view of the as-grown SnO_2 NSs. A large number of nano-pores could be observed on the SnO_2 nanosheets, indicating the high porosity of the as-grown SnO_2 NSs. The high specific surface area of the as-fabricated SnO_2 NSs arrays is also beneficial for the loading of more photoactive guest materials and for increasing the contact area of the entire photoanode to electrolytes as well. This enhances the PEC performance of the photoanode.

Although plenty of SnO_2 NSs coated on the FTO substrate have been examined by top-view SEM, some bare areas of FTO substrate may not be occupied by SnO_2 NSs. This can be reflected by the space between adjacent SnO_2 NSs in Figure 4.2(a) and 4.2(b). The exposure of bare FTO substrate to the electrolyte could cause serious interface charge recombination due to the back injection of electrons. As ALD involves a self-limiting growth, it can be used for the deposition of nano-films over 3D nanostructures with excellent conformality. The TiO_2 thin layer was coated on the as-fabricated SnO_2 NSs using ALD, which can also cover all the possible bare FTO areas. In the customized ALD system, N_2 was used as the carrier gas while $TiCl_4$ and H_2O were used as precursors. In each cycle of the ALD process, $TiCl_4$ reacted with the hydroxyl groups on the surface of SnO_2 NSs and formed $Cl_3Ti\text{-}O\text{-}SnO_2$. After the purge of excess $TiCl_4$ and byproduct HCl by N_2, H_2O gas was introduced into the chamber to react with $Cl_3Ti\text{-}O\text{-}SnO_2$. Thus, one layer of TiO_2 film was conformally coated on the SnO_2 NSs while excess H_2O and the byproduct HCl gas were purged by N_2. The thickness of TiO_2 films could be tuned by the number of ALD cycles. From Figures 4.2(e), it could be observed that the structure of SnO_2 NSs remains unchanged, indicating the conformal coating of TiO_2 films over SnO_2 NSs. The average thickness of the SnO_2 NSs increases from a few nanometers to around 30 nm after 400 cycles of ALD TiO_2 films. The uniform coating of TiO_2 films over SnO_2 NSs could also be observed from the smooth surface. It should be mentioned that the TiO_2 film can also be coated on the bare surface area of the FTO substrate. After loading of CdS QDs, the smooth surface becomes coarse and the thickness of the nanosheet further increases to around 40 nm, as shown in Figure 4.2(f). During the SILAR process, Cd^{2+} ions were first adsorbed onto the TiO_2 surface and then reacted with S^{2-} ions to form CdS particles.

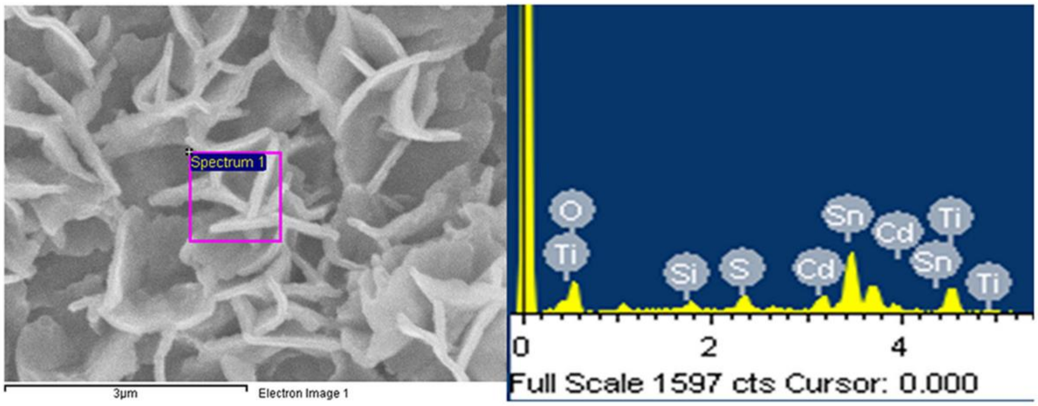

Figure 4.3 EDS characterization of SnO_2 NSs/TiO_2/CdS QDs.

EDS study confirmed the existence of Cd, S, Ti, O and Sn elements in the SnO_2 NSs/TiO_2/CdS QDs photoanode, as shown in Figure 4.3.

XRD was utilized to investigate the crystallinity and constituent of the as-prepared samples. Figure 4.4(a) shows the XRD patterns of bare FTO substrate, SnO_2 NSs, SnO_2 NSs/TiO_2, and SnO_2 NSs/TiO_2/CdS QDs. The diffraction peaks of SnO_2 NSs at 27°, 34°, 38°, 52°, and 55° correspond to (110), (101), (200), (211) and (220) planes of the rutile structure of SnO_2. As both SnO_2 NSs and FTO are comprised of rutile SnO_2, the XRD peaks of SnO_2 NSs and FTO overlap. However, the XRD peaks can be distinguished by their different full width at half maximum. The full width at half maximum of the XRD peaks for SnO_2 NSs is much broader than that for the FTO substrate, indicating that SnO_2 NSs are composed of nanosized SnO_2 crystals, which is consistent with our SEM study, as shown in Figure 4.2(d).

After coating of ALD TiO_2, small but obvious diffraction peaks located at 28°, 36° and 41° could be observed, which can be indexed to the (110), (101) and (200) planes of rutile phase TiO_2. Through the comparison of the XRD patterns of SnO_2 NSs/TiO_2 and SnO_2 NSs/TiO_2/CdS QDs, two new obvious diffraction peaks located at 29° and 44° could be observed after deposition of CdS QDs, and they could be ascribed to the (101) and (110) planes of hexagonal phase CdS. Raman spectroscopy was also utilized to determine the

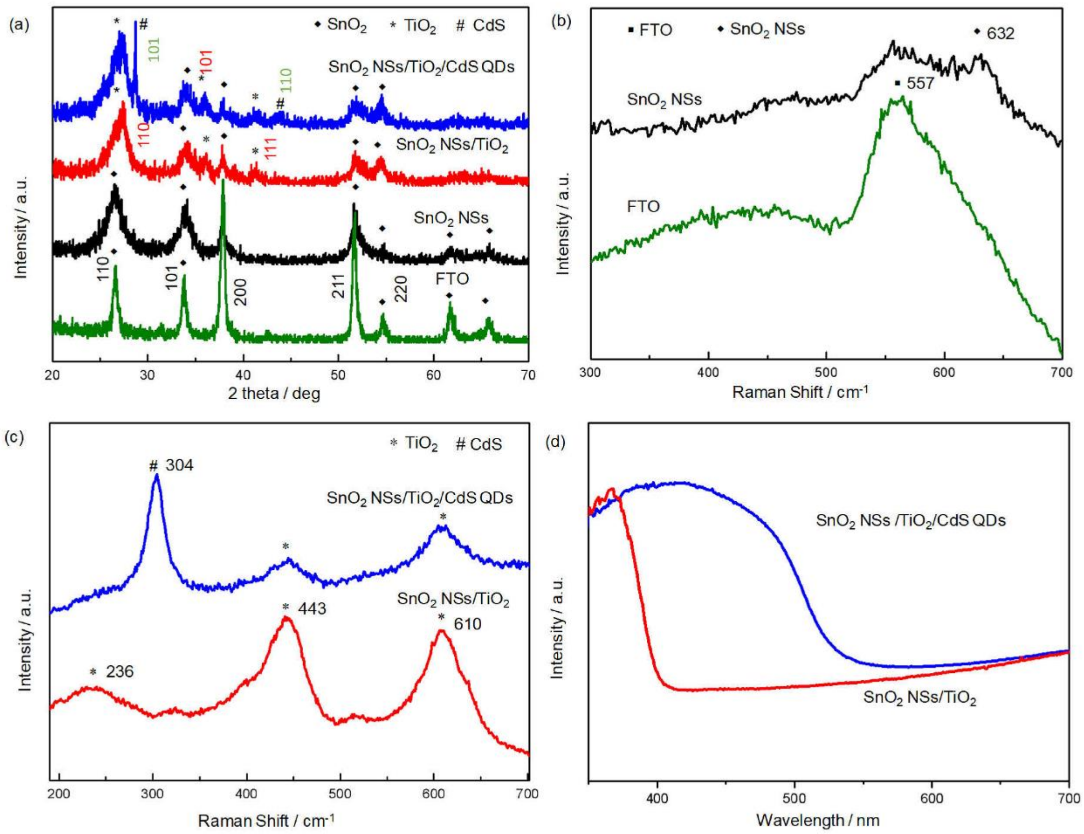

Figure 4.4 (a) XRD patterns of FTO substrate, SnO_2 NSs, SnO_2 NSs/TiO_2 and SnO_2 NSs/TiO_2/CdS QDs; (b) Raman spectra of FTO substrate, SnO_2 NSs; (c) Raman spectra of SnO_2 NSs/TiO_2 and SnO_2 NSs/TiO_2/CdS QDs; (d) UV-Vis absorbance of SnO_2 NSs/TiO_2 and SnO_2 NSs/TiO_2/CdS QDs.

compositions and crystalline phase of the as-prepared hybrid nanostructures. Figure 4.4(b) shows the Raman spectra of the pristine FTO glass and SnO_2 NSs. Due to the high transparency of SnO_2 NSs, the incident light can penetrate through the SnO_2 NSs array and reach the FTO glass, which causes unavoidably strong background signals of the FTO substrate. The pure FTO substrate has one prominent peak located at 557 cm^{-1}.[41] After the growth of SnO_2 NSs, another weak but distinguishable peak emerged at 632 cm^{-1}, which can be indexed to A_{1g} mode of SnO_2. As compared to XRD, Raman could indicate the successful fabrication of SnO_2 NSs on the FTO substrate. Figure 4.4(c) presents the Raman spectra of SnO_2 NSs/TiO_2 and SnO_2 NSs/TiO_2/CdS QDs. In the spectrum of SnO_2 NSs/TiO_2 (red curve in Figure 4.4(c)), the peaks at 236 cm^{-1} (broadband), 443 cm^{-1} (Eg) and 610 cm^{-1} (A1g) can be ascribed to rutile phase of TiO_2.[41] The new peak located at 304

cm^{-1} observed in the Raman spectrum of SnO_2 NSs/TiO_2/CdS QDs corresponds to the 1LO optical phonons of CdS.[35] Thus, both Raman peaks of TiO_2 and CdS can be observed. The disappearance of Raman peaks of SnO_2 at 632 cm^{-1} might be caused by the limited penetration depth of laser used in the Raman testing or the relatively weak signals of SnO_2. The step by step Raman testing as well as XRD characterization indicates the successful fabrication of the composite SnO_2 NSs/TiO_2/CdS QDs.

Figure 4.4(d) shows the UV-Vis absorption spectra. The light absorption of SnO_2 NSs/TiO_2 sample is merely in the UV range due to the large bandgaps of SnO_2 (3.6 eV) and TiO_2 (3.2 eV). After the introduction of CdS QDs, the light absorption edge extended to around 550 nm. This enhanced visible light absorption is due to the smaller bandgap of CdS (2.4 eV). Since visible light accounts for a large part of solar energy, photoanodes with strong visible light absorption should have higher PEC performance for water splitting applications.

4.3.2 PEC performance

The PEC performance of the as-prepared samples was evaluated by linear sweep voltammetry (LSV) with a three-electrode system. As the counter electrode platinum sheet has little effect on the generated photocurrent, the photocurrent density-potential characteristics can be used to determine the performance and the nature of the photoanode. With a higher photocurrent, a larger amount of photogenerated electrons can be involved in the hydrogen evolution on the counter electrode platinum sheet.[42] Figure 4.5(a) shows the comparison of LSV of the SnO_2 NSs/TiO_2, SnO_2 NSs/CdS-QDs, and SnO_2 NSs/TiO_2/CdS QDs photoanodes collected under both dark and illumination conditions. The SnO_2 NSs/TiO_2/CdS QDs photoanodes show a much better PEC performance than the SnO_2 NSs/TiO_2 and SnO_2 NSs/CdS QDs photoanodes. The SnO_2 NSs/TiO_2/CdS QDs showed a photocurrent density of 4.7 mA cm^{-2} at 0 V vs. AgCl, while SnO_2 NSs/TiO_2 only showed a photocurrent density of 0.7 mA cm^{-2}. The reason behind this is due to the increases the light absorption in the visible range, which is consistent with our UV-Vis

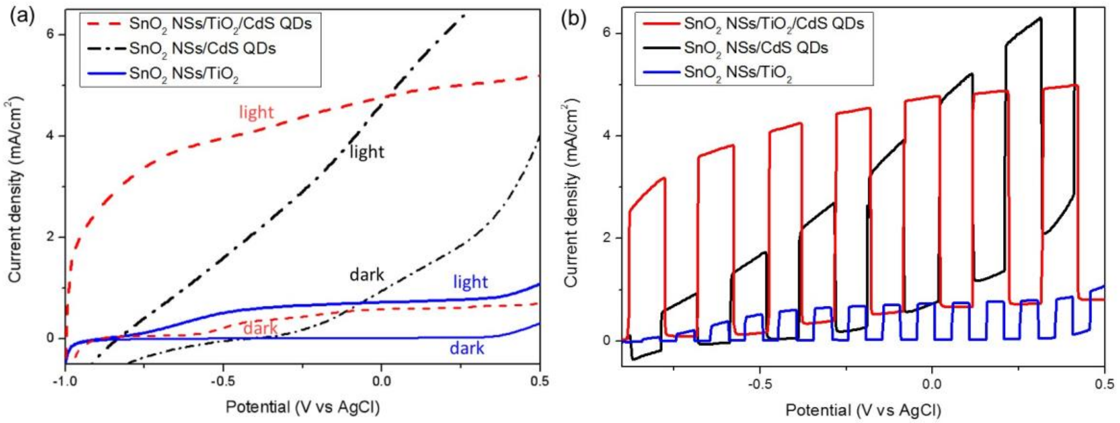

Figure 4.5 (a) Linear sweep voltammetry measurement of SnO_2 NSs/TiO_2, SnO_2 NSs/CdS QDs and SnO_2 NSs/TiO_2/CdS QDs; (b) Linear sweep voltammetry measurement of SnO_2 NSs/TiO_2, SnO_2 NSs/CdS QDs and SnO_2 NSs/TiO_2/CdS QDs under chopped light illumination.

study. The onset potential of SnO_2 NSs/TiO_2/CdS-QDs photoanode has also dropped from -0.75 V for SnO_2 NSs/TiO_2 photoanode to -1 V and that could also be due to the introduction of CdS QDs in the photoanode. To further determine the role of the TiO_2 interlayer, the linear sweep curve of SnO_2 NSs/CdS QDs photoanode was also collected, as seen in the black curve in Figure 4.5(a). The photocurrent density of SnO_2 NSs/TiO_2/CdS QDs photoanode is much larger than that of the SnO_2 NSs/CdS QDs photoanode with the applied voltage near the onset potential of SnO_2 NSs/CdS QDs photoanode at around -0.8 V vs. AgCl. This could be explained by the charge recombination rate of SnO_2 NSs/CdS QDs photoanode being much higher than that of the photoanode with the TiO_2 interlayer. The introduction of the TiO_2 interlayer is beneficial to the heterojunction formation between CdS and SnO_2. It can also help to insulate bare FTO substrate from direct contact with the electrolyte and thus suppress the interface charge recombination. With an increased applied voltage, the photocurrent difference between the SnO_2 NSs/CdS QDs and SnO_2 NSs/TiO_2/CdS QDs photoanodes becomes smaller, which is understandable as the increased applied voltage can depress the charge recombination process.[43] Figure 5.5(b) shows the LSV of the SnO_2 NSs/TiO_2, SnO_2 NSs/CdS QDs and SnO_2 NSs/TiO_2/CdS QDs electrodes under chopped light illumination, which agrees well with the difference between their photocurrent and dark current showed in Figure 4.5(a).

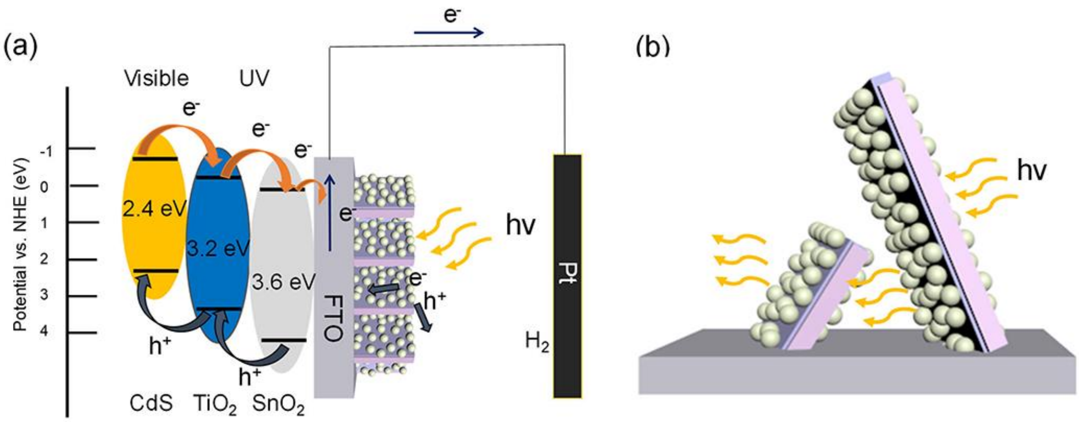

Figure 4.6 (a) Scheme of band alignment and charge transfer process in the SnO_2 NSs/TiO_2/CdS QDs photoanode. The bandgap of CdS, TiO_2 and SnO_2 are 2.4 eV, 3.2 eV and 3.6 eV, respectively; (b) Scheme of light transmission inside the hybrid SnO_2 NSs/TiO_2/CdS QDs photoanode.

The band alignment of SnO_2 NSs/TiO_2/CdS QDs photoanode is schematically shown in Figure 4.6(a). The band edge position of SnO_2, TiO_2 and CdS are favorable for charge transfer.[34, 35] Under light illumination, photo-generated electrons of CdS are sequentially transported from its conductive band (CB) level to lower CB of TiO_2 and then to even lower CB of SnO_2. These photogenerated electrons would then flow to the conductive FTO substrate and finally to the Pt electrode to produce H_2. The holes transfer conversely and finally reach to the valence band of CdS to join the oxidation process. The enhancement in the photocurrent of SnO_2 NSs/TiO_2/CdS QDs photoanode compared to that of SnO_2 NSs/TiO_2 can be ascribed to the visible light absorption of CdS QDs with a bandgap of 2.4 eV, while TiO_2 (3.2 eV) and SnO_2 (3.6 eV) can only absorb UV light. As visible light accounts for a larger part in the sunlight as compared to UV light, with the same light illumination, more absorption of visible light means there will be more photogenerated holes and electrons in the photoanode. In addition, the good band alignment between CdS QDs, TiO_2 and SnO_2 provides fast and direct electron pathways, hence enhancing charge separation and reducing the charge recombination rate. Furthermore, the vertically aligned sheet-like and porous structures provide large surface area for the loading of CdS QDs without stacking.

Table 4.1 Comparison of PEC performance of reported SnO_2/CdS based nanostructured photoanode.

SnO_2/CdS based photoanodes	Electrolyte	Photocurrent density [mA cm^{-2}]$^{a)}$	Remarks
SnO_2 NSs/TiO_2/CdS QD	0.25 M Na_2S + 0.35 M Na_2SO_3	4.7	This work
SnO_2 nanorods/CdS films		1.38	[45]
SnO_2/TiO_2 sea urchinlike nanotube arrays/CdS QDs		2.8	[34]
SnO_2 nanobowl arrays/CdS-NRs		3.5	[46]
SnO_2 nanowires/TiO_2 nanoneedles/CdS QDs		9	[35]
Screw-like SnO_2 nanostructures/CdS QDs		10	[33]

a) The photocurrent density was collected at 0.9 V vs. reversible hydrogen electrode under AM 1.5 illumination (100 mW cm^{-2}).

Transparent SnO_2 NSs also ensure effective light transmission inside the hybrid nanostructures, as schematically shown in Figure 4.6(b). The light illuminated on one side of a single hybrid nanosheet can penetrate through the transparent SnO_2 NSs and reach the CdS and TiO_2, and even the adjacent dwarf nanosheets, on the other side. This means that the incident light can be absorbed for multiple times by CdS QDs. The photocurrent of some SnO_2/CdS based hybrid photoanodes collected at 0.9 V versus RHE with AM 1.5 illumination (100 mW cm^{-2}) is summarized in Table 4.1. Although the photocurrent of the as-prepared SnO_2 NSs/TiO_2/CdS QDs is not the highest, the improved PEC performance due to the introduction of TiO_2 layer points out a possible solution to enhance PEC performance of CdS and other existing semiconductors. The PEC performance of the SnO_2 NSs/TiO_2/CdS QDs photoanode could be further improved by increasing the conductivity of SnO_2 NSs host via doping with antimony or fluorine. Besides, CdS QDs would suffer from serious photocorrosion due to its more negative E_d than $E(H_2O/O_2)$. The photo stability of CdS QDs could be improved by introduction of amorphous TiO_2 or SiO_2, which will be investigated in the next chapter.

4.4 Conclusion

In summary, a SnO_2 NSs/TiO_2/CdS QDs host-guest type photoanode has been prepared for PEC applications through a combination of hydrothermal method, ALD technique and typical SILAR method. The density of the as-grown SnO_2 NSs can be tuned by the amount of chemicals used in the precursor solution for the hydrothermal reaction. To reduce the charge recombination rate between CdS guest and SnO_2 host, a thin TiO_2 interlayer has been introduced for band alignment of the host-guest photoanode. The optimized SnO_2 NSs/TiO_2/CdS QDs show better PEC performance compared to SnO_2 NSs/TiO_2 and SnO_2 NSs/CdS QDs reference photoanodes. This enhanced PEC performance is attributed to the high visible light absorption of the CdS guest, large specific surface area and effective light trapping effect from the SnO_2 NSs host as well as the good band alignment from the ALD TiO_2 interlayer.

References

[1] X. Zhang, B. Zhang, Y. Luo, X. Lv, Y. Shen, *Appl. Surf. Sci*. **2017**, *391*, 288-294.

[2] C. Jiang, S.J. Moniz, A. Wang, T. Zhang, J. Tang, *Chem. Soc. Rev*. **2017**, *46*, 4645-4660.

[3] X. Li, P.S. Bassi, P.P. Boix, Y. Fang, L.H. Wong, *ACS Appl. Mater. Interface* **2015**, *7*, 16960-16966.

[4] X. Li, J. Yu, J. Low, Y. Fang, J. Xiao, X. Chen, *J. Mater. Chem. A* **2015**, *3*, 2485-2534.

[5] S.J. Moniz, S.A. Shevlin, D.J. Martin, Z.-X. Guo, J. Tang, *Energy Environ. Sci*. **2015**, *8*, 731-759.

[6] C. Ding, J. Shi, Z. Wang, C. Li, *ACS Catal*. **2016**, *7*, 675-688.

[7] Y. Zhou, L. Zhang, L. Lin, B.R. Wygant, Y. Liu, Y. Zhu, Y. Zheng, C.B. Mullins, Y. Zhao, X. Zhang, *Nano Lett*. **2017**, *17*, 8012-8017.

[8] P.M. Rao, L. Cai, C. Liu, I.S. Cho, C.H. Lee, J.M. Weisse, P. Yang, X. Zheng, *Nano Lett*. **2014**, *14*, 1099-1105.

[9] Y.F. Xu, H.S. Rao, B.X. Chen, Y. Lin, H.Y. Chen, D.B. Kuang, C.Y. Su, *Adv. Sci*.

2015, *2*,1500049.

[10] L. Zhang, E. Reisner, J.J. Baumberg, *Energy Environ. Sci*. **2014**, *7*, 1402-1408.

[11] X.D. Wang, Y.F. Xu, B.X. Chen, N. Zhou, H.Y. Chen, D.B. Kuang, C.Y. Su, *ChemSusChem* **2016**, *9*, 3012-3018.

[12] M.S. Prévot, Y. Li, N. Guijarro, K. Sivula, *J. Mater. Chem. A* **2016**, *4*, 3018-3026.

[13] S. Cao, X. Yan, Z. Kang, Q. Liang, X. Liao, Y. Zhang, *Nano Energy* **2016**, *24*, 25-31.

[14] Z. Zhang, Y. Li, X. Jiang, W. Han, M. Xie, F. Wang, E. Xie, *Nanoscale* **2017**, *9*, 14015-14022.

[15] S.-Y. Chen, J.-S. Yang, J.-J. Wu, *ACS Appl. Energy Mater*. **2018**, *1*, 2143-2149.

[16] S.K. Karuturi, J. Luo, C. Cheng, L. Liu, L.T. Su, A.I.Y. Tok, H.J. Fan, *Adv. Mater*. **2012**, *24*, 4157-4162.

[17] I. Kondofersky, H.K. Dunn, A. Müller, B. Mandlmeier, J.M. Feckl, D. Fattakhova-Rohlfing, C. Scheu, L.M. Peter, T. Bein, *ACS Appl. Mater. Interface* **2015**, *7*, 4623-4630.

[18] Y. Li, X. Wei, B. Zhu, H. Wang, Y. Tang, T.C. Sum, X. Chen, *Nanoscale* **2016**, *8*, 11284-11290.

[19] R.-B. Wei, P.-Y. Kuang, H. Cheng, Y.-B. Chen, J.-Y. Long, M.-Y. Zhang, Z.-Q. Liu, *ACS Sustain. Chem. Eng.* **2017**, *5*, 4249-4257.

[20] G. Yun, M. Balamurugan, H.-S. Kim, K.-S. Ahn, S.H. Kang, *J. Phys. Chem. C* **2016**, *120*, 5906-5915.

[21] Y. Gun, G.Y. Song, V.H.V. Quy, J. Heo, H. Lee, K.-S. Ahn, S.H. Kang, *ACS Appl. Mater. Interface* **2015**, *7*, 20292-20303.

[22] I.A. Cordova, Q. Peng, I.L. Ferrall, A.J. Rieth, P.G. Hoertz, J.T. Glass, *Nanoscale* **2015**, *7*, 8584-8592.

[23] L. Wang, A. Palacios - Padrós, R. Kirchgeorg, A. Tighineanu, P. Schmuki, *ChemSusChem* **2014**, *7*, 421-424.

[24] S. Zhou, R. Tang, L. Zhang, L. Yin, *Electrochim. Acta* **2017**, *248*, 593-602.

[25] L. Zhou, C. Zhao, B. Giri, P. Allen, X. Xu, H. Joshi, Y. Fan, L.V. Titova, P.M. Rao, *Nano Lett*. **2016**, *16*, 3463-3474.

[26] Z. Wang, X. Li, H. Ling, C.K. Tan, L.P. Yeo, A.C. Grimsdale, A.I.Y. Tok, *Small* **2018**, *14*, 1800395.

[27] F. Li, L. Chen, G.P. Knowles, D.R. MacFarlane, J. Zhang, *Angew. Chem. Int. Edit*.

2017, *56*, 505-509.

[28] M. Wang, L. Fan, X. Wu, D. Tian, J. Cheng, Y. Qiu, H. Wu, B. Guan, N. Zhang, K. Sun, *J. Mater. Chem. A* **2017**, *5*, 19613-19618.

[29] F. Zhan, W. Liu, H. Li, Y. Yang, M. Wang, *Appl. Surf. Sci*. **2018**, *45*, 476-483.

[30] S.K. Karuturi, R. Yew, P.R. Narangari, J. Wong-Leung, L. Li, K. Vora, H.H. Tan, C. Jagadish, *Nano Futures* **2018**, *2*, 015004.

[31] Y. Liu, Z. Kang, H. Si, P. Li, S. Cao, S. Liu, Y. Li, S. Zhang, Z. Zhang, Q. Liao, *Nano Energy* **2017**, *35*, 189-198.

[32] S. Ren, Y. Wang, G. Fan, R. Gao, W. Liu, *Nanotechnology* **2017**, *28*, 465403.

[33] Z. Zhang, C. Gao, Z. Wu, W. Han, Y. Wang, W. Fu, X. Li, E. Xie, *Nano Energy* **2016**, *19*, 318-327.

[34] C. Li, H. Zhang, C. Cheng, *RSC Adv*. **2016**, *6*, 37407-37411.

[35] C. Gao, Z. Zhang, X. Li, L. Chen, Y. Wang, Y. He, F. Teng, J. Zhou, W. Han, E. Xie, *Sol. Energ. Mat. Sol. C* **2015**, *141*, 101-107.

[36] X. Li, M. Puttaswamy, Z. Wang, C. Kei Tan, A.C. Grimsdale, N.P. Kherani, A.I.Y. Tok, *Appl. Surf. Sci*. **2017**, *422*, 536-543.

[37] S.K. Karuturi, C. Cheng, L. Liu, L.T. Su, H.J. Fan, A.I.Y. Tok, *Nano Energy* **2012**, *1*, 322-327.

[38] C. Cheng, S.K. Karuturi, L. Liu, J. Liu, H. Li, L.T. Su, A.I.Y. Tok, H.J. Fan, *Small* **2012**, *8*, 37-42.

[39] S. Peng, F. Cheng, J. Liang, Z. Tao, J. Chen, *J. Alloys. Compd*. **2009**, *481*, 786-791.

[40] C. Tang, Y. Zhang, J. Su, C. Wang, R. Sun, J. Zhang, G. Li, *Solid State Sci*. **2016**, *51*, 24-29.

[41] W.-Q. Fan, X.-Q. Yu, S.-Y. Song, H.-Y. Bai, C. Zhang, D. Yan, C.-B. Liu, Q. Wang, W.-D. Shi, *CrystEngComm* **2014**, *16*, 820-825.

[42] G.V. Govindaraju, G.P. Wheeler, D. Lee, K.-S. Choi, *Chem. Mater*. **2016**, *29*, 355-370.

[43] F. Le Formal, N. Tétreault, M. Cornuz, T. Moehl, M. Grätzel, K. Sivula, *Chem. Sci*. **2011**, *2*, 737-743.

[44] L. Wang, W. Wang, Y. Chen, L. Yao, X. Zhao, H. Shi, M. Cao, Y. Liang, *ACS Appl. Mater. Interfaces* **2018**, *10*, 11652-11662.

[45] X. Zhou, W. Fu, H. Yang, Y. Mu, J. Ma, L. Tian, B. Zhao, M. Li, Mater. Lett. **2013**, *93*, 95-98.

[46] W. Wang, C. Jin, L. Qi, *Small* **2018**, *14*, 1801352.

Chapter 5*

Amorphous TiO_2 Coated Hierarchical WO_3 Nanosheet/CdS Nanorod Arrays for Improved Photoelectrochemical Performance

This chapter demonstrates hierarchical WO_3 *nanosheet/CdS nanorod (*WO_3*-NS/CdS-NR) arrays as a type-II heterojunction photoanode for improved photoelectrochemical (PEC) water splitting. Due to the synergistic effect of different constituents in the novel hierarchical structure,* WO_3*-NS/CdS-NR arrays as a photoanode yield a photocurrent density of 5.4 mA* cm^{-2} *at 0.8 V versus reversible hydrogen electrode for sulfite oxidation. This is 12 times that of* WO_3*-NS arrays (0.45 mA* cm^{-2}*) and 3 times that of CdS-NR arrays (1.85 mA* cm^{-2}*). In this hybrid* WO_3*-NS/CdS-NR arrays photoanode, the favorable heterojunction between* WO_3 *and CdS enhances the charge separation efficiency and widens the light absorption spectrum. Furthermore, the optimization of the loading amount and size of CdS-NRs allows for a larger specific surface area as well as more effective light scattering, which further improves the PEC performance of* WO_3*-NS/CdS-NR arrays. Finally, the coating of an ultrathin layer of amorphous* TiO_2 *also enhances the photostability of* WO_3*-NS/CdS-NR arrays.*

---

*This section is published substantially as Z. Wang, et al. *Appl. Surf. Sci*. **2019**, *490*, 411-419.

5.1 Introduction

Photoelectrochemical (PEC) water splitting allows the direct conversion of solar energy into renewable hydrogen fuel. Since hydrogen is considered an environmentally-friendly and storable energy carrier, PEC water splitting has become one of the most promising methods for tackling global warming and energy shortage.[1-3] In a PEC device, the photoanode is responsible for oxygen evolution while the photocathode is responsible for hydrogen generation.[4] Efforts have mostly been devoted to the fabrication of efficient photoanodes for the complex oxygen evolution process.[5] To date, various semiconductors, such as Fe_2O_3, [6] $BiVO_4$,[7] TiO_2,[8] WO_3,[9] and CdS,[10] have been investigated as photoanode materials. However, none of these materials can simultaneously fulfill all the requirements for an ideal photoanode in terms of efficient visible light absorption, suitable band edge position, high photo-stability, large electrical conductivity and hole diffusion length.[11, 12] Several techniques, such as the development of novel nanostructure,[13] heterojunction engineering,[14] have thus been proposed to enhance PEC performance.

Among these materials, CdS with a direct bandgap of 2.4 eV has attracted much attention in PEC water splitting applications for its efficient visible light absorption and favorable band edge position.[15, 16] Various CdS nanostructures, such as CdS quantum dots (QDs),[17, 18] CdS nanosheets (NSs),[19] and CdS nanorods (NRs),[20] have been used to fabricate different photoanodes. Owing to the direct electron transport pathways, large specific surface area, and short hole transfer path length, CdS-NRs have recently been reported for their better PEC performance than other CdS nanostructures.[21, 22] However, the self-oxidation of CdS by photogenerated holes and low light scattering ability of pristine CdS-NR arrays still posed a significant challenge in the production of highly efficient CdS-NRs based photoanodes, [23, 24] To tackle these problems, CdS-NRs-based heterojunctions, such as CdS-NRs/Cu_2O p-n heterojunctions,[21] and CdS-NRs/SnS_x nanosheets heterojunction,[25] were reported to have enhanced charge separation efficiency. In addition, some well-designed CdS-NRs-based nanostructures, such as CdS-NRs@SnO_2 nanobowl arrays,[23] were proposed to increase the light scattering ability. Recently, the passivation layer with the ability to reduce surface defect states and mitigate the photo corrosion of semiconductors have attracted much attention.[26] Studies on the combination of the passivation layer with novel CdS-NRs-based nanostructures could provide the necessary insight into concurrently achieving efficient light absorption, enhanced charge separation efficiency and prolonged photostability. WO_3 is one of the most promising semiconductors for fabrication of type II heterojunctions when combined with other semiconductors, such as $BiVO_4$,[27] Fe_2O_3,[28] and Bi_2S_3,[29] due to its superior electron transport properties and high photostability. In WO_3-based type II heterojunctions, WO_3 not only enables accelerated charge separation and thus suppresses the internal charge recombination, but also plays the role of an electron conductor for quick transfer of photogenerated electrons to the conductive substrate.[30-32] The WO_3/CdS heterostructures in the form of WO_3-nanowires/CdS-film,[33] platelike WO_3/TiO_2/CdS-QDs,[34] platelike $WO_3/CdWO_4$/CdS-QDs,[35] and WO_3/CdS-QDs,[36] have also been investigated for potential applications as photoanodes. However, the combination of WO_3 and CdS-NRs as a heterojunction photoanode, which has the potential to further enhance PEC performance due to the superior characteristics of CdS-NRs, has yet to be investigated.

Recently, the nanosheet/nanorod (NS/NR) hierarchical structure has been utilized in the fabrication of various heterojunction photoanodes. This hierarchical structure has high light utilization efficiency and large effective surface area, which are both beneficial for the improvement of the PEC efficiency.[37, 38] Thus, in this work, we developed WO_3-NS/CdS-NR arrays as a novel type II heterojunction photoanode for efficient PEC water splitting, which showed a higher photocurrent than pristine CdS-NR arrays and WO_3-NS arrays. The enhanced photocurrent can be ascribed to the enhanced charge separation efficiency due to the strong electrons collection by WO_3 and the formation of a heterojunction between CdS and WO_3. The high specific surface area and effective light scattering due to the well-designed NR/NS nanostructure also contributed to the improved PEC performance. The photostability of the WO_3-NS/CdS-NR arrays was further improved by an ultrathin layer of amorphous TiO_2.

5.2. Experimental section

5.2.1 Materials

Fluorine-doped tin oxide (FTO) substrates were purchased from USA Pilkington (Model: Tec-7, 8 Ω sq^{-1}). Tungstic acid (H_2WO_4), poly(vinyl alcohol) (PVA), oxalic acid, acetonitrile, cadmium nitrate, glutathione, thiourea, urea, and hydrochloric acid were obtained from Sigma-Aldrich. Hydrogen peroxide (H_2O_2) was acquired from VWR International.

5.2.2 Fabrication of WO_3-NS Arrays

WO_3-NS arrays on FTO glass substrate were prepared according to previous reports, which involves the preparation of WO_3 seed layer and hydrothermal growth of WO_3-NS arrays.[39] Three solutions were prepared and then labeled as solution A, B, and C. Solution A was prepared with H_2WO_4 (1.25 g), PVA (0.5 g) and H_2O_2 (20 mL) and stirred at 80 °C for 1 h. Solution B was prepared with H_2WO_4 (1.25 g), H_2O_2 (17 mL) and deionized (DI) water (25 mL). After stirring at 90 °C for 1 h, more DI water was then added to dilute the solution to make up a volume of 100 mL. Solution C was prepared with oxalic acid (20 mg), urea (20 mg), solution B (3 ml), HCl (0.5 mL, 6 M) and acetonitrile (12.5 mL).

WO_3 seed layer was coated onto a clean FTO glass substrate by spin-coating. 100 µL of solution A was dropped on the FTO glass and spun at 500 rpm for 2 min. This process was repeated once more before annealing at 500 °C for 2 h in the air.

WO_3-NS arrays were fabricated on the WO_3 seed layer by a hydrothermal reaction. Solution C was first added into a Teflon-lined stainless autoclave (45 mL, Parr). Then, a piece of FTO glass coated with WO_3 seed layer was put into solution C with the seed layer facing down. Finally, the autoclave was placed in the oven at 180 °C for 2 h, followed by a post-heat treatment at 500 °C in air for 2 h.

5.2.3 Fabrication of WO_3-NS/CdS-NR Arrays

CdS-NRs were grown on the surface of WO_3-NS arrays by a hydrothermal reaction. The precursor solution, which is composed of cadmium nitrate (69 mg), thiourea (17 mg), glutathione (41 mg) and DI water (15 ml), was first added into a Teflon-lined stainless autoclave (23 mL, Parr). Then, a piece of FTO glass coated with WO_3-NS arrays was immersed in the precursor with the conductive surface facing down. Finally, the sealed autoclave was placed in an electric oven at 200 °C for 1 to 4 h, followed by annealing at 450 °C for 1h under Ar atmosphere.

A reference was prepared using the same method, but the CdS-NRs were grown on pure FTO substrate instead.

5.2.4 Fabrication of WO_3-NS/CdS-NR Arrays/Amorphous TiO_2

A customized atomic layer deposition (ALD) system was utilized for the deposition of a thin film of TiO_2 on the surface of WO_3-NS/CdS-NR arrays at 80 °C [40]. DI water and titanium tetrachloride ($TiCl_4$) were utilized as the oxygen and titanium precursors, respectively. In each ALD cycle, $TiCl_4$ pulse, H_2O pulse and purging time were set as 0.25 s, 0.06 s, 4 s, respectively. 10, 20, 30 and 40 ALD cycles were performed to deposit different thicknesses of TiO_2 films on the surface of the WO_3-NS/CdS-NR arrays.

5.2.5 Materials Characterization

Field-emission scanning electron microscope (FESEM, JEOL, JSM 7600F), Transmission electron microscope (TEM, JEOL, 2010) and high-resolution Transmission electron microscope (HRTEM, JEOL, 2010) were used to investigate the morphology and microstructure of the as-prepared samples. X-ray photoelectron spectroscopy (XPS) with a multichannel energy analyzer (SPECS Phoibos 100 MCD-5) and a monochromatic Ma Kα source at 1253 eV was used to analyze the composition and surface chemical state. C 1s (284.5 eV) was used for calibration. X-ray diffraction (XRD) pattern was obtained by using the X-ray diffractometer (Bruker D8). The radiation source is Cu-Kα. UV-Vis absorption spectra were measured on a spectrophotometer (Varian, Cary 5000).

5.2.6 PEC Measurement

PEC performance of the as-prepared samples was measured by a testing system consisting of a workstation (Autolab 270), a solar simulator equipped with an air mass 1.5 filter (300W Xe lamp, Newport) and a three-electrode electrochemical cell. The power of the output light was calibrated to 1 sun illumination (air mass 1.5, 100 mW cm^{-2}) by a standard Si solar cell. In the three-electrode electrochemical cell, a mix solution of 0.25 M Na_2SO_3 and 0.35 M Na_2S was used as the electrolyte. The working electrode is the as-prepared sample. The reference electrode and the counter electrode are Ag/AgCl electrode and platinum mesh, respectively. Electrochemical impedance spectroscopy (EIS) data were measured by the same testing system by applying a bias of 0.8 V versus reversible hydrogen electrode (RHE) over a frequency range from 10^{-1} to 10^{5} Hz with a 10 mV amplitude.

5.3 Results and discussion

5.3.1 Fabrication and Characterization

The fabrication process of the WO_3-NS/CdS-NR arrays is illustrated in Figure 5.1. WO_3-NS arrays were grown on a WO_3 seed layer coated FTO substrate through a hydrothermal reaction. Prior to the growth of the CdS-NRs, a calcination process was performed not only for the crystallization of WO_3 but also for better cohesion between WO_3-NS arrays and FTO substrate, which is crucial to the secondary growth of CdS-NRs. Subsequently, the direct hydrothermal growth of CdS-NR arrays on WO_3-NS arrays formed a hierarchical structure. The growth mechanism can be explained by the following chemical reactions:[41, 42]

$$H_2WO_4 + xH_2O_2 \rightarrow WO_3 \cdot xH_2O_2 \cdot H_2O\ (PTA) \quad (1)$$

$$WO_3 \cdot xH_2O_2 \cdot H_2O \rightarrow WO_3 \cdot \frac{1}{3}H_2O(nucleus) + \left(x + \frac{2}{3}\right)H_2O + \frac{x}{2}O_2 \uparrow \quad (2)$$

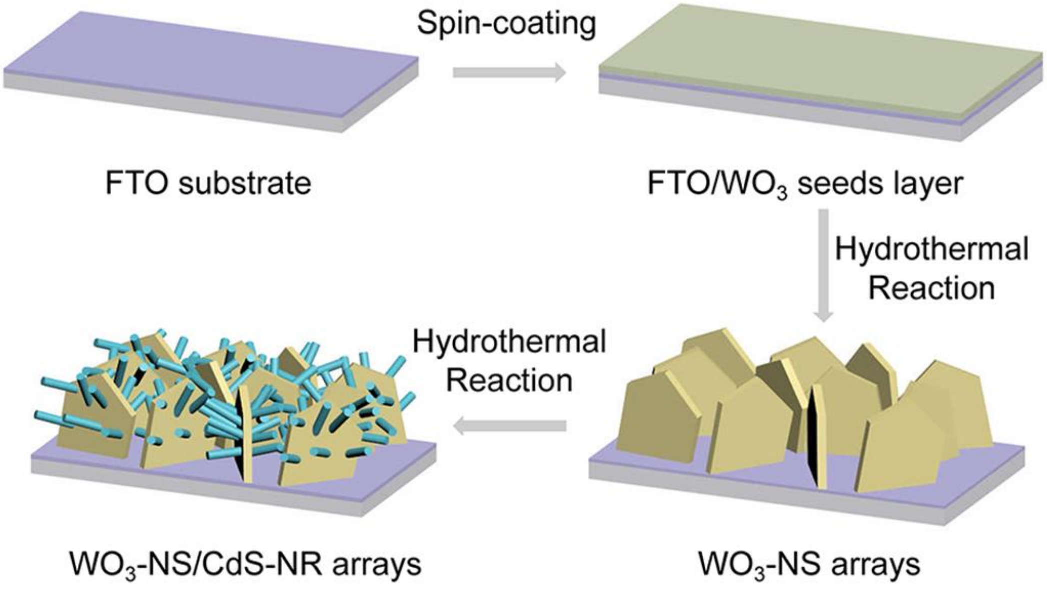

Figure 5.1 Schematic diagram for the fabrication of WO_3-NS/CdS-NR arrays.

$$WO_3 \cdot \frac{1}{3}H_2O(nucleus) \rightarrow WO_3 \cdot \frac{1}{3}H_2O \tag{3}$$

$$Cd(NO_3) + 2(NH_2)_2CS + 4H_2O \rightarrow CdS + H_2S\uparrow + 2HNO_3 + 2CO_2\uparrow + 4NH_3\uparrow \tag{4}$$

The WO_3 nuclei are obtained by the thermal decomposition of peroxopolytungstic acid (PTA), which act as the growth sites and nucleation for the hydrothermal growth of WO_3-NS arrays under the capping agent of oxalic acid and urea. In the second hydrothermal reaction, CdS nuclei form on the WO_3-NS arrays through the decomposition of the $Cd(NO_3)_2 \cdot x(NH_2)_2CS$ complex, which is obtained through the reaction between Cd^{2+} and thiourea. With glutathione-assisted orientation, CdS-NR arrays could be grown on WO_3-NS arrays.

In this hierarchical structure, the random dispersion of CdS-NRs on WO_3-NS also prevents the overlapping of CdS-NRs at the bottom, thus giving rise to a greater contact area with the electrolyte for the more efficient redox reaction and favoring the penetration of incident light to the bottom areas.

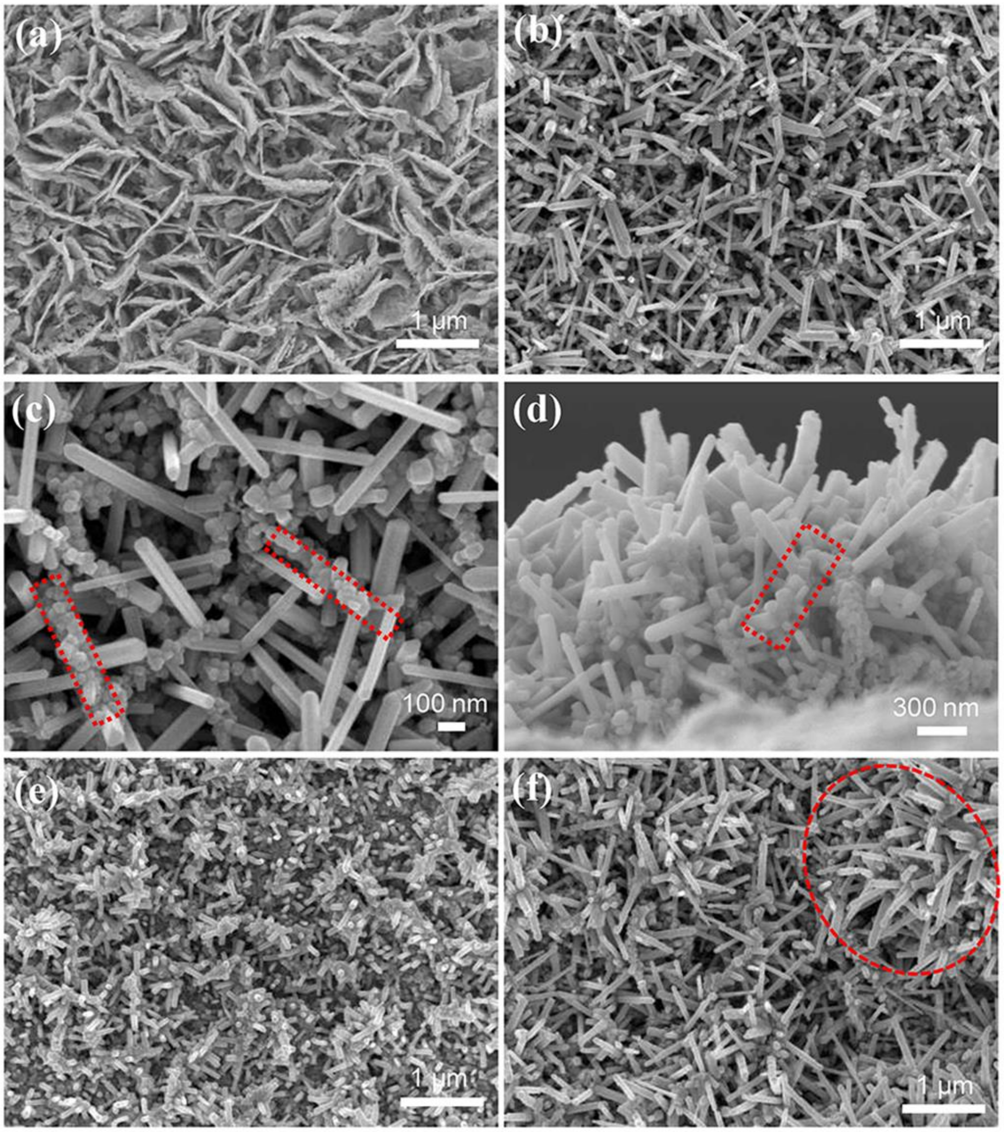

Figure 5.2 Top-view SEM images: (a) WO_3-NS arrays; (b)-(c) WO_3-NS/CdS-NR arrays with 2 h hydrothermal growth of CdS-NRs; (d) Cross-section view SEM image of WO_3-NS/CdS-NR arrays. Top-view SEM images: (e) WO_3-NS/CdS-NR arrays with 1h hydrothermal growth of CdS-NRs; (f) WO_3-NS/CdS-NR arrays with 3 h hydrothermal growth of CdS-NRs.

Figure 5.2(a) shows a typical SEM image of WO_3-NS arrays. The WO_3-NS arrays are observed to be perpendicular to the FTO substrate, leaving enough space between adjacent nanosheets for the secondary growth of other nanostructures. After a 2 h hydrothermal reaction, CdS-NR arrays were grown on the surface of WO_3-NS arrays. As shown in Figures 5.2(b) and 5.2(c), the WO_3-NS arrays are partially covered with short CdS NRs and partially covered with long CdS NRs. The sheet-like structure of WO_3 has been marked with red color. These CdS-NRs have an average length of 400 nm and a diameter of 50 nm. After the growth of CdS-NRs, the surface area of the single WO_3 NS increases by 1.6 times. The increased surface area of WO_3-NS arrays due to the growth of CdS-NR arrays was evaluated by approximating a cylinder geometry.[43, 44]

$$m_{all} = N \times m_{single} = N \times \rho \pi r^2 l \qquad (5)$$

In this equation, m_{all} is the total mass of CdS-NR arrays grown on the surface of WO_3 nanosheet and m_{single} is the mass of single CdS nanorod. N is the total number of CdS nanorods. The mass of the WO_3-NR arrays sample and WO_3-NS/CdS-NR arrays are 3224.7 mg and 3226.7 mg, respectively, so m_{all} is 2 mg. The average length (l) and radius (r) of single CdS nanorod are around 400 nm and 25 nm, respectively. Since the density (ρ) of CdS is 4.826 g cm^{-3}, the mass of singe CdS nanorod is calculated to 7.854 $*10^{-12}$ mg while N is $2.6*10^{11}$. Considering the total surface area of the electrode is 6 cm^2, the number of CdS NRs per cm^2 is $4.3*10^{10}$.

Figure 5.2(c) was selected to evaluate the number of CdS nanorods (n_{cds}) grown on each WO_3 nanosheet. The observed area is $2.89*10^{-8}$ cm^2, hence the number of CdS nanorods in this area is calculated to be $1.24*10^{3}$. The number of WO_3 nanosheets is estimated to be 16 as observed in Figure 5.2(c). Thus, n_{cds} grown on each WO_3 nanosheet is 77. The increased surface area ($S_{increased}$) for each nanosheet can be obtained by multiplying n_{cds} with the surface area of single CdS nanorod:

$$S_{increased} = n_{cds}\, 2\pi r l \qquad (6)$$

Thus, for each WO_3 nanosheet, the surface area increases by approximately $4.83*10^{-12}$ m^3. The surface area of a single WO_3 nanosheet was evaluated by approximating a cuboid geometry. The width of a single WO_3 nanosheet is around 1 μm, the thickness is around 10 nm and the height is around 1.5 μm, hence the surface area of a single WO_3 nanosheet is

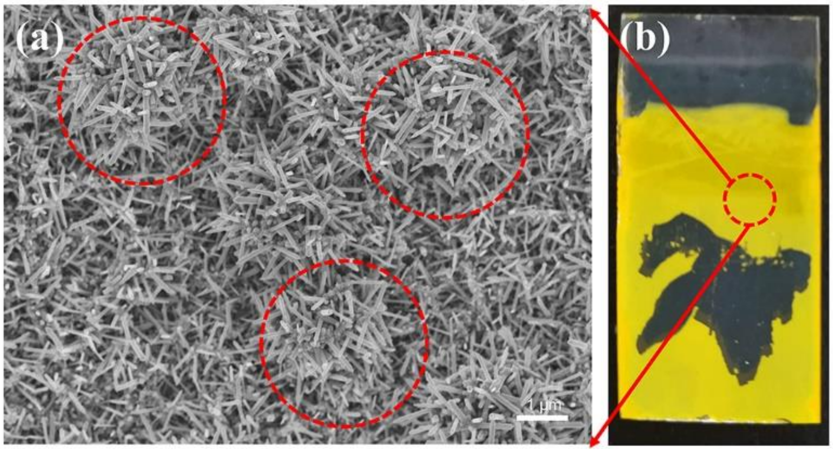

Figure 5.3 (a) Top-view SEM images of WO_3-NS/CdS-NR arrays with 4 h hydrothermal growth of CdS-NRs; (b) Digital image of WO_3-NS/CdS-NR arrays with 4 h hydrothermal growth of CdS-NRs.

approximated as $3*10^{-12}$ m^3. Thus, after the growth of CdS-NR arrays, the surface area of WO_3 nanosheet increases by 1.6 times.

Figure 5.2(c) shows that these CdS-NRs were grown on both sides of single WO_3 NS in random orientations, instead of simply stacking on the surface. In the hydrothermal growth process, CdS seeds were first formed on the surface, followed by the epitaxial growth of CdS-NRs.[23] The direct contact of CdS with WO_3 is beneficial for the transfer of electrons between them. Figure 5.2(d) shows the cross-section SEM image of WO_3-NS/CdS-NR arrays. It can be observed that the sheet-like structure of WO_3 is well maintained with CdS-NRs dispersed on both the upper and bottom surfaces. To investigate the growth process of CdS-NRs on WO_3-NS arrays, the hydrothermal reaction was carried out over different durations. After 1 h of hydrothermal growth, CdS-NRs with smaller lengths were obtained, as shown in Figure 5.2(e). By extending the reaction time to 3 h, both the loading amount and the length of the CdS-NRs increased sharply. In some areas, the density of CdS-NRs is so high that flower-like structures can be observed (marked with red color in Figure 5.2(f)), which fully covered the sheet-like structure of WO_3-NS arrays. The further increment of the reaction time to 4 h led to the peeling of a large area of nanostructures off the FTO substrate after rinsing

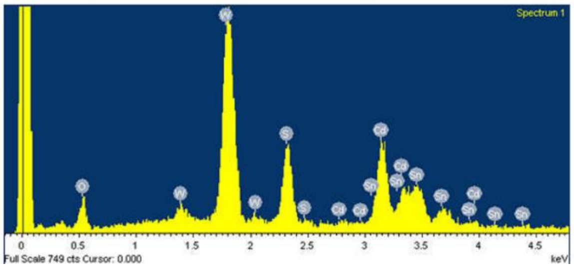

Figure 5.4 EDS of WO_3-NS/CdS-NR arrays.

with DI water. The corresponding optical image is shown in Figure 5.3(b). SEM was utilized to observe the remaining parts of the sample and more flower-like CdS-NRs were obtained on the surface (Figure 5.3(a)). Due to the excessive loading of CdS-NRs, the adhesion between WO_3-NS arrays and FTO substrate is insufficient to support a large amount of CdS-NRs, which may cause the nanostructures to peel off from the FTO substrates. This phenomenon demonstrates that CdS-NRs cannot be continuously loaded by prolonging the hydrothermal growth durations.

Energy-dispersive X-ray Spectroscopy (EDS) was performed to characterize the elemental composition of the as-prepared WO_3-NS/CdS-NR arrays, as shown in Figure 5.4. The EDS results show the presence of elements Sn, O, W, Cd, and S in the samples. The transition from WO_3-NS arrays to WO_3-NS/CdS-NR arrays can also be observed through the color change (Figure 5.5). The bare WO_3-NS arrays are white and translucent. Upon the growth of CdS-NRs, the color of WO_3-NS/CdS-NR arrays became light yellow.

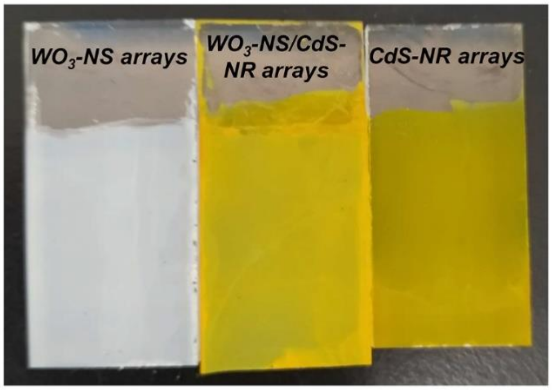

Figure 5.5 Digital images of the WO_3-NS arrays, WO_3-NS/CdS-NR arrays, and CdS-NR arrays.

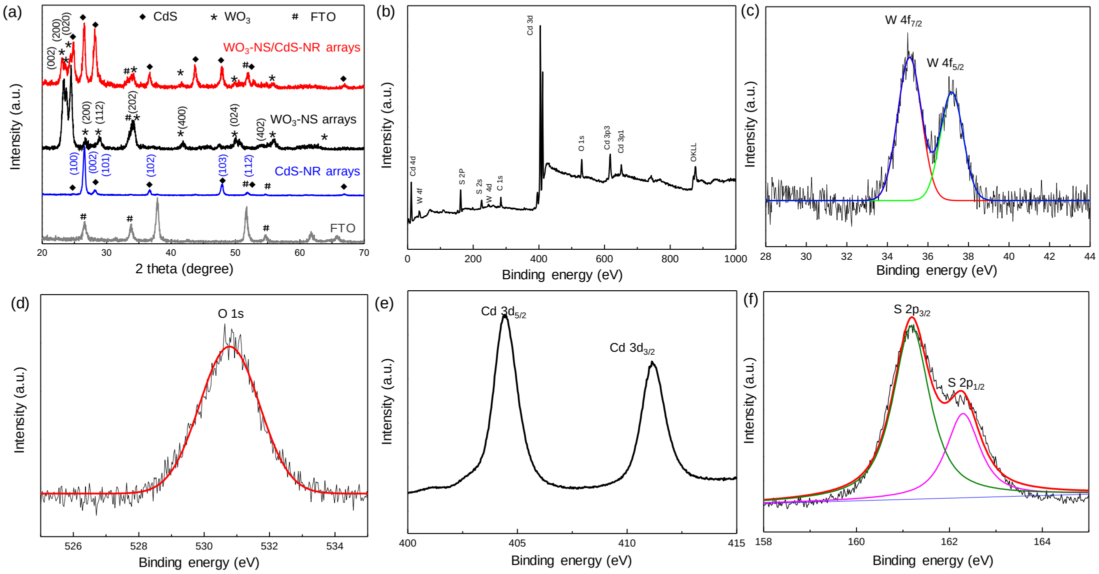

Figure 5.6 (a) XRD characterization of the as-prepared samples; (b) XPS survey spectrum WO_3-NS/CdS-NR arrays; High resolution XPS spectrum of WO_3-NS/CdS-NR arrays: (c) W 4f; (d) O 1s; (e) Cd 3d; (f) S 2p.

Figure 5.6(a) shows the XRD patterns of WO_3-NS/CdS-NR arrays, WO_3-NS arrays, CdS-NR arrays, and FTO substrate. For the WO_3-NS arrays and CdS-NR arrays, except for some peaks of the FTO substrate, all other peaks can be well indexed to the monoclinic phase of WO_3 and the wurtzite phase of CdS.[39, 45] In the case of WO_3-NS/CdS-NR arrays, the peaks corresponding to WO_3, CdS, and FTO can be distinguished, as marked in Figure 5.6(a). XPS spectra were applied to further analyze the composition and surface chemical state of WO_3-NS/CdS-NR arrays. As shown in Figure 5.6(b), the XPS survey spectrum demonstrates that the WO_3-NS/CdS-NR arrays contain Cd, S, W and O elements. Figures 5.6(c)-5.6(f) further show the high-resolution XPS spectrum of WO_3-NS/CdS-NR arrays. The peaks at W $4d_{7/2}$ (34.8 eV), W $3d_{3/2}$ (37.2 eV) and O 1s (531.2 eV) are assigned to W^{6+} and O^{2-} in WO_3, respectively, while the peaks at Cd $3d_{5/2}$ (404.7 eV), Cd $3d_{3/2}$ (411.4 eV) and S $2p_{3/2}$ (162.5 eV), S $2p_{1/2}$ (161.2 eV) can be assigned to Cd^{2+} and S^{2-} in CdS respectively.[21, 36] These observations from both XRD and XPS indicate that the heterostructures with high purity had been successfully synthesized.

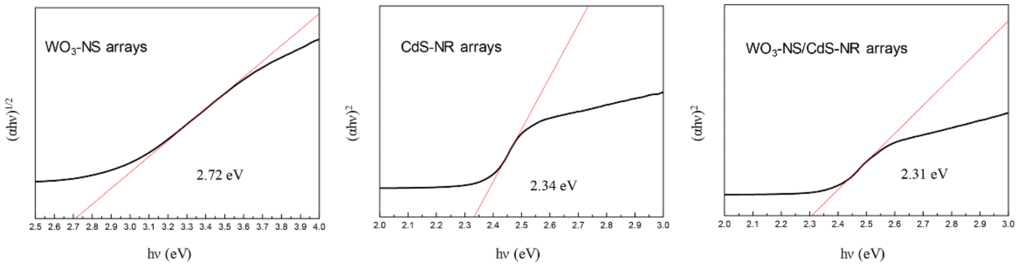

Figure 5.7 The band edge of WO_3-NS arrays, CdS-NR arrays and WO_3-NS/CdS-NR arrays.

The bandgap (Eg) of WO_3-NS arrays, CdS-NR arrays and WO_3-NS/CdS-NR arrays were measured through UV-Vis absorption spectra. As shown in Figure 5.7, the Eg of WO_3-NS arrays, CdS-NR arrays, and WO_3-NS/CdS-NR arrays are 2.72 eV, 2.34 eV and 2.31 eV respectively, as calculated with the following equation:[33]

$$(\alpha h\nu)^n = A(h\nu - Eg) \qquad (7)$$

In this equation, A is a constant, α presents the absorption coefficient and hν is the light energy. WO_3 has an indirect Eg, while CdS has a direct Eg, so the value of n is 1/2 and 2, respectively. Upon the growth of CdS-NR arrays, the bandgap of WO_3-NS/CdS-NR arrays decreased, which can enhance the visible light absorption. This enhanced visible light absorption is essential to the improvement of PEC efficiency of WO_3-NS/CdS-NR arrays as it allows the generation of more electron-hole pairs.

5.3.2 PEC performance

The measuring of linear sweep curves under front-side illumination is used to evaluate the photocurrent of the as-prepared samples with Na_2S/Na_2SO_3 mix solution as an efficient hole scavenger. Due to the fast oxidation kinetics of sulfite, this hole scavenger can prevent the oxidation of CdS and bring about a near 100% of surface charge transfer efficiency. Thus, the sulfite oxidation allows the investigation of charge separation efficiency in the heterostructures. As shown in Figure 5.8(a), the pristine WO_3-NS arrays and CdS-NR

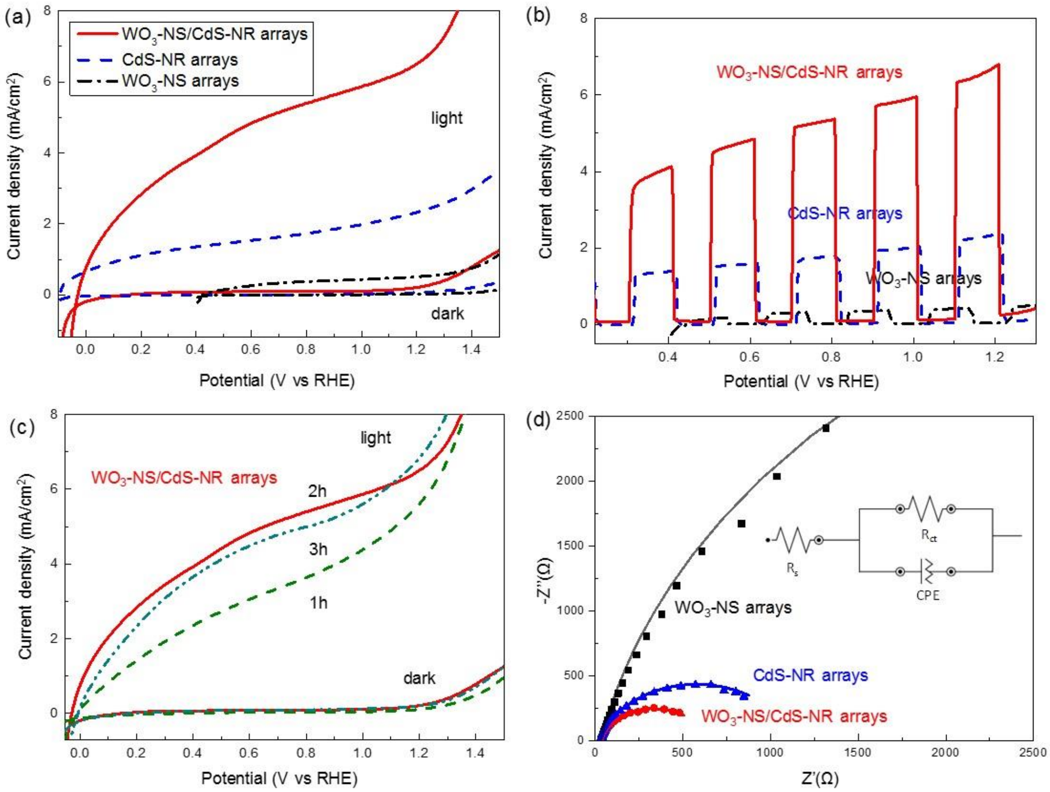

Figure 5.8 (a) Linear sweep curves of WO_3-NS arrays, CdS-NR arrays, and WO_3-NS/CdS-NR arrays; (b) Linear sweep curves of WO_3-NS arrays, CdS-NR arrays, and WO_3-NS/CdS-NR arrays with the light on/off cycles; (c) Linear sweep curves of WO_3-NS/CdS-NR arrays with different hydrothermal growth durations of CdS-NRs; (d) EIS Nyquist plots of WO_3-NS arrays, CdS-NR arrays, and WO_3-NS/CdS-NR arrays. Inset in (d) shows the equivalent circuit.

arrays show photocurrents of 0.45 mA cm^{-2} and 1.85 mA cm^{-2} at 0.8 V versus RHE respectively, which are comparable to previously reported values.[23, 39] After the 2 h hydrothermal growth of CdS-NRs on the surface of WO_3-NS arrays, the resultant WO_3-NS/CdS-NR arrays showed a significant increase in the photocurrent to 5.4 mA cm^{-2} at the same applied voltage, which is approximately 12 times that of WO_3-NS arrays and 3 times that of the CdS-NR arrays. The dark current density of these photoanodes is negligible between 0 V and 1.4 V versus RHE, attesting that these currents were produced by light illumination. It can also be observed that the onset potential of these three photoanodes is different. WO_3-NS arrays electrode has the highest onset potential of 0.45 V versus RHE. After the growth of CdS-NRs, the onset potential of WO_3-NS/CdS-NR arrays electrode decreases to -0.05 V versus RHE due to the formation of a heterojunction between WO_3 and CdS, which is close to that of the pristine CdS-NR arrays (-0.1 V versus RHE). The negative shift of onset potential can be ascribed to the enhanced charge separation efficiency.[46]

Figure 5.8(b) further shows the linear sweep curves of the WO_3-NS/CdS-NR arrays, CdS-NRs arrays, and WO_3-NS arrays electrodes with light ON/OFF cycles. The current density of these photoanodes increases with larger applied voltage and WO_3-NS/CdS-NR arrays show the higher photocurrent density compared to WO_3-NS arrays and CdS-NR arrays, which complies with Figure 5.8(a). Compared with bare WO_3-NS arrays, the improved PEC performance of WO_3-NS/CdS-NR arrays, to some extent, can be ascribed to the extended visible light absorption range resulting from the introduction of CdS-NRs, which was reflected in the UV-Vis absorption characterization. The hierarchical structure of WO_3-NS/CdS-NR arrays also contributes to the improvement of their PEC performance. Compared to pristine CdS-NR arrays, NS/NR hierarchical structure ensures large light scattering within the whole structure and provides a higher surface area of contact with the electrolyte. In addition, the formation of a heterojunction between CdS and WO_3 accelerates the charge separation process, thus leading to the improvement of PEC performance of the hierarchical arrays.

To further investigate the effect of the loading amount as well as the size of CdS-NRs on the PEC performance of the hierarchical arrays, the hydrothermal growth durations of CdS-NRs were varied. Only samples prepared with hydrothermal reactions between 1-3 h were investigated since previous SEM and optical characterizations had shown that longer hydrothermal growth durations of CdS-NRs would destroy the WO_3-NS arrays. The photocurrent of the as-prepared samples is shown in Figure 5.8(c). WO_3-NS/CdS-NR arrays-2h show higher photocurrent density (5.4 mA cm^{-2}) than WO_3-NS/CdS-NR arrays-1h (3.6 mA cm^{-2}) and WO_3-NS/CdS-NR arrays-3h (5.0 mA cm^{-2}) at 0.8 V versus RHE. The change of photocurrent can be ascribed to the variation of loading amount and length of the CdS-NRs, as reflected by SEM characterization. Compared to 1 h hydrothermal growth, the prolonged hydrothermal growth duration to 2 h resulted in the loading of longer

CdS-NRs at a higher quantity. The increment in loading amount and length improve light absorption and provide a larger specific surface area, which in turn increases the photocurrent. However, further increase of hydrothermal growth duration to 3 h caused the photocurrent density to be lowered despite more CdS-NRs grown on the WO_3-NR arrays. This decrease is attributed to the formation of the flower-like structures on the top surface of WO_3-NR arrays which had covered the NR/NS hierarchical structures. Unlike the close contact between CdS-NRs and WO_3-NR in the NR/NS hierarchical structures, the photogenerated electrons in flower-like CdS-NR arrays were not able to transfer as quickly to the WO_3-NRs, which resulted in larger charge recombination rate and thus a lower the photocurrent.

To investigate the charge separation and recombination dynamics of the as-prepared electrodes, EIS measurements were performed under light illumination. The middle frequency (1-10^5 Hz) semicircular diameter in the Nyquist plots can reflect charge transfer at the electrolyte/photoanode interface.[47]. As shown in Figure 5.8(d), WO_3-NS/CdS-NR arrays electrode presents a smaller semicircular diameter in the Nyquist plots than pristine WO_3-NS arrays and CdS-NR arrays, indicating the facilitated interface charge transfer between WO_3-NS and CdS-NR. Furthermore, the equivalent circuit used to fit the EIS data was also provided in Figure 5.8(d). R_s represents the series resistance, such as the resistance of the FTO substrate, while R_{ct} characterizes charge transfer resistance at the electrode/electrolyte interface. The fitting results showed that R_s value of WO_3-NS/CdS-NR arrays (37.6 Ω) was similar to that of WO_3-NS arrays (32.8 Ω) and CdS-NR arrays (31.4 Ω), while the R_{ct} value of WO_3-NS/CdS-NR (593.9 Ω) arrays was much smaller than that of WO_3-NS (9311 Ω) and CdS-NR (1092 Ω). The smallest R_{ct} confirmed the WO_3-NS/CdS-NR arrays could facilitate charge separation and transportation.

The Incident-photon-to-current-conversion efficiency (IPCE) of the as-prepared photoanodes were measured at 0.8 V versus RHE, which is defined by the following Equation:[8]

$$IPCE = (1024I)/(\lambda \, \mathrm{J}_{\mathrm{light}}) \qquad (8)$$

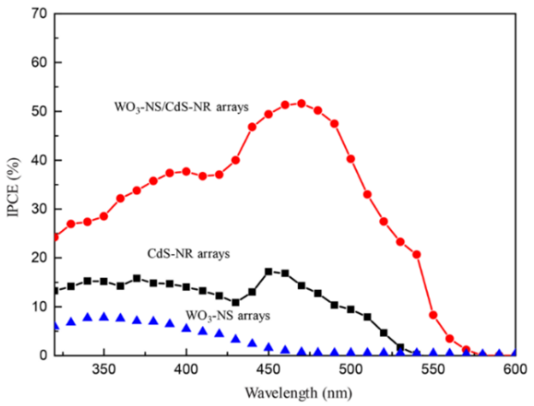

Figure 5.9 IPCE of WO_3-NS arrays, CdS-NR arrays and WO_3-NS/CdS-NR arrays.

Where λ is the wavelength of the incident light, I is the corresponding photocurrent density and J_{light} is the incident light power density. As shown in Figure 5.9, WO_3-NS/CdS-NR arrays have higher IPCE maximum (55%) in the wavelength between 300-550 nm compared to that of CdS-NR arrays (20%) and WO_3-NS arrays (10%), which could be ascribed to the enhanced charge separation efficiency due to the formation of the heterojunctions.

The formation of a heterojunction and the PEC water splitting process in the WO_3-NS/CdS-NR arrays are schematically illustrated in Figure 5.10. Due to the well-matched band edge position, a type-II heterojunction forms upon the contact of CdS with WO_3, as shown in Figure 5.10(a).[35, 48] Electrons generated in the conduction band (CB) of CdS transfer to the lower CB of WO_3, while holes transfer from lower valence band (VB) of WO_3 to higher VB of CdS for the sulfite oxidation. In this way, the recombination rate of photogenerated carriers is depressed. In addition to the formation of type-II heterojunction, the high conductivity of WO_3 ensures effective charge collection and thus lowers the bulk charge recombination rate. The detailed charge separation process in the PEC device is shown in Figure 5.10(b). In pristine CdS-NR arrays, the photogenerated electrons can only transfer to the FTO substrate through the less conductive CdS-NRs before transferring to the FTO substrate. Hence there are more chances for charge recombination. When CdS-NRs are grown on the highly conductive WO_3-NS, electrons generated in the CdS can be transferred to FTO

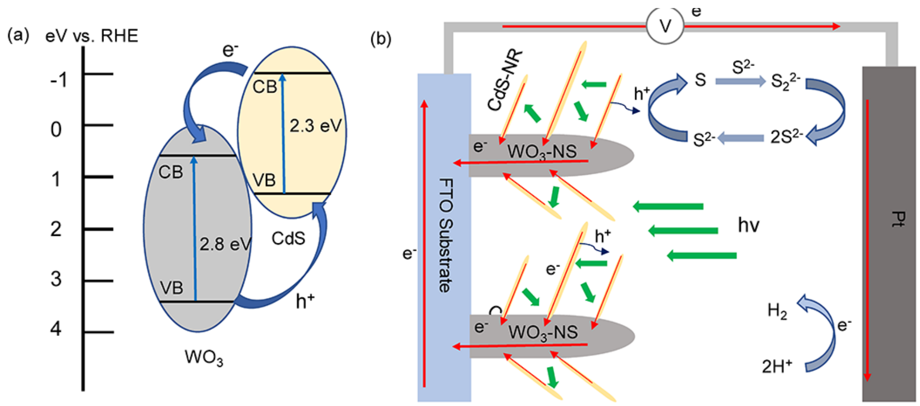

Figure 5.10 (a) Schematic of the formation of a type-II heterojunction between CdS and WO_3; (b) Schematic of the PEC water splitting process in WO_3-NS/CdS-NR arrays photoanode.

Table 5.1 Comparison of PEC performance of reported WO_3/CdS based nanostructures.

WO_3/CdS based photoanodes	Electrolyte	Photocurrent density [$mAcm^{-2}$] a)	Band gap (eV)	Remarks
WO_3-NS/CdS-NR arrays	0.25 M Na_2S + 0.35 M Na_2SO_3	4.9	2.31	This work
WO_3-nanowires/CdS-film	0.1 M Na_2S	1.4	2.32	[33]
Platelike WO_3/TiO_2/CdS-QDs	0.25 M Na_2S + 0.35 M Na_2SO_3	0.95	2.34	[34]
$WO_3/CdWO_4$/CdS-QDs	0.25 M Na_2S + 0.35 M Na_2SO_3	2.5	2.25	[35]
WO_3-NSs/CdS-QDs	0.25 M Na_2S + 0.35 M Na_2SO_3	1.7	-	[36]

a) The photocurrent density was collected at 0.6 V vs. RHE under AM 1.5 illumination (100 mW cm^{-2}).

substrate with the assistant of conductive WO_3 skeleton, and finally, reach to the Pt electrode for the generation of hydrogen. These factors resulted in improved PEC performance of WO_3-NS/CdS-NR arrays compared to that of WO_3-NS arrays and CdS-NR arrays and showed a higher photocurrent compared to other reported WO_3/CdS heterostructures, as shown in Table 5.1.

It was reported that amorphous TiO_2 films by ALD could mitigate photo corrosion of CdS-based photoanodes as well as act as a passivation layer to suppress surface charge recombination.[49] Thus, an ultrathin layer of amorphous TiO_2 films was deposited on WO_3-NS/CdS-NR arrays to increase the photo-stability. Representative TEM images of WO_3-NS/CdS-NR arrays/TiO_2 are shown in Figure 5.11(a) and Figure 5.11(b). As shown in Figure 5.11(a), the morphologies of CdS-NR and WO_3-NS can be clearly distinguished. The inset of Figure 5.11(b) is the HRTEM image of WO_3 NS. The d-spacing of 0.365 nm can be ascribed to (200) plan of WO_3. Figure 5.11(b) shows a single CdS NR coated with a thin TiO_2 layer. The boundary between lattice fringes of CdS and amorphous TiO_2 was marked with a red dash line. The thickness of the TiO_2 film is around 2 nm. The inset image shows clear lattice fringes with a d-spacing of 0.34 nm, which corresponds to (002) plan of CdS. As shown in Figure 5.11(c), the photocurrent of WO_3-NS/CdS-NR arrays/TiO_2-10 cycles is comparable to that of the uncoated WO_3-NS/CdS-NR arrays. With the deposition of more TiO_2, WO_3-NS/CdS-NR arrays/TiO_2-20 cycles showed a slightly higher photocurrent than that of pure WO_3-NS/CdS-NR arrays at lower applied potentials. However, the further deposition of TiO_2 causes the decrease of the photocurrent of WO_3-NS/CdS-NR arrays/TiO_2-30 cycles and WO_3-NS/CdS-NR arrays/TiO_2-40 cycles. In the ALD process, the thickness of TiO_2 films increases linearly with the number of ALD cycles.[50] The amorphous TiO_2 acts as a protective layer as well as a passivation layer. When 10 and 20 ALD cycles were performed, the amorphous TiO_2 layer produced is so thin that some pinholes exist, providing channels for holes transfer from CdS to the electrolyte. In addition, amorphous TiO_2 can passivate the surface state on the CdS-NR arrays, thus reducing charge recombination probability. At this point, the photocurrent increases with the increase of ALD cycles. However, the further increase of ALD cycles brings about a thicker TiO_2 layer on the surface of CdS. The thick TiO_2 layer takes on the role of a tunneling barrier rather than a passivation layer, which prevents the transfer of holes from the CdS to the electrolyte.[51] Thus, the photocurrent decreases when 30 and 40 ALD cycles were

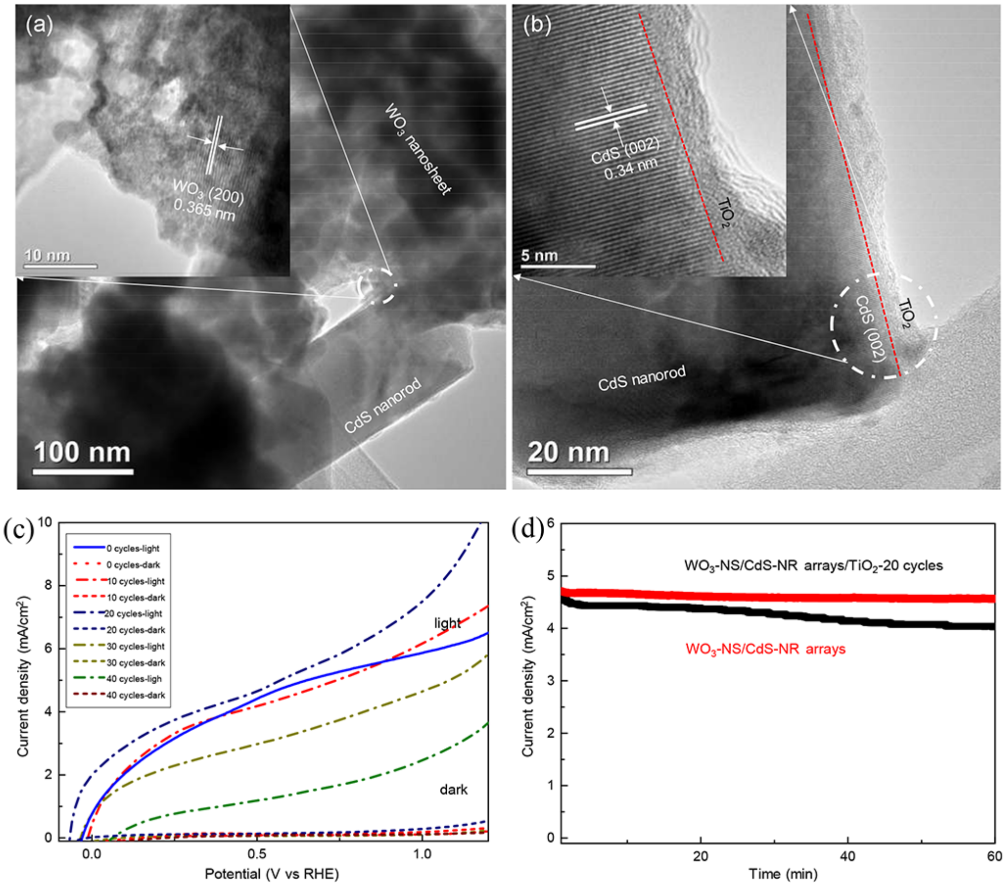

Figure 5.11 (a) TEM image of WO_3-NS/CdS-NR arrays/TiO_2-20 cycles. The inset is the HRTEM image of WO_3-NS; (b) TEM image of single CdS-NR coated with 20 ALD cycles of TiO_2. The inset is the HRTEM image of CdS-NR; (c) Linear sweep curves of WO_3-NS/CdS-NR arrays with different ALD cycles of TiO_2; (d) Photostability test of WO_3-NS/CdS-NR arrays and WO_3-NS/CdS-NR arrays/TiO_2-20 cycles.

performed. Figure 5.11(d) shows the photostability test results of WO_3-NS/CdS-NR arrays/TiO_2-20 cycles and WO_3-NS/CdS-NR arrays. After 1 hour of light illumination, the photocurrent density of WO_3-NS/CdS-NR arrays/TiO_2-20 cycles decreased from 4.7 mA cm^{-2} to 4.6 mA cm^{-2} at 0.5 V versus RHE, while the photocurrent density of pure WO_3-NS/CdS-NR arrays dropped from 4.5 mA cm^{-2} to 4 mA cm^{-2}. After the photostability test, SEM and XRD results show that there is no obvious change in the morphology and phase of WO_3-NS/CdS-NR arrays/TiO_2-20 cycles, as shown in Figure 5.12. The enhanced photostability of WO_3-NS/CdS-NR arrays/TiO_2-20 cycles could be ascribed to the

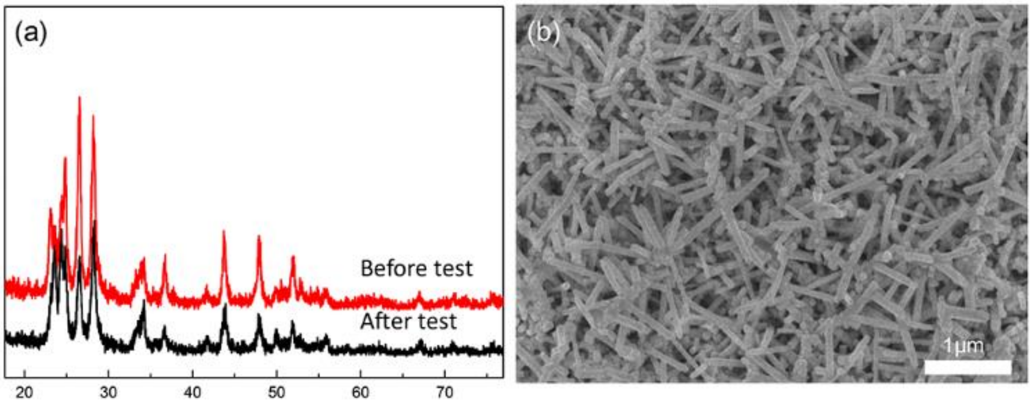

Figure 5.12 XRD and SEM characterizations of WO_3-NS/CdS-NR arrays/TiO_2 after stability test.

deposition of amorphous TiO_2 layer, which prevents direct contact between CdS and the electrolyte. In addition, the TiO_2 layer can capture and store holes generated by CdS and thus reduce the photocorrosion.[52]

5.4 Conclusion

In summary, a type-II WO_3/CdS heterojunction with a hierarchical structure has been presented as a photoanode for PEC water splitting. Through the optimization of hydrothermal growth of CdS-NRs, the as-prepared WO_3-NS/CdS-NR arrays demonstrated enhanced PEC performance compared to pristine WO_3-NR arrays and CdS-NR arrays. This improvement can be ascribed to the broader light absorption spectrum, the depressed charge recombination rate due to the heterojunction between CdS and WO_3, as well as the high charge collection ability of WO_3. The hierarchical structure also enables better light scattering ability and provides a higher specific surface area to the as-prepared photoanode. In addition, an ultrathin layer of the amorphous TiO_2 layer has been applied as a protection layer to enhance the photostability of WO_3-NS/CdS-NR arrays. This work indicates that the construction of a hierarchical nanostructure with the combination of a highly conductive skeleton, favorable heterojunction, and efficient light absorption is an effective route for improving the PEC performance of a photoanode.

References

[1] H. Kaneko, T. Minegishi, K. Domen, *Chem.-Eur. J*. **2018**, *24*, 5697-5706.

[2] K.N. Dinh, P. Zheng, Z. Dai, Y. Zhang, R. Dangol, Y. Zheng, B. Li, Y. Zong, Q. Yan, *Small* **2018**, *14*, 1703257.

[3] H. Hou, H. Liu, F. Gao, M. Shang, L. Wang, L. Xu, W.-Y. Wong, W. Yang, *Electrochim. Acta*, **2018**, *283*, 497-508.

[4] G.V. Govindaraju, G.P. Wheeler, D. Lee, K.-S. Choi, *Chem. Mater*. **2016**, *29*, 355-370.

[5] T. Jin, P. Diao, Q. Wu, D. Xu, D. Hu, Y. Xie, M. Zhang, *Appli. Catal. B: Environ.* **2014**, *148*, 304-310.

[6] P. Kuang, L. Zhang, B. Cheng, J. Yu, *Appli. Catal. B: Environ*. **2017**, *218*, 570-580.

[7] Z. Zhang, L. Zhang, B. Chen, M. Baek, K. Yong, *ACS Sustain. Chem. Eng*. **2018**, *6*, 13462-13472.

[8] Z. Wang, X. Li, H. Ling, C.K. Tan, L.P. Yeo, A.C. Grimsdale, A.I.Y. Tok, *Small* **2018**, *14*, 1800395.

[9] B. Chen, Z. Zhang, M. Baek, S. Kim, W. Kim, K. Yong, *Appl. Catal. B: Environ*. **2018**, *237*, 763-771.

[10] A. Mezzetti, M. Balandeh, J. Luo, S. Bellani, A. Tacca, G. Divitini, C. Cheng, C. Ducati, L. Meda, H. Fan, *Nanotechnology* **2018**, *29*, 335404.

[11] L. Zhou, C. Zhao, B. Giri, P. Allen, X. Xu, H. Joshi, Y. Fan, L.V. Titova, P.M. Rao, *Nano Lett*. **2016**, *16*, 3463-3474.

[12] X. Zhao, J. Hu, B. Wu, A. Banerjee, S. Chakraborty, J. Feng, Z. Zhao, S. Chen, R. Ahuja, T.C. Sum, *J. Mater. Chem. A* **2018**, *6*, 16965-16974.

[13] F. Cao, W. Tian, L. Li, *J. Mater. Sci. Technol.* **2018**, *34*, 899-904.

[14] C. Liu, F. Meng, L. Zhang, D. Zhang, S. Wei, K. Qi, J. Fan, H. Zhang, X. Cui, *Appl. Surf. Sci*. **2019**, *469*, 276-282.

[15] R.-B. Wei, P.-Y. Kuang, H. Cheng, Y.-B. Chen, J.-Y. Long, M.-Y. Zhang, Z.-Q. Liu, *ACS Sustain. Chem. Eng*. **2017**, *5*, 4249-4257.

[16] W. Kim, D. Monllor-Satoca, W.-S. Chae, M.A. Mahadik, J.S. Jang, *Appl. Surf. Sci*. **2019**, *463*, 339-347.

[17] Z. Wang, X. Li, C.K. Tan, C. Qian, A.C. Grimsdale, A.I.Y. Tok, *Appl. Surf. Sci*. **2019**,

470, 800-806.

[18] F. Zhan, W. Liu, H. Li, Y. Yang, M. Wang, *Appl. Surf. Sci*. **2018**, *455*, 476-483.

[19] T. Wang, Y. Chai, D. Ma, W. Chen, W. Zheng, S. Huang, *Nano Research* **2017**, *10*, 2699-2711.

[20] Z. Han, M. Wang, X. Chen, S. Shen, P*hys. Chem. Chem. Phys*. **2016**, *18*, 11460-11466.

[21] L. Wang, W. Wang, Y. Chen, L. Yao, X. Zhao, H. Shi, M. Cao, Y. Liang, *ACS Appl. Mater. Interfaces* **2018**, *10*, 11652-11662.

[22] Y. Huang, Y. Xu, J. Zhang, X. Yin, Y. Guo, B. Zhang, *J. Mater. Chem. A* **2015**, *3*, 19507-19516.

[23] W. Wang, C. Jin, L. Qi, *Small* **2018**, *14,* 1801352.

[24] J.-P. Song, P.-F. Yin, J. Mao, S.-Z. Qiao, X.-W. Du, *Nanoscale* **2017**, *9*, 6296-6301.

[25] Y. Fu, F. Cao, F. Wu, Z. Diao, J. Chen, S. Shen, L. Li, *Adv. Funct. Mater*. **2018**, *16*, 1706785.

[26] S. Hu, M.R. Shaner, J.A. Beardslee, M. Lichterman, B.S. Brunschwig, N.S. Lewis, *Science* **2014**, *344*, 1005-1009.

[27] Z. Ma, K. Song, L. Wang, F. Gao, B. Tang, H. Hou, W. Yang, *ACS Appl. Mater. Interfaces* **2018**, *11,* 889-897.

[28] Y. Li, L. Zhang, R. Liu, Z. Cao, X. Sun, X. Liu, J. Luo, *ChemCatChem* **2016**, *8*, 2765-2770.

[29] Y. Wang, W. Tian, L. Chen, F. Cao, J. Guo, L. Li, *ACS Appl. Mater. Interfaces* **2017**, *9*, 40235-40243.

[30] Q. Zeng, Y. Gao, L. Lyu, S. Chang, C. Hu, *Nanoscale* **2018**, *10*, 13393-13401.

[31] J. Choi, T. Song, J. Kwon, S. Lee, H. Han, N. Roy, C. Terashima, A. Fujishima, U. Paik, S. Pitchaimuthu, *Appl. Surf. Sci*. **2018**, *447*, 331-337.

[32] J. Fu, Q. Xu, J. Low, C. Jiang, J. Yu, *Appl. Catal. B: Environ*. **2019**, *243,* 556-565.

[33] H. Li, Y. Zhou, L. Chen, W. Luo, Q. Xu, X. Wang, M. Xiao, Z. Zou, *Nanoscale* **2013**, *5*, 11933-11939.

[34] C. Liu, Y. Li, W. Li, J. Zhu, J. Li, Q. Chen, Y. Yang, *Mater. Lett*. **2014**, *120*, 170-173.

[35] F. Zhan, J. Li, W. Li, Y. Yang, W. Liu, Y. Li, *J. Power Sources* **2016**, *325*, 591-597.

[36] Y. Liu, Y. Cui, F. Huang, X. Yang, *RSC Adv*. **2016**, *6,* 16668-16672.

[37] Y. Liu, Z. Kang, H. Si, P. Li, S. Cao, S. Liu, Y. Li, S. Zhang, Z. Zhang, Q. Liao, L.

Wang, Y. Zhang, *Nano Energy* **2017**, *35*, 189-198.

[38] S. Bai, X. Yang, C. Liu, X. Xiang, R. Luo, J. He, A. Chen, *ACS Sustain. Chem. Eng*. **2018**, *6*, 12906-12913.

[39] W. Shi, X. Zhang, J. Brillet, D. Huang, M. Li, M. Wang, Y. Shen, *Carbon* **2016**, *105*, 387-393.

[40] X. Li, M. Puttaswamy, Z. Wang, C. Kei Tan, A.C. Grimsdale, N.P. Kherani, A.I.Y. Tok, *Appl. Surf. Sci*. **2017**, *422*, 536-543.

[41] Z. Jiao, X. Wang, J. Wang, L. Ke, H.V. Demir, T.W. Koh, X.W. Sun, *Chem. Commun*. **2012**, *48*, 365-367.

[42] Y. Liu, Y.-X. Yu, W.-D. Zhang, *J. Alloys Compd*. **2013**, *569*, 102-110.

[43] T.D. Nguyen, G.G. Scherer, Z.J. Xu, *Electrocatalysis* **2016**, *7*, 420-427.

[44] Y. Lee, J. Suntivich, K.J. May, E.E. Perry, Y. Shao-Horn, *J. Phys. Chem. Lett*. **2012**, *3*, 399-404.

[45] X.-X. Yu, H. Yin, H.-X. Li, H. Zhao, C. Li, M.-Q. Zhu, *J. Mater. Chem. C* **2018**, *6*, 630-636.

[46] S.J. Hong, S. Lee, J.S. Jang, J.S. Lee, *Energy Environ. Sci*. **2011**, *4*, 1781-1787.

[47] F. Ning, M. Shao, S. Xu, Y. Fu, R. Zhang, M. Wei, D.G. Evans, X. Duan, *Energy Environ. Sci*. **2016**, *9*, 2633-2643.

[48] Y. Li, Z. Liu, J. Zhang, Z. Guo, Y. Xin, and L. Zhao, *J. Alloy. Compds.* **2019**, *790*, 493-501.

[49] S.K. Karuturi, R. Yew, P.R. Narangari, J. Wong-Leung, L. Li, K. Vora, H.H. Tan, C. Jagadish, *Nano Futures* **2018**, *2*, 015004.

[50] J.P. Lee, Y.J. Jang, M.M. Sung, *Adv. Funct. Mater*. **2003**, *13*, 873-876.

[51] Z. Xie, X. Liu, W. Wang, X. Wang, C. Liu, Q. Xie, Z. Li, Z. Zhang, *Nano Energy* **2015**, *11*, 400-408.

[52] R. Wang, L. Wang, Y. Zhou, Z. Zou, *Appl. Catal. B: Environ*. **2019**, *255*, 117738.

Chapter 6*

3D FTO IOs/SnO_2 NCs/TiO_2 Composite Inverse Opal Photoanode for Efficient Photoelectrochemical Water Splitting

This chapter reported a 3D fluorine-doped SnO_2 inverse opal (FTO IOs)/SnO_2 nanocrystals (NCs)/TiO_2 structure is designed and fabricated as a new "host & guest" type of composite photoanode for efficient photoelectrochemical (PEC) water splitting. In this novel photoanode design, the highly conductive and porous FTO IOs/SnO_2 NCs acts as the "host" skeleton, which provides direct pathways for faster electron transport, while the conformally coated TiO_2 layer acts as the "guest" absorber layer. The unique composite IO structure is fabricated through self-assembly of colloidal spheres template, a hydrothermal method and atomic layer deposition (ALD). Owing to its large surface area and efficient charge collection, the FTO IOs/SnO_2 NCs/TiO_2 composite photoanode shows excellent photocatalytic properties for PEC water splitting. With optimized dimensions of the SnO_2 NCs and the thickness of the ALD TiO_2 absorber layers, the 3D FTO IOs/SnO_2 NCs/TiO_2 photoanode yields a photocurrent density of 1.0 mA cm^{-2} at 1.23 V vs. RHE under AM 1.5 illumination, which is 4 times higher than that of the FTO IOs/TiO_2 reference photoanode.

---

*This section is published substantially as Z. Wang, et al. *Small* **2018**, *14*,1800395.

6.1 Introduction

The ability to directly convert solar energy into hydrogen has made photoelectrochemical (PEC) water splitting as one of the most promising techniques to harvest unlimited solar energy.[1, 2] A key challenge for PEC applications is the fabrication of high-performance nanostructured photoelectrodes, which are characterized by high carrier mobility, wide light absorption range, high stability and environmental benignity.[3-5] Much research has been done to enhance the solar energy conversion efficiency of the photoelectrodes.[6, 7] TiO_2 was investigated as a photoanode since 1972 owing to the favorable band edge positions, high photochemical stability, nontoxicity, and low cost.[8-10] However, the PEC performance of TiO_2 is restricted by its short hole diffusion length, low electron mobility, and the wide bandgap.[11-13] In the past decades, some targeted strategies, such as elemental doping, structural design, and surface modification, were proposed to increase the photocurrent of TiO_2.[14-16] Recently, constructing composite semiconductor nanostructures with the use of two or more materials were reported to enhance light absorption and the charge separation and hence enhance the overall PEC efficiency.[17-21] In such composite electrode designs, a conductive skeleton with a high specific area acts as the host, which is then further coated with a photoactive guest material. Due to the transparent conductive oxide nature of fluorine-doped tin oxide (FTO) or antimony doped tin oxide (ATO), it is considered as an ideal host material for this purpose.[22-24] For instance, a thin TiO_2 layer coated on FTO and ATO nanoparticle film photoanodes were reported to have excellent PEC performance.[25, 26] In addition, the design of a nanostructured electrode is essential to the PEC performance. 3D inverse opals (IOs) have presented extraordinary high PEC efficiency.[27-30] The light scattering inside the continuous and periodic void structure of the 3D IOs enhances light absorption while the large specific surface area of the structure allows the loading of conductive films and light absorber materials.[31, 32] The specific surface area of IOs can be further increased by loading secondary nanostructures, for example, ZnO nanorods (NRs) grown on TiO_2 IOs were reported to increase the surface area of the entire photoanode.[33] In the meantime, the conformal coating of such a porous host skeleton with a uniform and continuous absorber layer is equally important to the PEC performance of the entire composite photoelectrode, which still remains a challenge currently. Atomic layer deposition (ALD) with a self-limiting surface reaction mechanism has demonstrated its effectiveness in depositing conformal thin films over highly porous nanostructures.[34-36] In particular, a stop-flow ALD process was utilized to deposit MoS_2 thin films on such highly porous 3D IOs in our previous study.[37]

Herein, 3D FTO IOs/SnO_2 nanocrystals (NCs)/TiO_2 thin film, denoted as FTO IOs/SnO_2 NCs/TiO_2, were fabricated for PEC water splitting. In this composite IOs, the highly porous and conductive FTO IOs/SnO_2 NCs acted as the host scaffold for deposition of the photoactive TiO_2 layer, providing direct pathways for electron transport. The void spaces of the FTO IOs are beneficial to the secondary growth of SnO_2 NCs, which further increases the surface area of the structure. The light scattering inside the continuous and periodic void structure provides additional benefits for light harvesting. Moreover, a stop-flow ALD process ensures that the photoactive TiO_2 layer coated on the highly porous FTO IOs/SnO_2 NCs is continuous and has excellent conformality. The as-fabricated FTO IOs/SnO_2 NCs/TiO_2 presented a maximum photocurrent density of 1.0 mA cm^{-2} at 1.23 V vs. RHE, which is 4 times to that of the reference FTO IOs/TiO_2 photoanode (0.25 mA cm^{-2}).

6.2. Experimental Section

6.2.1 Materials

All the solid chemicals were purchased from Sigma-Aldrich without further treatment, including tin tetrachloride ($SnCl_4{\cdot}5H_2O$), ammonium fluoride (NH_4F), antimony chloride ($SbCl_3$) and absolute ethanol. Polystyrene (PS) microspheres were obtained from Duke Corporation.

6.2.2 Preparation of FTO IOs

The FTO IOs structure was prepared by using a PS opals as sacrificial templates. Firstly, FTO coated glass substrates were sequentially cleaned with acetone, methanol, ethanol and

DI water. Cleaned FTO substrates were then immersed into a PS solution and kept at 50 °C, for 72 hours to initiate the self-assembly of PS opals. Secondly, PS opal templates were immersed in methanol for 10 minutes and then quickly transferred to a prepared FTO precursor solution, which were contained in a suction flask connected to a vacuum pump. The FTO precursors were prepared by using 2.8 g tin tetrachloride ($SnCl_4$,), 50 mg ammonium fluoride (NH_4F,) and 40 ml absolute-ethanol. After evacuating of the suction flask for 30 mins, the PS opal templates were taken out and dried in air. In the last step, the samples were annealed in air at 550 °C for 2 h, which can remove the PS opals and crystallize the FTO simultaneously.

6.2.3 Fabrication of the FTO IOs/SnO_2 NCs

The FTO glass substrates covered with FTO IOs were put into an autoclave (Parr, 125 mL) in precursor solution prepared with ethanol (25 mL), DI water (25 mL), HCl (1.3 ml or 2ml), and $SnCl_4$ (30-60 mg). Then, the autoclave was transferred to an oven and kept at 200 °C for hydrothermal reaction for 12 h. Afterward, the samples were taken out from the autoclave, dried in ambient air, and annealed at 500 °C for 2h.

6.2.4 Fabrication of FTO IOs/SnO_2 NCs/TiO_2

A thin layer of TiO_2 films was coated on FTO IOs/SnO_2 NCs by ALD, which was carried out on a homebuilt ALD system with stop-flow mode. The reaction chamber was maintained at 80 °C. $TiCl_4$ and water were used as the Ti and O precursors, respectively. Typically, a pressure stop-flow ALD process includes the pulsing of precursor (200 ms), increase the chamber pressure by filling of N_2 to the 6 mbar, and maintained the pressure for reaction (5 s), and purging time (10 s) for each precursor. For comparison, a bare TiO_2 IO structure was prepared by a stop-flow ALD process with 600 cycles. Also, FTO IOs/SnO_2 NCs/TiO_2 was prepared using a continuous ALD process with the same number of cycles for comparison. After ALD of TiO_2, the samples were annealed at 500 °C for 1 hour in the air.

6.2.5 Material Characterization

Field-emission scanning electron microscope (SEM), JEOL, JSM 7600F, and Transmission electron microscopy (TEM) and high-resolution transmission electron microscopy (HRTEM), JEOL, JEM-2100F, were used to investigate the morphology of the as-prepared samples. X-ray diffraction pattern (XRD) patterns were obtained with Bruker D8 X-ray diffractometer. Varian, Cary 5000 was used to obtain UV-Vis diffuse reflectance spectra. Raman spectra were acquired on a Renishaw system. The excitation wavelength is 532 nm.

6.2.6 PEC Measurement

The PEC performance of the as-prepared samples was measured under AM 1.5G simulated sunlight illumination. The photocurrent was collected on an Autolab 270 workstation with a three-electrode electrochemical system. The as-prepared photoanodes were used as the working electrode, Ag/AgCl (3M KCl) were used as the reference electrode, and the platinum mesh was used as the counter electrode. The electrolyte was 1 M NaOH solution. The electrochemical impedance spectroscopy (EIS) data were collected on the same electrochemical system with a frequency range from 10^{-1} to 10^{5} Hz under a 10 mV amplitude. Incident-photon-to-current-conversion efficiency (IPCE) test was performed with a xenon light source (MAX-302, Asahi Spectra Co. Ltd.) and a monochromator (CMS-100, Asahi Spectra Co. Ltd.) at a potential of 1.23 V vs. RHE.

6.3 Results and discussion

6.3.1 Fabrication and Characterization

The fabrication process of FTO IOs/SnO_2 NCs/TiO_2 is shown in Figure 6.1. Firstly, PS microspheres were self-assembled on the FTO glass substrate to form PS opals. Secondly, a modified dip-coating method was utilized to fill the precursors into the voids of the PS opal templates. After post-annealing, the FTO IOs structure can be formed. During the dip-

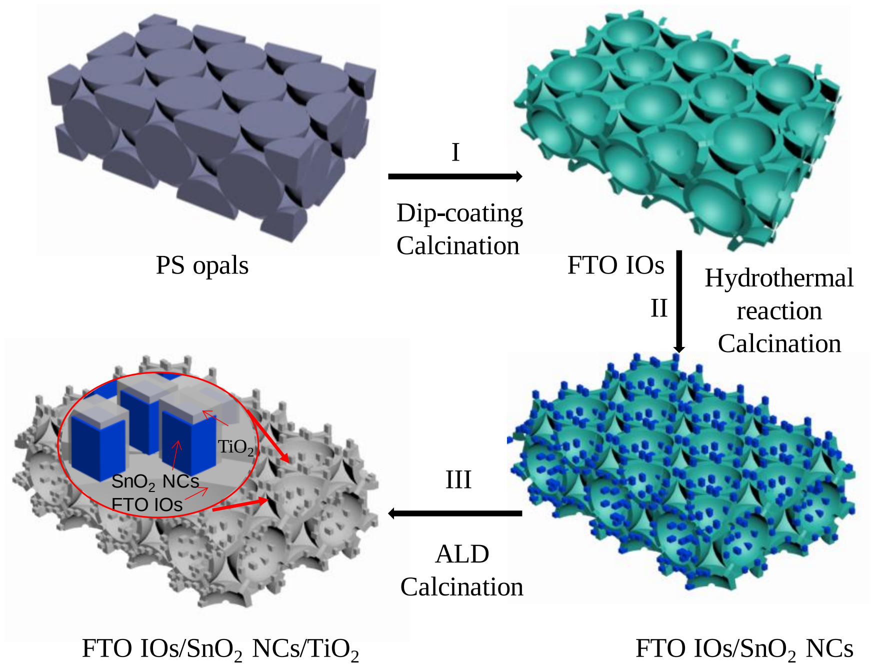

Figure 6.1 Schematic diagram for the fabrication of the FTO IOs/SnO$_2$ NCs/TiO$_2$.

coating process, the PS opal templates were immersed into methanol prior to immersing in the FTO precursors. Under evacuation, methanol will be removed first because of its low boiling point and thus form a negative pressure, favoring the impregnation of precursors into the voids throughout the PS opal templates.[38] After calcination, crystallized FTO IOs were obtained. In an electrochemical system, with many reactions between the electrode and electrolyte, an electrode with a larger contact area would give rise to more active sites, and thus enhance the overall performance of the entire system. For the FTO IOs, there is still enough space for the growth of secondary nanostructure to further increase the surface area of the entire host structure. For this purpose, growing SnO$_2$ NCs on the FTO IOs is a good choice, because it can increase surface area. Thus, SnO$_2$ NCs were grown on the FTO IOs by a simple hydrothermal reaction in the third step. After a second calcination process, the FTO IOs/SnO$_2$ NCs conductive skeleton was successfully fabricated. Finally, a conformal and continuous TiO$_2$ layer was deposited on FTO IOs/SnO$_2$ NCs by a stop-flow ALD process to form an FTO IOs/SnO$_2$ NCs/TiO$_2$. In the stop-flow ALD process, the precursors are kept at proper base pressure for 5s to enhance the precursor diffusion and adsorption. The unique role of the stop-flow ALD process over the highly porous IOs had been demonstrated in our previous report.[37]

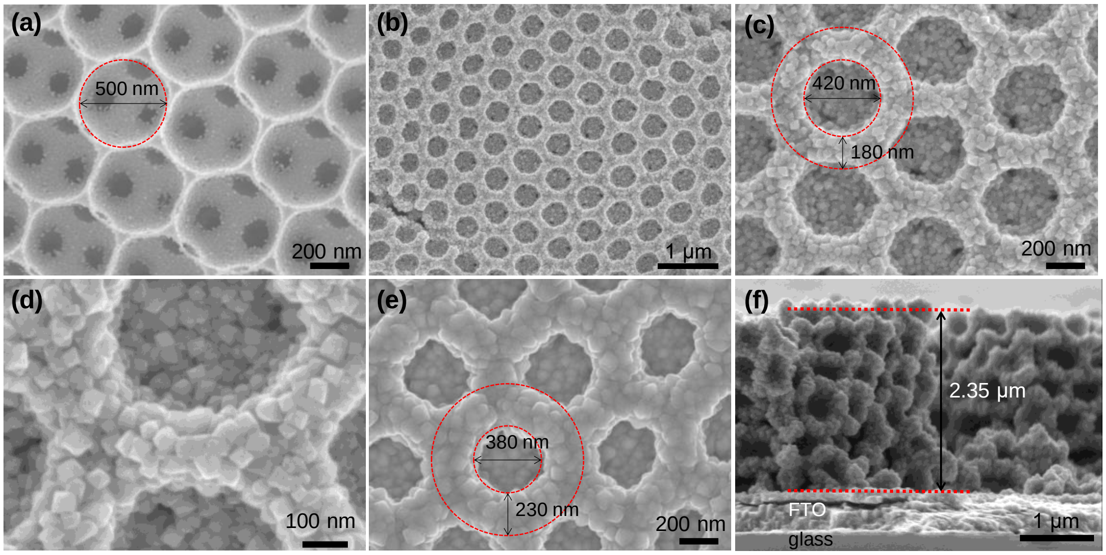

Figure 6.2 Top-view SEM images of: (a) FTO IOs; (b)-(d) FTO IOs/SnO_2 NCs; (e) FTO IOs/SnO_2 NCs/TiO_2; (f) Cross-section view of FTO IOs/SnO_2 NCs/TiO_2.

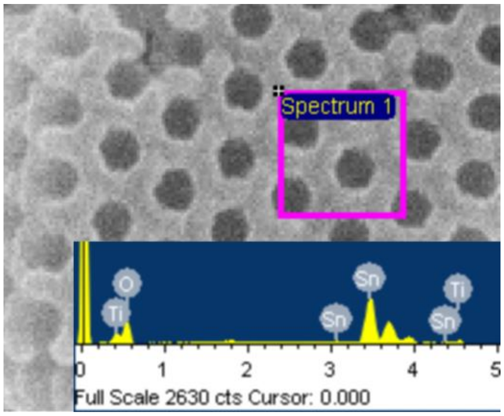

Figure 6.3 EDS of FTO IOs/SnO_2 NCs/TiO_2.

Figure 6.2(a) shows a top-view SEM image of the FTO IOs after the dip-coating process. The pore diameter of the as-fabricated FTO IOs is around 500 nm with a 33% shrinkage compared to that of the initial PS spheres (750 nm), while the FTO wall thickness is around 20 nm. After the hydrothermal process using 45 mg $SnCl_4$ and 1.3 ml HCl in the precursor solution, it can be clearly seen that the SnO_2 NCs grew well on the FTO void walls on a large scale without disrupting its structure (Figure 6.2(b)). The average wall thickness increased from 20 nm to 180 nm, while the pore diameter decreased to 420 nm, as shown in Figure 6.2(c). The diameter of the as-grown SnO_2 NCs was around 20 nm and their length was also around 30 nm, as shown in Figure 6.2(d). After ALD of TiO_2, the pore diameter of the FTO IOs/SnO_2 NCs/TiO_2 further decreases to 380 nm, as shown in Figure 6.2(e), indicating that the TiO_2 thin film has a thickness of around 20 nm. The growth rate of the ALD TiO_2 was about 0.05 nm per cycle in our study, which value is consistent with a previous report on growing TiO_2 by ALD.[39] The vanishing of the gaps between the SnO_2 NCs also indicates the conformal coating of ALD TiO_2 layers. Figure 6.2(f) shows the cross-section SEM image of FTO IOs/SnO_2 NCs/TiO_2. The periodical structure of the composite IO is well maintained and the hybrid ALD TiO_2 coated SnO_2 NCs are uniformly attached to the FTO IOs. The thickness of the as-prepared FTO IOs/SnO_2 NCs/TiO_2 is about 2.5 μm. EDS further confirms the existence of Sn, O, Ti elements in this composite IO, as shown in Figure 6.3.

Furthermore, the microstructure of the FTO IOs/SnO_2 NCs/TiO_2 was characterized by the TEM and HRTEM. Figure 6.4(a) clearly shows the pore structure of the FTO IOs/SnO_2 NCs/TiO_2. Figure 6.4(b) shows the measured *d* spacing of 0.248 nm can be indexed to (101) plane of rutile TiO_2, while 0.33 nm belongs to (110) plan of SnO_2. The inset image in Figure 6.4(b) is a selected area diffraction (SAED) pattern, showing the polycrystalline structure of the FTO IOs/SnO_2 NCs/TiO_2. Figure 6.4(c) shows the XRD patterns of the FTO IOs/SnO_2 NCs/TiO_2 obtained by a hydrothermal process with 45 mg $SnCl_4$ and 1.3 ml HCl used in the reaction precursor and after 400 ALD cycles of TiO_2 deposition. For comparison, the XRD pattern of the FTO IOs/SnO_2 NCs is also presented. The peaks at 27°, 34°, 38° and 52° could be ascribed to (110), (101), (200), and (211) planes of rutile phase of SnO_2, while the XRD peaks for TiO_2 cannot be observed. This could be due to the overlapping of the XRD patterns of TiO_2 and SnO_2. It may also be due to the ALD TiO_2 being too thin (~20 nm) for XRD detection. Raman spectra were further utilized to investigate the crystal phase of the thin ALD TiO_2 layers on the FTO IOs/SnO_2 NCs (red curve), together with the Raman spectrum of the FTO IOs/SnO_2 NCs (black curve), as shown in Figure 6.4(d). The Raman peaks at 476 cm^{-1}, 635 cm^{-1} and 777 cm^{-1} can be ascribed to E_g, A_{1g} and B_{2g} mode of SnO_2 while peaks at 150 cm^{-1}, 236 cm^{-1}, 444 cm^{-1} and 609 cm^{-1} can be ascribed to rutile TiO_2,[40] which is in accordance with our HRTEM results. It should be noticed that the phase of the TiO_2 films by ALD is normally anatase phase,

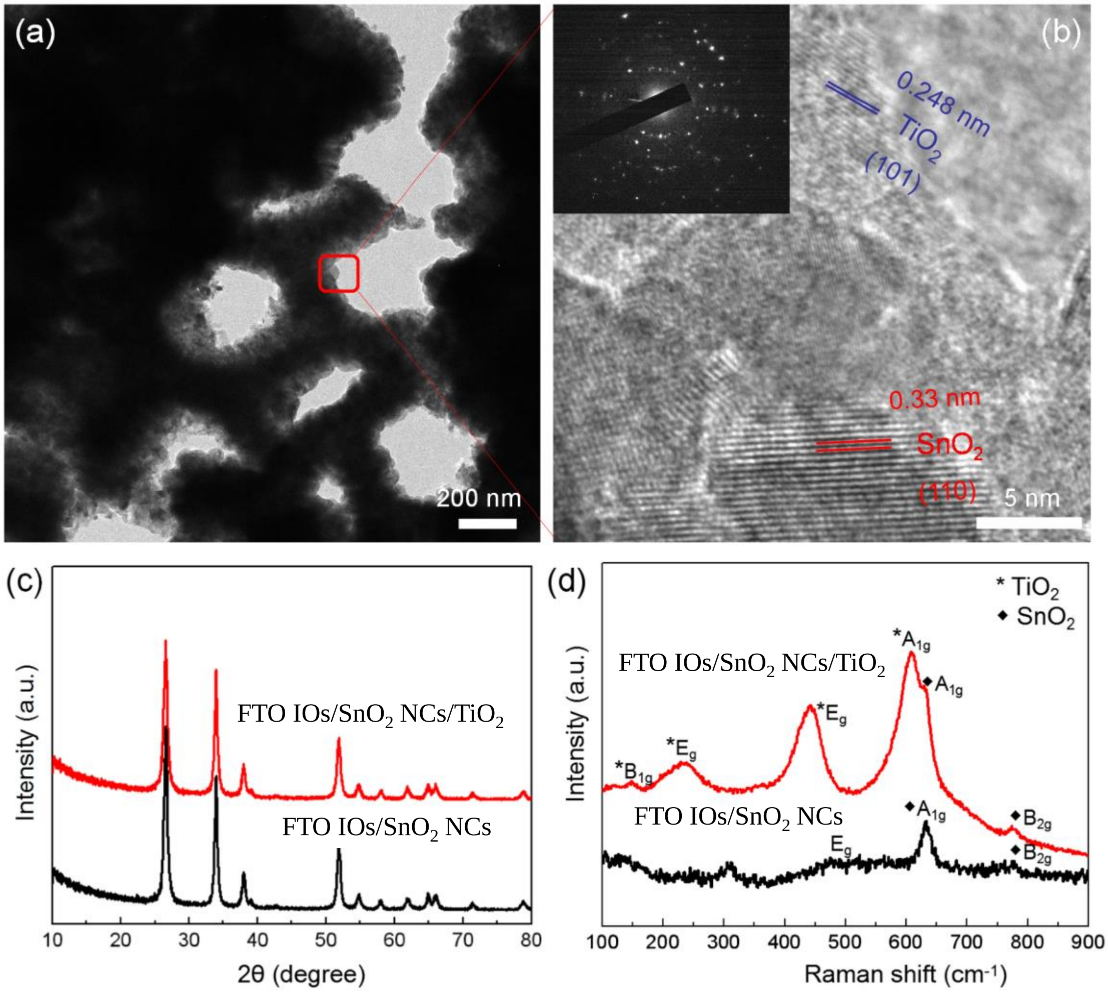

Figure 6.4 (a) TEM image of FTO IOs/SnO_2 NCs/TiO_2; (b) The HRTEM image of FTO IOs/SnO_2 NCs/TiO_2, the inset in (b) shows the SAED patterns; (c) XRD of FTO IOs/SnO_2 NCs and FTO IOs/SnO_2 NCs/TiO_2; (d) Raman spectra of FTO IOs/SnO_2 NCs and FTO IOs/SnO_2 NCs/TiO_2.

however, in this study, the TiO_2 films coated on rutile FTO IOs/SnO_2 NCs substrate is rutile, which could be due to their preferential formation on rutile SnO_2 surface due to the lattice match between rutile TiO_2 and SnO_2.[25]

To investigate the hydrothermal growth of the SnO_2 NCs on FTO IOs/SnO_2 NCs, the products obtained at different amounts of $SnCl_4$ and HCl added in the precursor solution

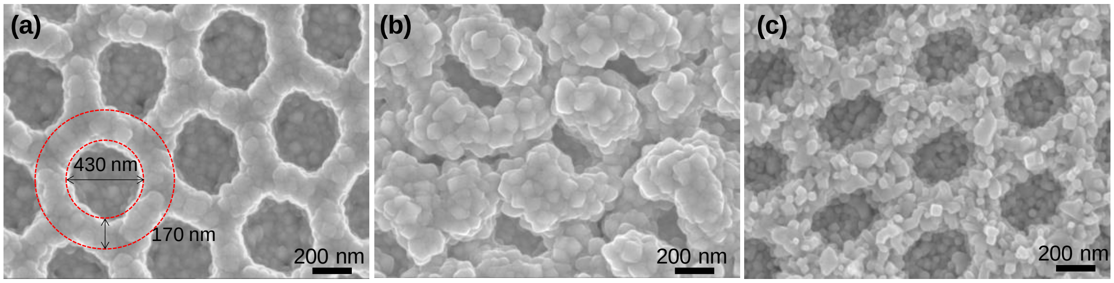

Figure 6.5 Top-view SEM images of FTO IOs/SnO_2 NCs/TiO_2 obtained with different amounts of $SnCl_4$ and HCl: (a) 30 mg $SnCl_4$ and 1.3 ml HCl; (b) 60 mg $SnCl_4$ and 1.3 ml HCl; (c) 45 mg $SnCl_4$ and 2 ml HCl.

were observed using SEM. Figure 6.5(a) and 6.5(b) show the FTO IOs/SnO_2 NCs/TiO_2 obtained with 30 mg and 60 mg $SnCl_4$ added in the precursor solution, respectively, while the HCl added amount was fixed to 1.3 ml. It can be clearly seen that with the decrease of the $SnCl_4$ precursor amount (30 mg), the pore diameter of the composite structure increases while the wall thickness decreases, indicating the smaller density and size of the SnO_2 NCs grown on the composite IO structure. Furthermore, the pore diameter of the composite structure decreases and even disappears with an excessive amount of $SnCl_4$ precursor amount (60 mg), which disrupts the periodical structure of the inverse opal. Figure 6.5(c) shows the SEM image of the as-fabricated FTO IOs/SnO_2 NCs/TiO_2 with an increased amount of HCl (2 ml) used in the precursor solution while the $SnCl_4$ precursor amount was kept at 45 mg. Through the comparison of Figure 6.2(e) and Figure 6.5(c), it can be observed that the length of the as-grown SnO_2 NCs increases when more HCl is added in the reaction precursor. Thus, the length, diameter, and density of the SnO_2 NCs can be adjusted by changing the amount of the $SnCl_4$ and HCl used in the hydrothermal process.

The light absorption of as-prepared samples was characterized by diffuse reflectance with an integrating sphere, as shown in Figure 6.6. The obvious band edge absorption of TiO_2 was observed around 380 nm for the composite opal structures. SnO_2 has a wide bandgap of 3.6 eV, corresponding to the optical band edge of 340 nm. Due to the existence of prominent noise between 300 nm-350 nm, the optical response of SnO_2 can not be directly

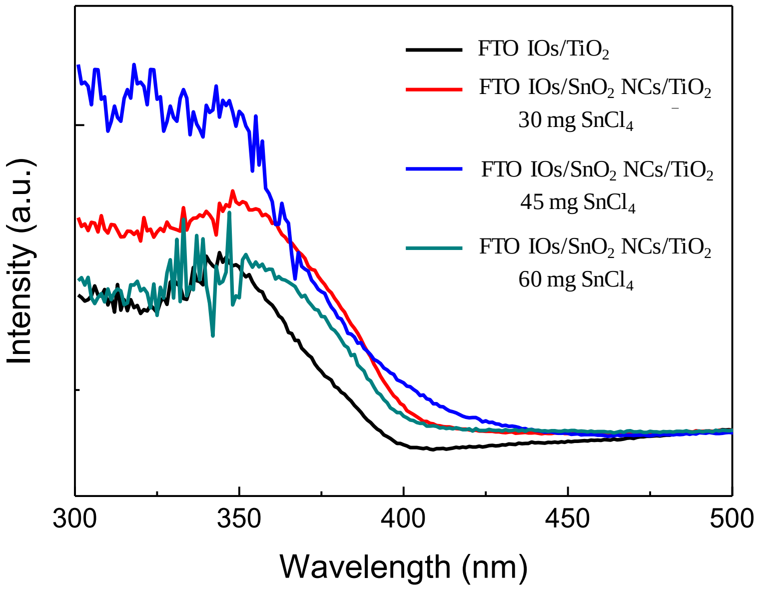

Figure 6.6 Absorption spectra of FTO IOs/TiO_2 and FTO IOs/SnO_2 NCs/TiO_2 prepared with different amounts of $SnCl_4$.

observed. The absorption edges of FTO/TiO_2 and FTO/SnO_2 NCs are mainly determined by photoactive TiO_2 films due to the lower bandgap. The direct light absorption of SnO_2 NCs has little contribution to the photocurrent due to the large bandgap. However, SnO_2 NCs act as the host scaffold could influence the loading amount of photoactive TiO_2 films, thus affecting the light absorption of the hierarchical nanostructures. It was observed that the light absorption of the as-prepared FTO IOs/SnO_2 NCs/TiO_2 structures first increased and then decreased when the amount of $SnCl_4$ precursor used during the hydrothermal process increased from 30 mg to 45 mg and then to 60 mg. That could be due to the increase in $SnCl_4$ precursor amount from 30 mg to 45 mg, resulting in more SnO_2 NCs grown on the FTO IOs. The larger surface area of the FTO IOs/SnO_2 NCs means more ALD photoactive TiO_2 can be deposited on them. However, further increasing the $SnCl_4$ precursor amount to 60 mg leads to the disruption of the periodical structure of the inverse opal, which causes a decrease of the multi-scattering inside the structure, hence reducing light absorption.[16] Thus, the light absorption of FTO IOs/SnO_2 NCs/TiO_2 will first increase, then reach a maximum value and after which it will decrease.

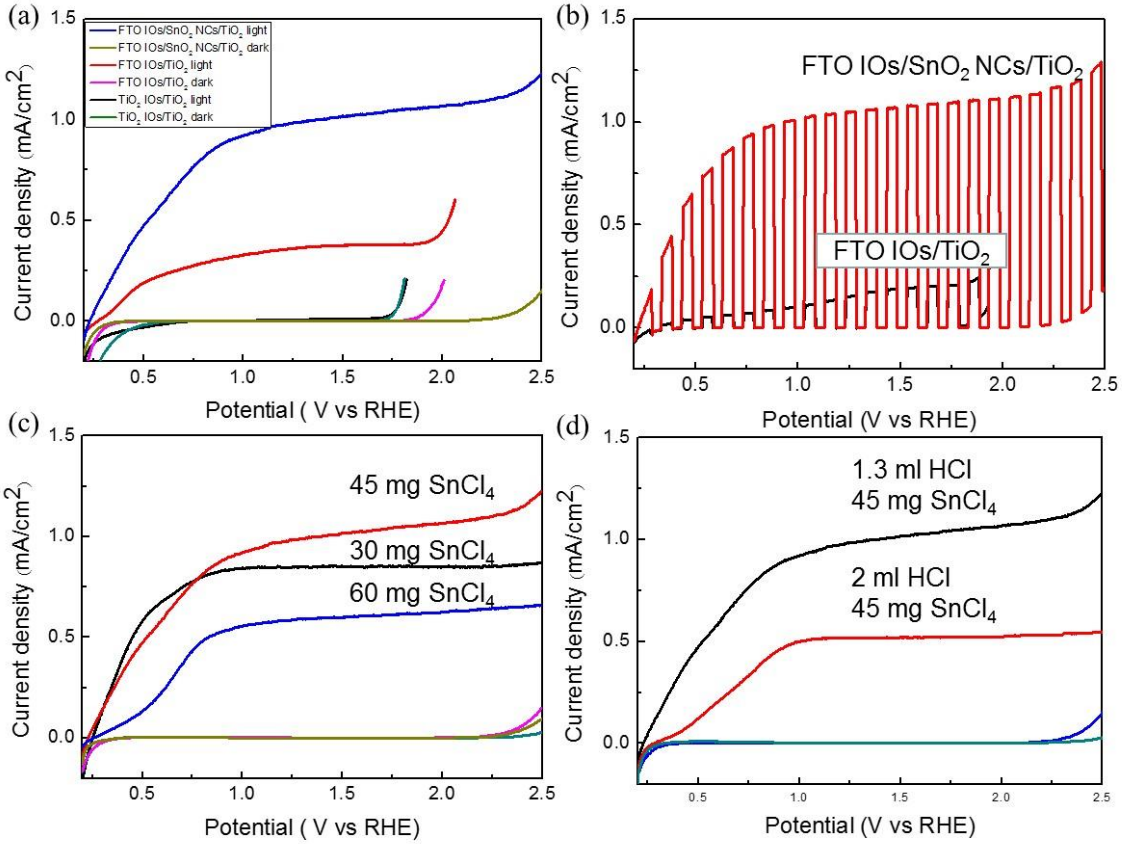

Figure 6.7 (a) Linear sweep curves of TiO_2 IOs, FTO IOs/TiO_2 and FTO IOs/SnO_2 NCs/TiO_2 electrodes; (b) Linear sweep curves of FTO IOs/TiO_2 and FTO IOs/SnO_2 NCs/TiO_2 electrodes under chopped light illumination with a light on/off cycles; (c) Linear sweep curves of FTO IOs/SnO_2 NCs/TiO_2 electrode prepared with different amounts of $SnCl_4$; (d) Linear sweep curves of FTO IOs/SnO_2 NCs/TiO_2 electrode prepared with different amounts of HCl.

6.3.2 PEC performance

Figure 6.7(a) shows the photocurrent of the FTO IOs/SnO_2 NCs/TiO_2, FTO IOs/TiO_2 and TiO_2 IO electrodes collected under both dark and illumination conditions. The FTO IOs/SnO_2 NCs/TiO_2 electrode shows a better PEC performance in contrast with the bare TiO_2 IO and FTO IOs/TiO_2 electrodes. The photocurrent density of the FTO IOs/SnO_2 NCs/TiO_2 electrode reaches 1.0 mA cm^{-2} at 1.23 V vs. RHE, which is 4 times that of the FTO IOs/TiO_2 (0.25 mA cm^{-2}) and much larger than that of the bare TiO_2 IOs electrode (0.006 mA cm^{-2}) prepared by ALD. The photocurrent density of FTO IOs/TiO_2 and TiO_2

IOs electrodes are 0.25 and 0.006 mA cm^{-2} at 1.23 V vs. RHE, respectively. These values are comparable to the previous reports.[27, 41] It should be noted that the bare TiO_2 IO electrode was prepared with 600 ALD TiO_2 cycles since the opal structure collapsed when the ALD TiO_2 layer was too thin. Figure 6.7(b) shows the linear sweep curves of the FTO IOs/SnO_2 NCs/TiO_2 and FTO IOs/TiO_2 electrodes under chopped light illumination, both samples display fast response and low recovery time.

To investigate the effect of the size, length and density of the SnO_2 NCs grown on the FTO IOs surface on the PEC performance, the samples were prepared with different amounts of $SnCl_4$ as well as HCl precursor, SEM images of the resultant samples are shown in Figure 6.2 and 6.5. The photocurrent density of the FTO IOs/SnO_2 NCs/TiO_2 electrode at 1.23 V vs. RHE increased from 0.8 to 1.0 mA cm^{-2}, and dropped to 0.6 mA cm^{-2} when the amount of the $SnCl_4$ precursor used during the hydrothermal reaction increased from 30 mg to 45 mg and then to 60 mg, as shown in Figure 6.7(c). These results are consistent with the light absorption testing. The change in the morphology of the as-prepared samples causes variations in the light absorption and thus induces a change in their photocurrent density. The influence of the length of the SnO_2 NCs on the photocurrent of the as-fabricated FTO IOs/SnO_2 NCs/TiO_2 electrode was also investigated. The length of the SnO_2 NCs can be adjusted by changing the HCl amount as discussed previously. However, when the length of the SnO_2 increased, the photocurrent of the FTO IOs/SnO_2 NCs/TiO_2 decreased, as shown in Figure 6.7(d). This could be due to fewer F^- ions diffusing from the FTO IOs underlay during the second post-annealing process. Thus, the conductivity of the shorter SnO_2 NCs is better than the longer ones, resulting in better PEC performance.

The IPCE was performed to further investigate the PEC performance of as-prepared samples, which is defined by the following equation (1):

$$\mathrm{IPCE} = (1024\mathrm{I})/(\lambda J_{light}) \qquad (1)$$

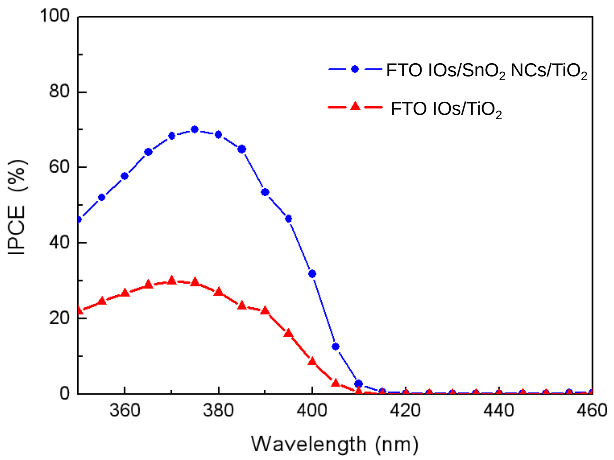

Figure 6.8 IPCE plots of FTO IOs/TiO_2 electrode and FTO IOs/SnO_2 NCs/TiO_2 electrode collected at 1.23 V vs. RHE.

Where λ is the wavelength of the incident light, I is the corresponding photocurrent density and J_{light} is power density of the incident light.

Figure 6.8 shows that FTO IOs/SnO_2 NCs/TiO_2 electrode has higher IPCE maximum (70%) in the wavelength between 350-430 nm compared to that of FTO IOs/TiO_2 electrode (29%), which could be ascribed to the higher specific surface area, improved charge transport and separation efficiency and enhanced light scattering ability due to the growth of SnO_2 NCs.

To investigate the influence of the thickness of ALD TiO_2 layers on the PEC performance of the FTO IOs/SnO_2 NCs/TiO_2 electrode, samples were fabricated using different numbers of ALD TiO_2 cycles. Figure 6.9(a) shows that the FTO IOs/SnO_2 NCs/TiO_2 electrode with 400 ALD TiO_2 cycles shows the best PEC performance. When the ALD photoactive TiO_2 layer is too thin, the light absorption of the as-obtained FTO IOs/SnO_2 NCs/TiO_2 electrode is insufficient. Alternatively, when the TiO_2 layer is too thick, the lowered mobility of the TiO_2 will result in a rise of charge recombination rate and hence worsens the PEC performance of the overall electrode.[21]

As previously mentioned, a stop-flow ALD mode ensures a conformal and uniform coating of the TiO_2 layer over the high porous FTO IOs/SnO_2 NCs structure. For comparison, the FTO IOs/SnO_2 NCs/TiO_2 electrode was also prepared using a normal continuous flow ALD

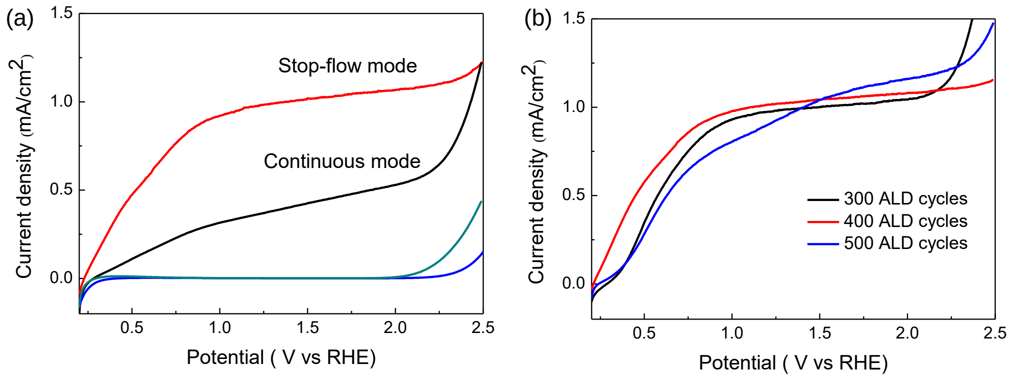

Figure 6.9 (a) Linear sweep curves of FTO IOs/SnO_2 NCs/TiO_2 electrode prepared with different ALD modes; (b) Linear sweep curves of FTO IOs/SnO_2 NCs/TiO_2 electrode prepared with different ALD cycles.

process with the same number of ALD cycles. The tested photocurrent results are shown in Figure 6.9(b). FTO IOs/SnO_2 NCs/TiO_2 electrode prepared with stop-flow ALD process shows higher photocurrent than that prepared by a continuous flow ALD process, which can be ascribed to the non-uniform coating of TiO_2 by the continuous flow ALD process over the highly porous nanostructure as reported in our previous study.[37]

To further investigate the kinetics of the charge transfer process of the various electrodes, EIS measurements were performed. The EIS Nyquist plots of the as-prepared IO electrodes are shown in Figure 6.10(a). The charge transfer resistance at the electrolyte/photoanode interface can be reflected by the diameter of the semicircular portion in the Nyquist plots. FTO IOs/SnO_2 NCs/TiO_2 electrode shows lower charge transfer resistance than that of the FTO IOs/TiO_2 electrode, implying that the as-prepared FTO IOs/SnO_2 NCs skeleton facilitates charge transfer and electron collection. The measured resistance of the FTO IOs/SnO_2 NCs/TiO_2 with longer SnO_2 NCs is larger than that with short SnO_2 NCs. These results are consistent with the previous PEC performance test. The PEC process in the FTO IOs/SnO_2 NCs/TiO_2 electrode is schematically illustrated in Figure 6.10(b). Under illumination, electrons and holes are generated in the photoactive TiO_2 thin layers. Then, electrons are collected by the conductive FTO IOs/SnO_2 NCs and directly transferred to the Pt counter electrode to initialize the H_2 evolution. In this process, the band alignment between TiO_2 and SnO_2 could form a heterojunction, which further enhances the charge

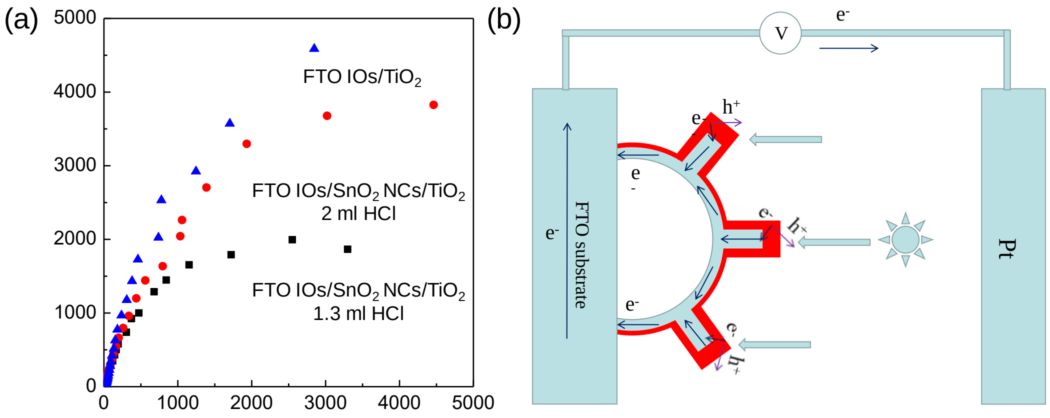

Figure 6.10 (a) EIS Nyquist plots of FTO IOs/TiO_2 and FTO IOs/SnO_2 NCs/TiO_2 electrodes prepared with different amounts of HCl; (b) The schematic diagram for charge transfer process in the FTO IOs/SnO_2 NCs/TiO_2.

separation efficiency. Specifically, electrons would transfer from a higher conduction band of TiO_2 to the lower conduction band of SnO_2, while holes in the valence band would move in the opposite way. The primary electron-hole recombination appears inside the photoactive TiO_2 layer itself. Since the thickness of the ALD TiO_2 layer is around 20 nm, which is comparable to the carrier diffusion length of TiO_2,[26] reducing the charge recombination, and thus resulting in a better PEC performance.

Among the TiO_2 based nanostructured photoanodes without the further combination of low bandgap semiconductors or other visible light sensitizers, the PEC performance of the as-prepared FTO IOs/SnO_2 NCs/TiO_2 electrode belongs to the forefront, as shown in Table 1. The high conductivity of the FTO IOs/SnO_2 NCs provides direct and fast electron transfer pathways, while the high specific surface area of such periodical host skeleton enables loading of sufficient photoactive materials and effective light scattering inside the structure, so the as-prepared FTO IOs/SnO_2 NCs/TiO_2 electrode exhibits higher photocurrent than that of considerable reported nanostructured TiO_2 electrodes.[14, 16, 25, 26, 42, 43] Although the photocurrent of the as-prepared FTO IOs/SnO_2 NCs/TiO_2 electrode is not the best, the utilization of conductive FTO IOs/SnO_2 NCs skeleton with high specific surface area to boost PEC efficiency of TiO_2 offered a general solution to enhance PEC performance of existing semiconductors.

Table 6.1. Comparison of PEC performance of reported TiO_2 based nanostructured photoanodes.

TiO_2 based photoanodes	Electrolyte	Photocurrent density [$mAcm^{-2}$]a)	Preparation method	Remarks
FTO IOs/SnO_2 NCs/TiO_2	1 NaOH	1.0	ALD	This work
Pristine TiO_2 nanorods	1M KOH	0.58	Hydrothermal	[14]
TiO_2 nanorod @nanobowl	1M KOH	1.24	Sol-gel & Hydrothermal	[16]
FTO nanoparticle films/TiO_2	1M KOH	0.75	ALD	[25]
ATO colloid films/TiO_2	1M KOH	0.65	ALD	[26]
Hierarchical TiO_2 urchins	1M NaOH	0.95	ALD	[42]
TiO_2/SnO_2 branched nanowires	1M NaOH	0.85	Hydrothermal	[43]

a) The photocurrent density was collected at 1.23V vs. RHE with AM 1.5 illumination (100 mW cm^{-2}).

6.4 Conclusions

In summary, a 3D FTO IOs/SnO_2 NCs/TiO_2 electrode was fabricated for PEC water splitting. Through the optimization of the density and sizes of the hydrothermally grown SnO_2 NCs, the as-fabricated FTO IOs/SnO_2 NCs/TiO_2 photoanodes presented enhanced PEC performance comparing to the reference FTO/TiO_2 IO photoanode. The significant PEC performance enhancement of such 3D FTO IOs/SnO_2 NCs/TiO_2 photoanode is ascribed to the high conductivity as well as the high specific surface area of the FTO IOs/SnO_2 NCs host skeleton, which improves charge collection and light absorption of TiO_2 films. Our results suggest that a highly conductive nanostructured host skeleton designed with tailored constitutes is a promising technique to boost the overall PEC performance of TiO_2 photoanodes. This strategy may also be applied to boost the PEC efficiency of other photoanodes, such as Fe_2O_3, $BiVO_4$, and WO_3 photoanodes.

References

[1] C. Ding, J. Shi, Z. Wang, C. Li, *ACS Catal*. **2017**, *7*, 675.

[2] C. Jiang, S.J. Moniz, A. Wang, T. Zhang, J. Tang, *Chem. Soc. Rev*. **2017**, *46*, 4645.

[3] K. Sivula, R. van de Krol, *Nature Rev. Mater.* **2016**, *1*, 15010.

[4] L. Mao, X. Cai, H. Gao, X. Diao, J. Zhang, *Nano Energy* **2017**, *39*,172.

[5] M. Zhong, T. Hisatomi, Y. Sasaki, S. Suzuki, K. Teshima, M. Nakabayashi, N. Shibata, H. Nishiyama, M. Katayama, T. Yamada, *Angew. Chem.-Int. Edit*. **2017**, *56*, 4739.

[6] J. Azevedo, S.D. Tilley, M. Schreier, M. Stefik, C. Sousa, J.P. Araújo, A. Mendes, M. Grätzel, M.T. Mayer, *Nano Energy* **2016**, *24*, 10.

[7] H. Han, F. Riboni, F. Karlicky, S. Kment, A. Goswami, P. Sudhagar, J. Yoo, L.Wang, O. Tomanec, M. Petr, O. Haderka, C. Terashima, A. Fujishima, P. Schmuki, R. Zboril, *Nanoscale* **2017**, *9*, 134.

[8] Y. Zhao, N. Hoivik, K. Wang, *Nano Energy* **2016**, *30*, 728.

[9] W. Chen, T. Wang, J. Xue, S. Li, Z. Wang, S. Sun, *Small* **2017**, *13*, 1602420.

[10] C. Chen, Y. Wei, G. Yuan, Q. Liu, R. Lu, X. Huang, Y. Cao, P. Zhu, *Adv. Funct. Mater*. **2017**, *27*, 1701575.

[11] Z. Pei, M. Zhu, Y. Huang, Y. Huang, Q. Xue, H. Geng, C. Zhi, *Nano Energy* **2016**, *20*, 254.

[12] M.Z. Ge, C.Y. Cao, S.H. Li, Y.X. Tang, L.N. Wang, N. Qi, J.Y. Huang, K.Q. Zhang, S.S. Al-Deyab, Y.K. Lai, *Nanoscale* **2016**, *8*, 5226.

[13] F. Wu, Y. Yu, H. Yang, L.N. German, Z. Li, J. Chen, W. Yang, L. Huang, W. Shi, L. Wang, *Adv. Mater*. **2017**, *29*, 1701432.

[14] H.-Y. Wang, H. Yang, L. Zhang, J. Chen, B. Liu, *ChemNanoMat.* **2016**, *2*, 660.

[15] X. Wang, R. Long, D. Liu, D. Yang, C. Wang, Y. Xiong, *Nano Energy* **2016**, 24 87.

[16] W. Wang, J. Dong, X. Ye, Y. Li, Y. Ma, L. Qi, *Small* **2016**, *12*, 1469.

[17] Y.-F. Xu, H.-S. Rao, X.-D. Wang, H.-Y. Chen, D.-B. Kuang, C.-Y. Su, *J. Mater. Chem. A* **2016**, *4*, 5124.

[18] Z. Bai, X. Yan, Y. Li, Z. Kang, S. Cao, Y. Zhang, *Adv. Energy Mater*. **2016**, *6*. 1501459.

[19] Z. Zhang, C. Gao, Y. Li, W. Han, W. Fu, Y. He, E. Xie, *Nano Energy* **2016**, *30*, 892.

[20] J. Yang, C. Bao, T. Yu, Y. Hu, W. Luo, W. Zhu, G. Fu, Z. Li, H. Gao, F. Li, Z. Zou, *ACS Appl. Mater. Interfaces* **2015**, *7*, 26482.

[21] Y. Mi, L. Wen, R. Xu, Z. Wang, D. Cao, Y. Fang, Y. Lei, *Adv. Energy Mater*. **2016**, *6*. 1501496.

[22] Y.F. Xu, H.S. Rao, B.X. Chen, Y. Lin, H.Y. Chen, D.B. Kuang, C.Y. Su, *Adv. Sci*. **2015**, *2*, 1500049.

[23] X.D. Wang, Y.F. Xu, B.X. Chen, N. Zhou, H.Y. Chen, D.B. Kuang, C.Y. Su, *ChemSusChem*. **2016**, *9*, 3012.

[24] L. Zhou, C. Zhao, B. Giri, P. Allen, X. Xu, H. Joshi, Y. Fan, L.V. Titova, P.M. Rao, *Nano Lett*. **2016**, *16*, 3463.

[25] I.A. Cordova, Q. Peng, I.L. Ferrall, A.J. Rieth, P.G. Hoertz, J.T. Glass, *Nanoscale* **2015**, *7*, 8584.

[26] Q. Peng, B. Kalanyan, P.G. Hoertz, A. Miller, D.H. Kim, K. Hanson, L. Alibabaei, J. Liu, T.J. Meyer, G.N. Parsons, *Nano Lett*. **2013**, *13*, 1481.

[27] H. Zhang, C. Cheng, *ACS Energy Lett*. **2017**, *2*, 813.

[28] H. Zhang, W. Zhou, Y. Yang, C. Cheng, *Small* **2017**, *13*, 1603840.

[29] R. Boppella, S.T. Kochuveedu, H. Kim, M.J. Jeong, F. Marques Mota, J.H. Park, D.H. Kim, *ACS Appl. Mater. Interfaces* **2017**, *9*, 7075.

[30] K.-H. Ye, Z. Wang, J. Gu, S. Xiao, Y. Yuan, Y. Zhu, Y. Zhang, W. Mai, S. Yang, *Energy Environ. Sci*. **2017**, *10*, 772.

[31] M. Curti, J. Schneider, D.W. Bahnemann, C.B. Mendive, *J. Phys. Chem. Lett.* **2015**, *6*, 3903-3910.

[32] Y. Gun, G.Y. Song, V.H. Quy, J. Heo, H. Lee, K.S. Ahn, S.H. Kang, *ACS Appl. Mater. Interfaces* **2015**, *7*, 20292.

[33] S.K. Karuturi, J. Luo, C. Cheng, L. Liu, L.T. Su, A.I. Tok, H.J. Fan, *Adv. Mater*. **2012**, *24*, 4157.

[34] L. Wen, M. Zhou, C. Wang, Y. Mi, Y. Lei, *Adv. Energy Mater*. **2016**, 6, 1600468.

[35] C. Cheng, S.K. Karuturi, L. Liu, J. Liu, H. Li, L.T. Su, A.I. Tok, H.J. Fan, *Small* **2012**, *8*, 37.

[36] M. Kulmas, L. Paterson, K. Höflich, M.Y. Bashouti, Y. Wu, M. Göbelt, J. Ristein, J. Bachmann, B. Meyer, S. Christiansen, *Adv. Funct. Mater*. **2016**, *26*, 4882.

[37] X. Li, M. Puttaswamy, Z. Wang, T.C. Kei, A.C. Grimsdale, N.P. Kherani, A.I.Y. Tok, *Appl. Surf. Sci*. **2017**, *422*, 536.

[38] X. Chen, J. Ye, S. Ouyang, T. Kako, Z. Li, Z. Zou, *ACS Nano* **2011**, *5*, 4310.

[39] A. Moya, N. Kemnade, M. Osorio, A. Cherevan, D. Granados, D. Eder, J. Vilatela,

J. Mater. Chem. A **2017**, *5*, 24695.

[40] S.F. Shaikh, R.S. Mane, O.-S. Joo, *RSC Adv*. **2014**, *4*, 35919.

[41] Z. Chen, L. Fang, W. Dong, F. Zheng, M. Shen, J. Wang, *J. Mater. Chem. A* **2014**, *2*, 824.

[42] W. Ren, H. Zhang, D. Kong, B. Liu, Y. Yang, C. Cheng, *Phys. Chem. Chem. Phys.* **2014**, *16*, 22953.

[43] C. Cheng, W. Ren, H. Zhang, *Nano Energy* **2014,** *5*, 132-138.

[44] M. Zalfani, B. van der Schueren, Z.-Y. Hu, J.C. Rooke, R. Bourguiga, M. Wu, Y. Li, G. Van Tendeloo, B.-L. Su, *J. Mater. Chem. A*. **2015**, *3*, 21244.

[45] Y. Sun, W.D. Chemelewski, S.P. Berglund, C. Li, H. He, G. Shi, C.B. Mullins, *ACS Appl. Mater. Interfaces* **2014**, *6*, 5494.

Chapter 7*

Periodic FTO IOs/CdS NRs/CdSe Clusters with Superior Light Scattering Ability for Improved photoelectrochemical Performance

In this chapter, periodic fluorine-doped tin oxide inverse opals (FTO IOs) grafted with CdS nanorods (NRs) and CdSe clusters are reported for improved photoelectrochemical (PEC) performance. The growth of one-dimensional (1D) CdS NRs on the periodic walls of three-dimensional (3D) FTO IOs forms a unique 3D/1D hierarchical structure, providing a sizeable specific surface area for the loading of CdSe clusters. Significantly, the periodic FTO IOs enable uniform light scattering whilst the abundant surrounded CdS NRs induce additional random light scattering, combining to give multiple light scattering within the complete hierarchical structure, significantly improving light-harvesting of CdS NRs and CdSe clusters. The high electron collection ability of FTO IOs and the CdS/CdSe heterojunction formation also contribute to the enhanced charge transport and separation. Due to the incorporation of these enhancement strategies in one hierarchical structure, FTO IOs/CdS NRs/CdSe clusters present an improved PEC performance. The photocurrent density of FTO IOs/CdS NRs/CdSe clusters at 1.23 V versus reversible hydrogen electrode reaches 9.2 mA cm^{-2}*, which is 1.43 times greater than that of CdS NRs/CdSe clusters and 3.83 times of CdS NRs.*

---

*This section is published substantially as Z. Wang, et al. *Small* **2020**, *16*, 1905826.

7.1 Introduction

Photoelectrochemical (PEC) water splitting enables the utilization of unlimited solar energy to produce clean and renewable hydrogen fuel, offering a promising route to reduce carbon dioxide emissions and mitigate the energy crisis.[1-5] To achieve a high energy conversion efficiency, photoelectrodes should have a sufficient light absorption, quick charge separation, fast kinetics of surface reactions, and excellent photostability.[6, 7] However, photoelectrodes fabricated with a single semiconductor cannot simultaneously fulfill these requirements. Several methods, such as morphology manipulation,[8, 9] fabrication of heterojunctions,[10] surface coating with protection layer or electrocatalyst,[11-13] have been proposed to improve the PEC performance. As bulk semiconductors usually suffer from low light scattering and small specific surface area, a large thickness is needed to bring about sufficient light absorption. However, this would unavoidably increase the charge recombination rate, especially in semiconductors with a small diffusion length of minority carriers or low electrons mobility.[14, 15] The development of nanostructured semiconductors provides a solution to overcome this dilemma due to their unique properties. For example, zero-dimensional (0D) quantum dots (QDs) with adjustable bandgap can achieve strong visible light absorption.[16] One-dimensional (1D) nanorods (NRs) provide direct pathways for electrons transport and reduce length for holes diffusion.[17] Two-dimensional (2D) nanosheets (NSs) have a large active surface area and a low density of grain boundaries along charge-transport paths.[18] Three-dimensional (3D) inverse opals (IOs) provide high surface area and enhanced light-matter interactions.[19]
Furthermore, some host/guest hierarchical structures fabricated with different dimensional nanostructures, such as 3D SnO_2 nanobowls/1D CdS NRs,[20] 3D TiO_2 IOs/1D ZnO NRs,[21] and 2D WO_3 NSs/1D Bi_2S_3 NRs,[22] have been reported to show higher PEC performance due to the synergistic effects of these component nanostructures. In these nanostructures, host materials usually have a large specific surface area and high chemical stability, acting as a skeleton for the secondary growth of guest materials, which can enable wide-spectrum light absorption due to their lower bandgap.[23, 24] The PEC performance of hierarchical structures can be further enhanced by using a highly conductive material as the host skeleton, which can quickly collect electrons generated in the guest materials and thus

lowering bulk charge recombination.[25, 26] Tin oxide with high transparency in the visible area and high chemical stability is one of the promising candidate materials.[27, 28] Among various tin oxide nanostructures, fluorine-doped tin oxide (FTO) IOs have attracted much attention for their high porosity, strong light manipulation ability, and excellent electrical conductivity.[29, 30] Several FTO IOs/guest film photoelectrodes, such as FTO IOs/TiO_2 film,[29] and FTO IOs/TiO_2/$BiVO_4$ film,[31] have been developed. However, research on the FTO IOs based hierarchical structures is still limited. As host/guest hierarchical structures have the potential for superior properties, it is desirable to combine 3D FTO IOs with other dimensional nanostructured semiconductors to form novel hierarchical photoelectrodes.

CdS and CdSe are two promising guest semiconductors that have been extensively investigated for the fabrication of effective photoanodes. Due to the small bandgap, they have strong visible light absorption, thus ensuring a sufficient generation of electron-hole pairs.[32-35] The co-deposition of CdS and CdSe QDs to form CdS/CdSe nanojunction has been successfully achieved, such as CdSe/CdS/TiO_2/indium-tin-oxide nanowire array,[36] and CdS/CdSe QDs co-sensitized TiO_2 nanocable arrays,[37] CdS/CdSe co-sensitized brookite H:TiO_2 nanostructures,[38] CdS/CdSe co-sensitized ZnO porous nanotube arrays.[39] Compared to CdS QDs or CdS films, CdS NRs have better PEC performance due to the presence of direct pathways for electron transportation and its larger specific surface area.[20, 40] Although the combination of CdSe nanostructures with CdS NRs has been investigated for PEC applications,[41] the utilization of 3D FTO IOs as a host skeleton to further improve their PEC performance has yet to be investigated. Herein, the periodic FTO IOs/CdS NRs/CdSe clusters as a novel host/guest photoanode is designed and fabricated for the improved PEC performance. In this hierarchical photoanode, FTO IOs play the role of the conductive skeleton to collect electrons and offer a large surface area for the secondary growth of CdS NRs, while CdS NRs carry out visible light absorption and serve to a further increase in surface area for the loading of CdSe clusters. The loading of CdSe QDs further extends the range of light absorption and forms a heterojunction with CdS NRs, enhancing the charge generation and separation efficiency. Furthermore, this 3D periodic FTO IOs/1D CdS NRs structure provides a large surface area and enables multiple light scattering within the hierarchical nanostructure, thereby increasing the active reaction area and the light-harvesting efficiency. Due to these synergistic effects in the hierarchical structure, FTO IOs/CdS NRs/CdSe clusters show a better PEC performance than pristine CdS NRs and CdS NRs/CdSe clusters.

7.2 Experimental Section

7.2.1 Materials

Fluorine-doped tin oxide (FTO) glasses were obtained from Pilkington (Model: Tec-7, 8 Ω sq^{-1}). Tin(IV) chloride pentahydrate ($SnCl_4 \cdot 5H_2O$), ammonium fluoride (NH_4F), cadmium nitrate, thiourea, glutathione, KOH, and absolute ethanol were purchased from Sigma-Aldrich. Se powders were ordered from Kanto Chemical. Polystyrene (PS) microspheres dispersion (870 nm, 500 nm, and 300 nm, 10 wt%) were ordered from Duke Corporation.

7.2.2 Preparation of PS Opals

The preparation of PS opals on the FTO coated glass substrate (FTO substrate/PS opals) was achieved by an evaporation-induced self-assembly method. FTO substrates (1.5 cm × 5 cm) were sonicated in acetone, methanol, ethanol and deionized (DI) water for 30 minutes each. After sonication, a piece of hydrophilic FTO substrate was put into a 5 ml beaker with a conductive side facing up and then soaked with a diluted solution of PS particles (4.5 ml, 0.2 wt%). Each time, up to nine as-prepared 5ml beakers would be transferred together to a temperature-controlled oven and covered with a larger beaker. The oven was maintained at 50 °C and then kept for 72 hours to control the vaporization rate of water that initiates the assembly of PS microspheres. In the last step, the as-prepared FTO substrates/PS opals were placed in an oven at 90 °C for another 2 h to increase the mechanical strength.

7.2.3 Preparation of FTO IOs

FTO IOs were prepared by a forced impregnation method with PS opals as sacrificial templates. FTO precursor solution was prepared with $SnCl_4$ (2.8 g), NH_4F (25 mg), and absolute ethanol (40 ml). Before the soaking in the precursor solution, FTO substrates/PS opals were immersed in methanol for 10 minutes. Then, FTO substrates/PS opals sample was soaked in a 5 mL beaker full of FTO precursor solution before being transferred to a suction flask, which was connected to a vacuum pump. Then the suction flask was evacuated for 30 mins. After that, the infiltrated samples were taken out from the beaker and placed vertically for sample drying. Finally, the samples were annealed at 500 °C under air for 2 h with a moderate ramp rate of 1°C/min to melt the PS opals and crystallize the resultant FTO IOs at the same time.

7.2.4 Preparation of FTO IOs/CdS NRs

FTO IOs/CdS NRs were prepared by a hydrothermal reaction. The precursor for the growth of CdS NRs was prepared with cadmium nitrate (69 mg), thiourea (17 mg), glutathione (41 mg), and DI water (15 ml). An FTO substrate coated with FTO IOs was placed in a 25 mL Teflon-lined autoclave with its conductive side facing down. The as-prepared precursor was then added into the autoclave before it was sealed and placed in a temperature-controlled oven at 200 °C for 2 h. After the reaction, the autoclave was cooled down to room temperature. The obtained FTO IOs/CdS NRs sample was then rinsed with DI water and then dried with N_2 flow, followed by post-annealing at 450 °C for 1 hour under the protection of Argon.

A control sample was fabricated via the same process, except for the use of pure FTO substrate instead of FTO IOs.

7.2.5 Preparation of FTO IOs/CdS NRs/CdSe Clusters

FTO IOs/CdS NRs/CdSe clusters were obtained by a chemical bath deposition method under N_2 flow. Se powder (0.789g), Na_2SO_3 (3.15g) and DI water (50 mL) were added to a three-necked round bottom flask. Prior to heating, the flask was first bubbled with N_2 gas for 20 min to remove the air. Then, the solution was maintained at 70 °C and refluxed for 10 h to form the solution of Na_2SeSO_3. In a separate beaker, KOH (0.505 g) and nitrilotriacetic acid (0.57 g) were dissolved in 100 mL DI water. $Cd(NO_3)_3 \cdot 4H_2O$ (0.617 g) was then added to the above solution and stirred for 20 min to get a transparent solution. Several FTO IOs/CdS NRs samples were placed in this transparent solution, which was then bubbled with nitrogen gas for 20 min and kept at 70 °C for 10 min. Next, 10 ml of Na_2SeSO_3 solution was quickly transferred to the transparent solution. The mixed solution was maintained at 70 °C for 1 hour and then cooled down to room temperature naturally. The samples were rinsed with DI water for several times, then dried in a vacuum furnace.

7.2.6 Material Characterization

Field-emission scanning electron microscope (FESEM, JEOL, JSM 7600F) and scanning transmission electron microscope (STEM, JEOL 2100F equipped with INCA Energy Dispersive X-ray spectrometer detector) were used to investigate the microstructure, morphology and the elemental composition of the as-prepared samples. The X-ray diffraction pattern was carried out on a Bruker D8 X-ray diffractometer, equipped with Cu-Kα radiation source. X-ray photoelectron spectroscopy was collected on a multichannel energy analyzer (SPECS Phoibos 100 MCD-5) with a monochromatic Ma Kα source at 1253 eV. The calibration was achieved by C 1s (284.5 eV). UV-Vis diffuse reflectance spectra and transmission spectra were collected on a Varian, Cary 5000 spectrophotometer. Photoluminescence spectra were collected on a Cary photoluminescence spectrophotometer.

7.2.7 PEC Measurement

PEC performance was tested with an Autolab 270 workstation under AM 1.5G sunlight illumination (100 mW cm^{-2}). The simulated sunlight was provided by a solar simulator (300W Xe lamp, Newport). In the three-electrode electrochemical system, the working electrode, counter electrode, and reference electrode are the as-prepared nanostructures, platinum mesh, and Ag/AgCl, respectively. 0.25 M Na_2SO_3 and 0.35 M Na_2S mix solution were selected as the electrolyte for the PEC measurements. The measurement of electrochemical impedance spectroscopy (EIS) was carried out on the same system. The frequency ranged from 10^{-1} to 10^5 Hz and amplitude was 10 mV. The incident-photon-to-current conversion efficiency (IPCE) was measured by a two-electrode configuration under 0 V bias using the Zolix Solar cell Scan100. Mott-Schottky measurements were performed in a 0.5 M Na_2SO_4 solution under the dark condition with a three-electrode configuration. Electrochemical active surface area measurements were performed in the 0.25 M Na_2SO_3 and 0.35 M Na_2S mix solution under the dark condition with a three-electrode configuration. Open circuit voltage decay was measured in 0.25 M Na_2SO_3 and 0.35 M Na_2S mix solution with a three-electrode configuration.

7.3 Results and discussions

7.3.1 Fabrication and Characterization

The fabrication process of FTO IOs/CdS NRs/CdSe clusters is illustrated in Figure 7.1. Periodic polystyrene (PS) opals, with a face-centered cubic structure, were coated on the FTO glass substrate through an evaporation-induced self-assembly method. FTO IOs were fabricated by a forced impregnation method with as-prepared PS opals as the sacrificial template. To increase the filling rate of FTO sol-gel precursors into their void areas, PS opals were first immersed in a methanol solution. Due to its low viscosity, methanol could fully occupy the void areas inside the FTO IOs. Under vacuum, methanol could be easily removed from the void areas and thus formed negative pressure in these areas, promoting the filling of the FTO sol-gel precursors.[42] Then, PS opals were removed by a calcination process and the FTO sol-gels in the void areas were converted into crystalline FTO IOs. Next, CdS NRs were grafted on their surface by a hydrothermal reaction. The chemical reaction is shown in equation (1).[43]

$$Cd(NO_3) + 2(NH_2)_2CS + H_2O \rightarrow CdS + H_2S \uparrow + 2HNO_3 + 2CO_2 \uparrow + 4NH_3 \uparrow \quad (1)$$

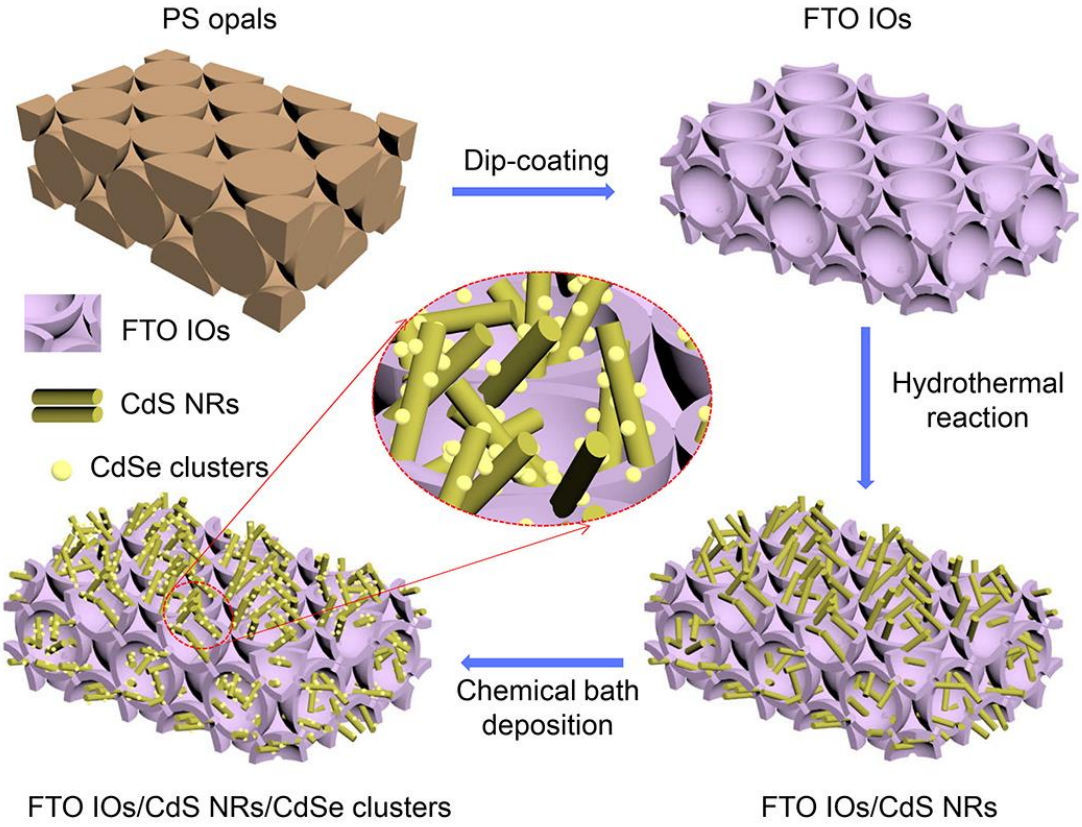

Figure 7.1 Schematic shown of the fabrication process of FTO IOs/CdS NRs/CdSe clusters.

The reaction between Cd^{2+} and thiourea formed the $Cd(NO_3)_2·x(NH_2)_2CS$ complex films, which deposited on the walls of FTO IOs and then decomposed into CdS nuclei layer at high temperature. CdS NRs were grown on the seed layer with glutathione-assisted orientation, forming the 3D FTO IOs/1D CdS NRs hierarchical nanostructures. CdSe clusters were then coated on the hierarchical nanostructures through the reaction of Cd^{2+} and $SeSO_3^{2-}$.

Figure 7.2 shows the scanning electron microscope (SEM) images of the product of each step. As shown in Figure 7.2(a), FTO IOs consist of periodic voids, which are separated by a circular wall. On each inner wall, three smaller holes can be observed where the PS opal spheres were previously adjoined, indicating the existence of multiple layers within the FTO IOs. The diameter of the PS microspheres used in the opal template was 870 nm.

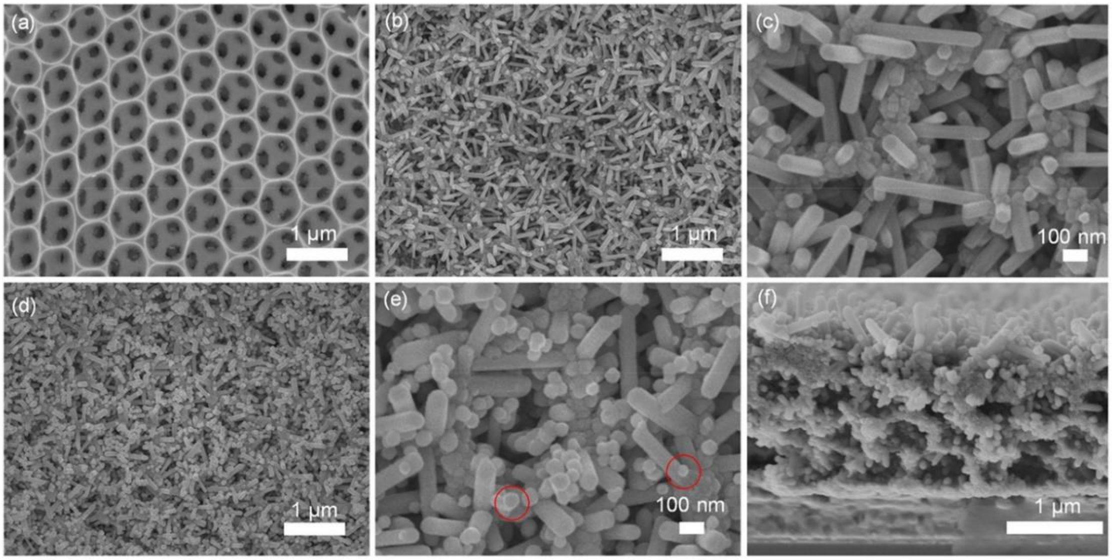

Figure 7.2 Top-view SEM images: (a) FTO IOs, (b)-(c) FTO IOs/CdS NRs; and (d)-(e) FTO IOs/CdS NRs/CdSe clusters; (f) Cross-section view SEM image of FTO IOs/CdS NRs/CdSe clusters.

Following the calcination, the average pore diameter of FTO IOs shrunk to approximately 700 nm, while the thickness of the newly formed wall between each pore increased to 20 nm. In the hydrothermal reaction, the FTO walls provided a surface for the deposition of numerous CdS nuclei, from which CdS NRs could be grown inside each FTO pore. The selection of PS microspheres with smaller diameters, such as 300 nm and 500 nm, would cause the formation of tree-like CdS nanostructures on the top surface of the FTO IOs, as shown in Figure 7.3. Thus, the PS microsphere diameter should be large enough to ensure the secondary growth of CdS NRs without disrupting the periodic FTO IOs structure. Figure 7.2(b) shows that despite the CdS NRs having grown over the FTO walls, the periodic structures of the FTO IOs are well maintained. The magnified image in Figure 7.2(c) further exhibits that the FTO walls are partially coated with short CdS nanocrystals and partially with longer CdS NRs, indicating the formation of FTO IOs/CdS NRs hierarchical nanostructures.

The length of these CdS NRs ranges from 100 nm to 400 nm, which is smaller than the pore diameter, leaving distinguishable space in each void. Our previous studies have

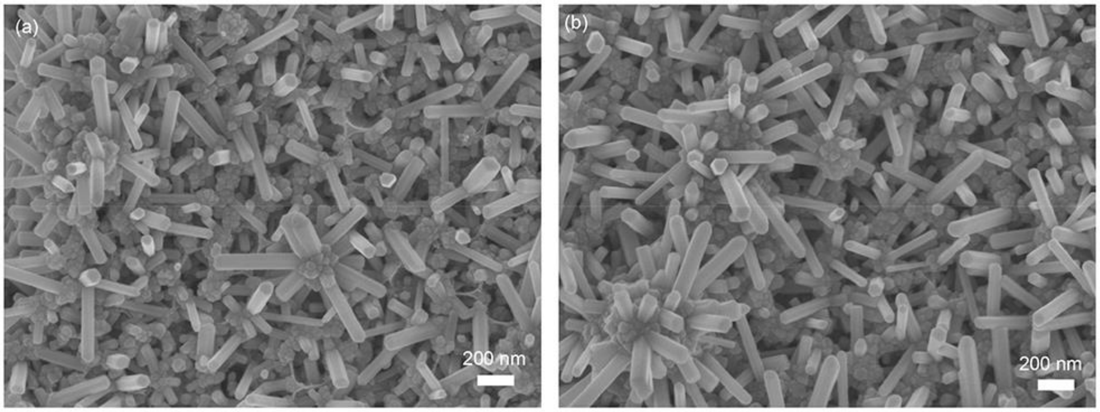

Figure 7.3 Top-view SEM images of FTO IOs/CdS NRs/CdSe clusters by using the different diameters of PS microspheres as the template: (a) 300 nm; (b) 500 nm.

proved that the small CdS nanocrystals can be transformed into longer CdS NRs with extended duration of the hydrothermal reaction.[44] However, the existence of only CdS NRs can cause all the void areas to be occupied, thus forming a thick film on the top surface of FTO IOs, which could hinder their light scattering capability. On the other hand, by having a co-existence of CdS NRs and CdS nanocrystals on FTO IOs, there will be the presence of unoccupied space, which is essential for light transmission and the formation of multiple light scattering within the nanostructures. Figures 7.2(d) and 7.2(e) are SEM images of FTO IOs/CdS NRs/CdSe clusters taken from the top-view. Figure 7.2(d) shows that the FTO IOs/CdS NRs hierarchical nanostructures have no obvious deformation after the coating of CdSe clusters. By comparing Figure 7.2(e) with Figure 7.2(c), it can be observed that some CdSe clusters are dispersed on top of both the small CdS nanocrystals and longer CdS NRs, as marked in red in Figure 7.2(e). Figure 7.2(f) is the cross-sectional view of the FTO IOs/CdS NRs/CdSe clusters. FTO IOs with a thickness of 2 μm are covered with CdS NRs and CdSe clusters from the top to the bottom layer, making it possible for CdS NRs and CdSe clusters to absorb the multiply scattered light within the hierarchical nanostructures. The digital images of the sample obtained in each step are shown in Figure 7.4. Except for some bare area used to connect the electrode, FTO glass is fully covered with the as-prepared nanostructures, indicating the formation of periodic nanostructures on a large scale. The color change also suggests the transition from

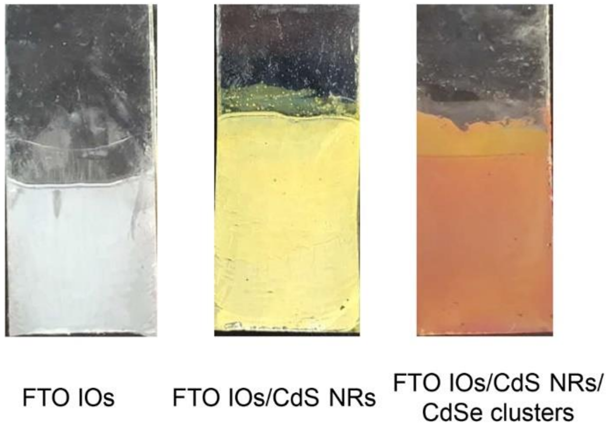

Figure 7.4 Digital images of FTO IOs, FTO IOs/CdS NRs, and FTO IOs/CdS NRs/CdSe clusters.

FTO IOs to FTO IOs/CdS NRs and FTO IOs/CdS NRs/CdSe clusters. The microstructure of the FTO IOs/CdS NRs/CdSe clusters was also characterized by TEM, as shown in **Figures 7.5**. Figure 7.5(a) clearly shows the TEM image of FTO IOs/CdS NRs/CdSe clusters, from which CdS NRs can be observed to surround the pore structure of FTO IOs. A high-resolution TEM image shown in Figure 7.5(b) further confirms the decoration of CdSe clusters on the surface of CdS NRs. The measured lattice of 0.34 nm and 0.35 nm correspond to the (002) plane of CdS and the (111) plane of CdSe, respectively.[20, 37] EDS elemental mapping was used to investigate the hierarchical structure of the FTO IOs/CdS NRs/CdSe clusters, and the results of Sn, Cd, S, and Se mapping are shown in Figures 7.5(c)-7.5(f), respectively. Sn elements are only distributed on the walls of FTO IOs, while the Cd, S, and Se elements are dispersed on both the walls and the voids of the FTO IOs. This mapping demonstrates that the CdS NRs were rooted in the walls of FTO IOs and gradually grew within the voids area of FTO IOs. The distribution of Se elements is similar to that of S and Sn elements, indicating that CdSe clusters were uniformly coated on the surface of FTO IOs/CdS NRs.

Figure 7.6(a) shows the XRD patterns of FTO IOs, FTO IOs/CdS NRs, and FTO IOs/CdS NRs/CdSe clusters. FTO IOs show four main peaks, as marked on the blue curve, referring to the rutile phase of SnO_2. After the growth of CdS NRs, some new peaks, as marked on

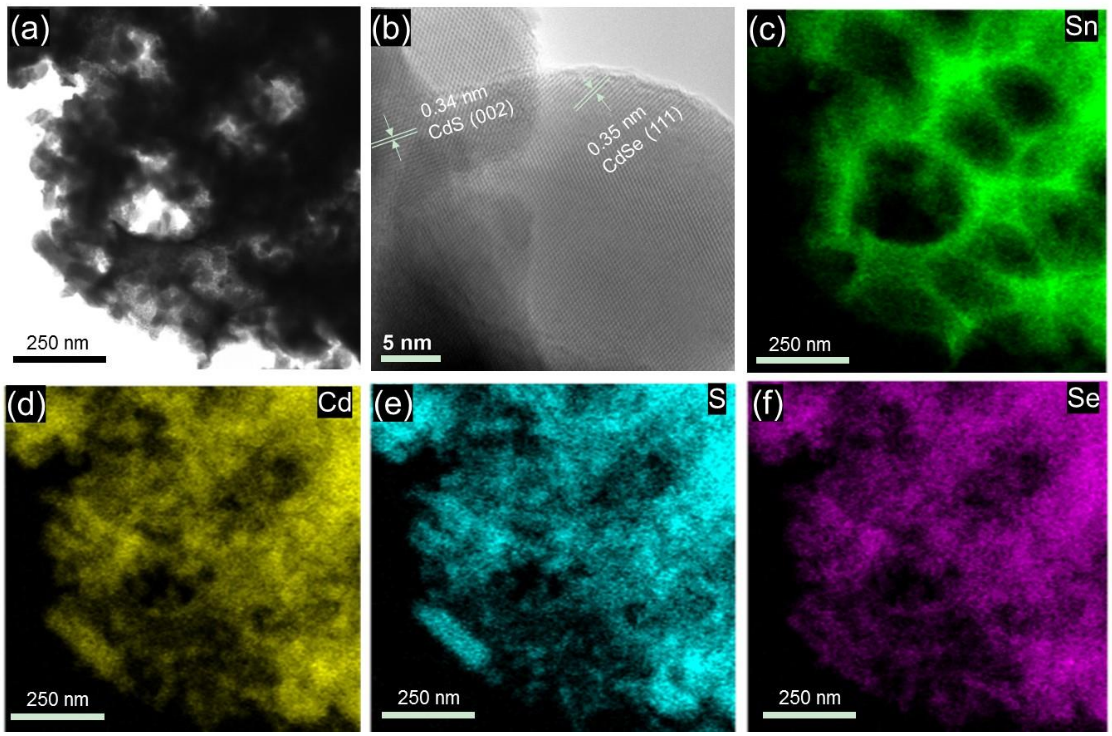

Figure 7.5 (a) TEM image of FTO IOs/CdS NRs/CdSe clusters; (b) HRTEM image of FTO IOs/CdS NRs/CdSe clusters; (c)-(f) EDS mapping of FTO IOs/CdS NRs/CdSe clusters.

the red curve, can be observed, corresponding to the wurtzite phase of CdS. The black curve shows the XRD patterns of FTO IOs/CdS NRs/CdSe clusters. The new peaks at 25.3°, 42.2°, and 49.7° correspond to the (111), (220), and (311) planes of cubic CdSe.[45] Thus, the peaks corresponding to SnO_2, CdS, and CdSe can be simultaneously distinguished. XPS was then conducted to analyze the composition and surface chemical state of FTO IOs/CdS NRs/CdSe clusters. Figures 3(b)-3(d) present the high-resolution XPS spectra of Cd, S, and Se. Figure 3(b) shows that the binding energies at 405.14 eV and 411.88 eV can be indexed to Cd $3d_{5/2}$ and Cd $3d_{3/2}$. In Figure 3(c), the binding energy at 161.09 eV and 162.35 eV correspond to $S2p_{3/2}$ while the peaks at 162.5 eV and 163.61 eV can be associated with $S2p_{1/2}$. Besides, the peak at ~167 eV can be assigned to oxidized sulfur moieties on the surface.[46] Figure 3(d) shows the binding energies at Se $3d_{5/2}$ (53.96 eV), Se $3d_{3/2}$ (54.82 eV), which could be assigned to Cd-Se bonds.[34] Both XRD and XPS results attest that FTO IOs/CdS NRs/CdSe clusters with high purity had been successfully fabricated.

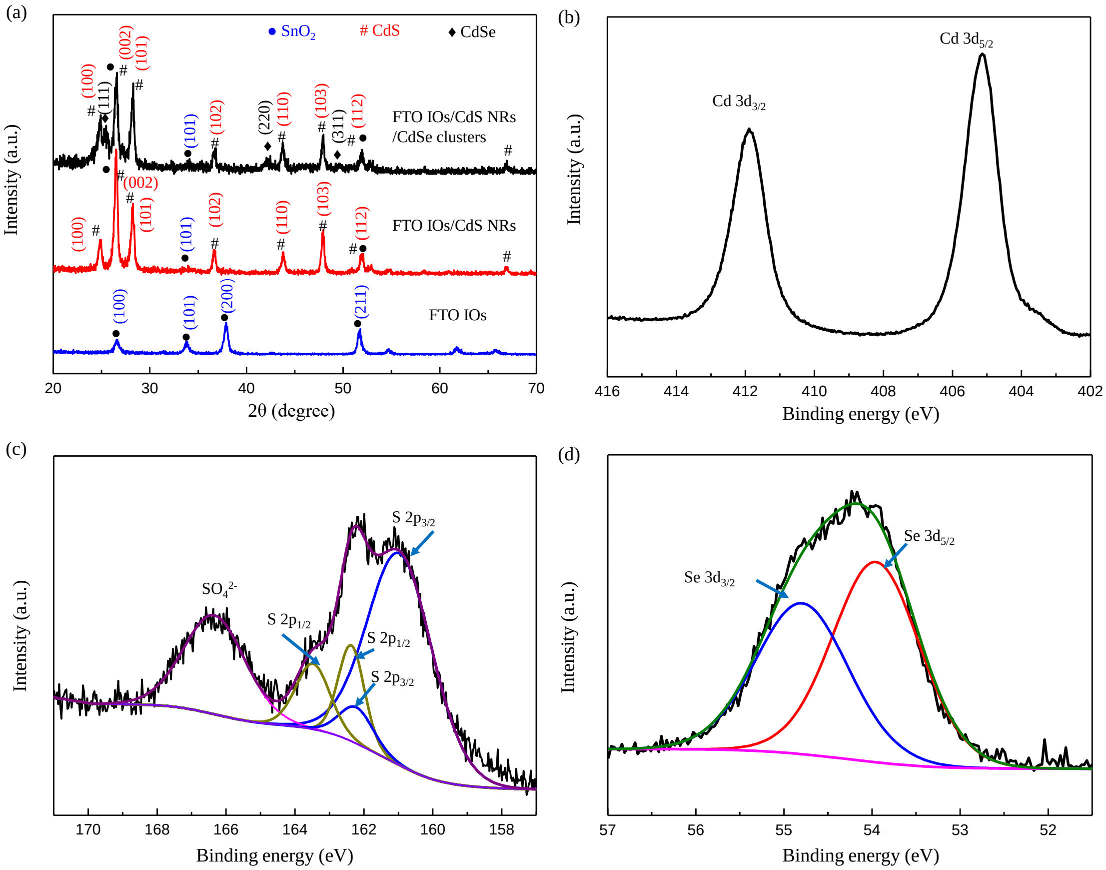

Figure 7.6 (a) XRD patterns of the as-prepared samples. High resolution XPS spectrum of FTO IOs/CdS NRs/CdSe clusters: (b) Cd 3d, (c) S 2p, and (d) Se 3d.

As a 3D porous structure, FTO IOs can provide high surface area for the loading of visible light sensitizers.[47] Thus, the electrochemical active surface area (ECSA) of FTO IOs/CdS NRs/CdSe clusters and pristine CdS NRs/CdSe clusters were examined. As shown in equation (2) and (3), the ECSA is proportional to the electrochemical double-layer capacitance (C_{dl}), which can be obtained from the cyclic voltammetry scans.[48]

$$ECSA = \frac{C_{dl}}{C_s} \qquad (2)$$

$$I_c = v * C_{dl} \qquad (3)$$

C_s is the intrinsic specific capacitance. I_c is the capacitive current and v is the scan rate.

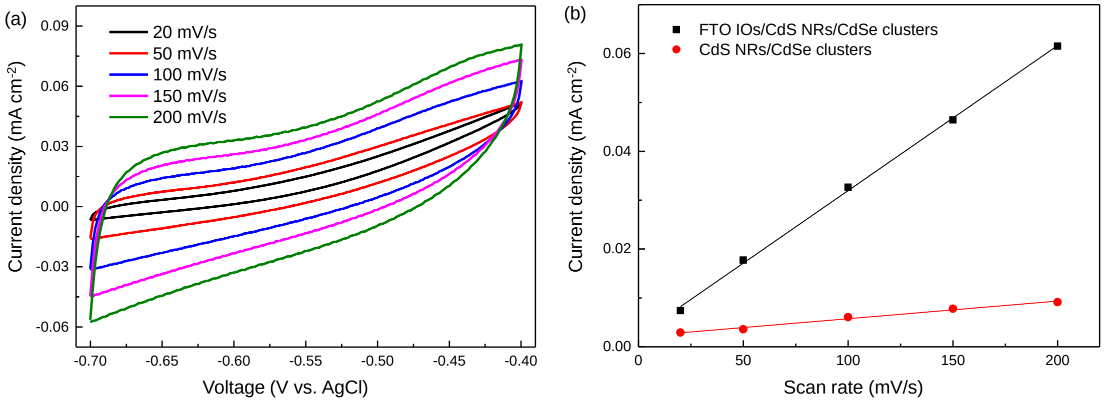

Figure 7.7 (a) The capacitive currents of the FTO IOs/CdS NRs/CdSe clusters under different scan rates. (b) The linear relationship between the capacitive currents and the scan rate.

Figure 7.7a shows the capacitive currents of FTO IOs/CdS NRs/CdSe clusters with different scan rates under the dark condition with the Na_2S and Na_2SO_3 mixed solution as the electrolyte. The difference between capacitive currents at -0.55 V under different scan rates was calculated and compared in Figure 7.7(b). The C_{dl} of FTO IOs/CdS NRs/CdSe clusters and CdS NRs/CdSe clusters is 0.297 mF cm^{-2} and 0.0361 mF cm^{-2} respectively, thus, the ECSA of FTO IOs/CdS NRs/CdSe clusters is 8.2 times higher than that of pristine CdS NRs/CdSe clusters. This enlarged ECSA indicates that FTO IOs/CdS NRs/CdSe clusters can provide higher active sites for surface reactions and lower surface interface resistance.

To examine the impact of FTO IOs on the light absorption of hierarchical nanostructures, the optical performance of the FTO IOs/CdS NRs/CdSe clusters and pristine CdS NRs/CdSe clusters were examined and compared in Figure 7.8. Figure 7.8(a) shows that the FTO IOs/CdS NRs/CdSe clusters exhibit considerably higher reflectance than the CdS NRs/CdSe clusters when the incident light wavelength exceeds 700 nm. The comparatively higher diffuse reflectance reveals the enhanced light scattering ability of FTO IOs/CdS NRs/CdSe clusters, which can be ascribed to the periodic structure of FTO IOs and the surrounded CdS NRs. Figure 7.8(b) shows the comparison of the transmittance spectra of FTO IOs/CdS NRs/CdSe clusters and pristine CdS NRs/CdSe clusters. FTO IOs/CdS NRs/CdSe clusters have a lower transmittance than pristine CdS NRs/CdSe clusters when

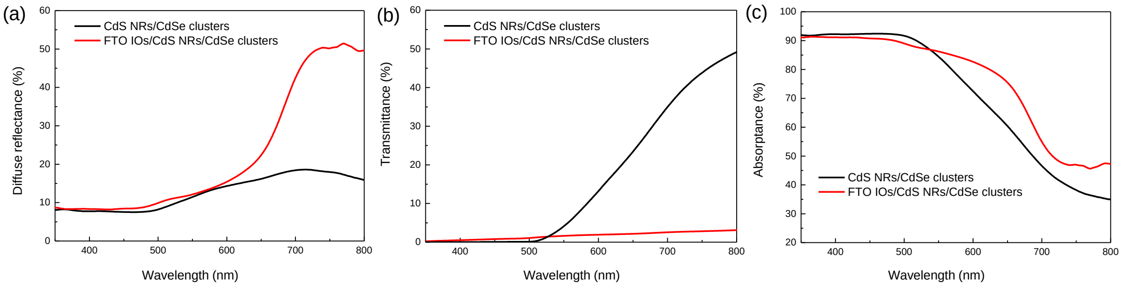

Figure 7.8 The optical performance of the FTO IOs/CdS NRs/CdSe clusters and CdS NRs/CdSe clusters: (a) diffuse reflectance spectra; (b) transmittance spectra; and (c) absorptance spectra.

the incident light wavelength exceeds 520 nm. The absorptance spectra can be calculated by the following equation (4).

$$Absorptance(\%) = 100\% - transmittance(\%) - reflection\ (\%) \qquad (4)$$

As shown in Figure 7.8(c), FTO IOs/CdS NRs/CdSe clusters have higher light absorption than pristine CdS NRs/CdSe clusters in the range of 550-700 nm. This enhancement can be illustrated by the enhanced scattering ability and enlarged specific surface area of FTO IOs/CdS NRs/CdSe clusters hierarchical nanostructures. Compared to the CdS NRs/CdSe clusters grown on the flat FTO substrate, the incident light penetrated the FTO IOs/CdS NRs/CdSe clusters would be scattered by the periodic walls of FTO IOs and the surrounded CdS NRs. The uniform structure of FTO IOs enabled even light scattering while the CdS NRs brought about addition random light scattering, thus prolonging the optical length and enhancing the light absorption of CdS and CdSe. The enlarged specific surface area of the hierarchical structure also contributed to the higher loading of CdSe clusters, which further increased the visible light absorption.

7.3.2 PEC performance

The PEC performance was evaluated by testing linear sweep curves with front-side illumination using Na_2S/Na_2SO_3 mix solution as the electrolyte. As photocurrent is induced by the transfer of photo-induced electrons from photoanode to the counter electrode, it can be used to compare the PEC performance of different photoanodes.[1] Na_2S/Na_2SO_3 mix

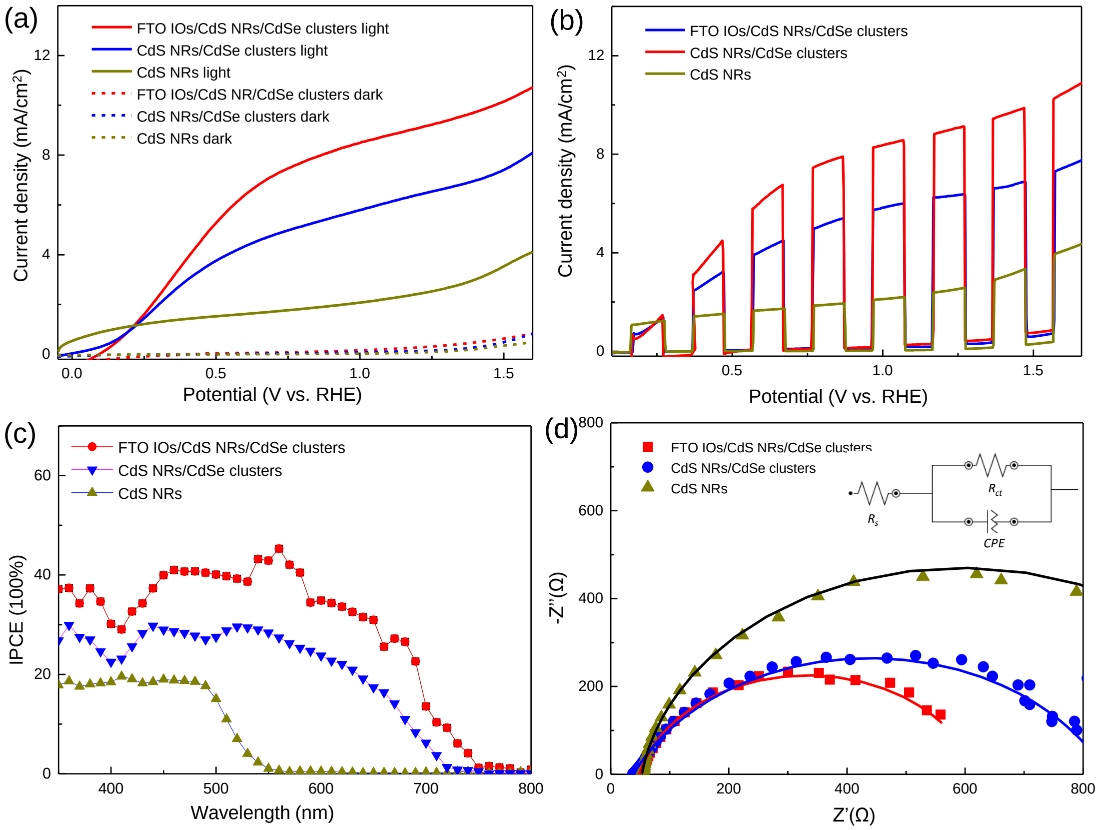

Figure 7.9 (a) Linear sweep curves of FTO IOs, FTO IOs/CdS NRs, and FTO IOs/CdS NRs/CdSe clusters; (b) Linear sweep curves of FTO IOs, FTO IOs/CdS NRs, and FTO IOs/CdS NRs/CdSe clusters with the light on/off cycles; (c) IPCE of FTO IOs, FTO IOs/CdS NRs, and FTO IOs/CdS NRs/CdSe clusters; (d) EIS Nyquist plots of FTO IOs, FTO IOs/CdS NRs, and FTO IOs/CdS NRs/CdSe clusters. Inset in (d) shows the equivalent circuit.

solution act as an efficient hole scavenger can achieve a high surface charge transfer efficiency (100%), which allows an investigation into the contribution of the hierarchical structures on charge generation and charge transport. As shown in Figure 7.9(a), the photocurrent density of pristine CdS NRs at 1.23 V versus reversible hydrogen electrode (RHE) is 2.4 mA cm^{-2}. After loading the CdSe clusters, the photocurrent increased to 6.4 mA cm^{-2} at 1.23 V versus RHE, which can be attributed to the extended visible light absorption range due to the lower bandgap of CdSe as well as the heterojunction formed between CdS and CdSe. The combination of host FTO IOs with guest CdS NRs/CdSe clusters further increased the photocurrent to 9.2 mA cm^{-2} at the same applied voltage. As

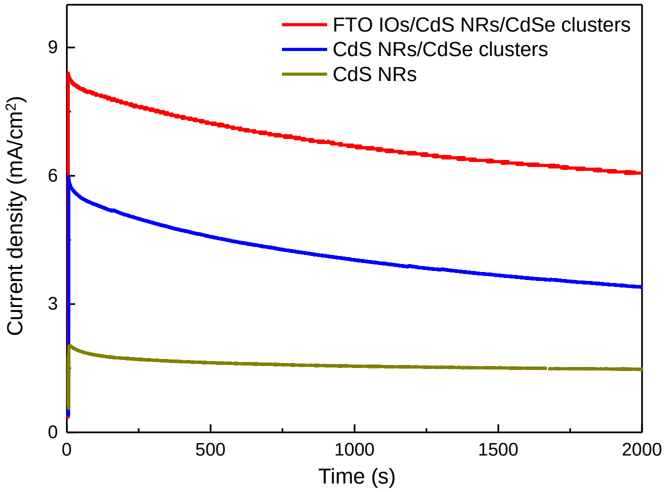

Figure 7.10 The photostability measurements of FTO IOs/CdS NRs/CdSe clusters, CdS NRs/CdSe clusters, and CdS NRs.

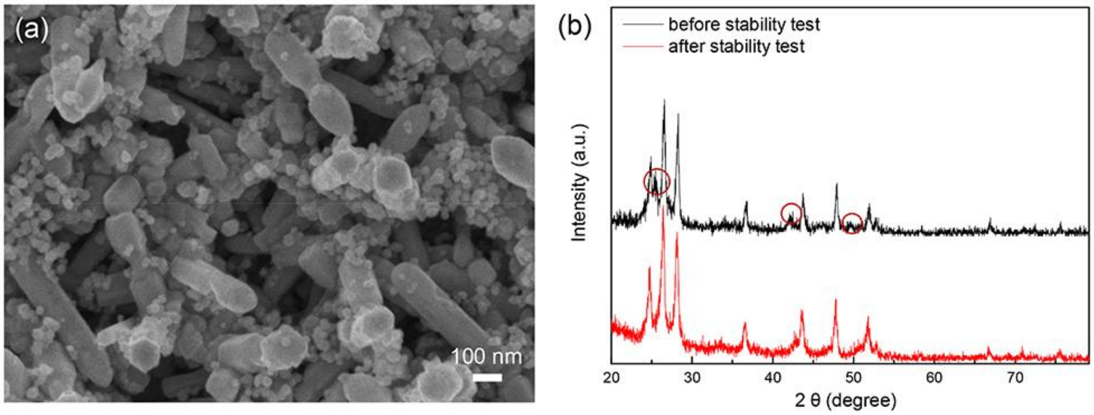

Figure 7.11 (a) Top-view SEM images of FTO IOs/CdS NRs/CdSe clusters after the photostability test; (b) XRD patterns of FTO IOs/CdS NRs/CdSe clusters after photostability test.

reflected by the UV measurement, the introduction of FTO IOs increased the light absorption of CdS and CdSe, producing more electron-hole pairs. Furthermore, the FTO IOs with high electron mobility could accelerate charge transport from the CdSe and CdS to the counter electrode for hydrogen evolution. Figure 7.9(a) also shows that the dark current of these photoanodes is negligible at 1.23 V versus RHE, thus confirming that photocurrent was induced by light illumination. Figure 7.9(b) further shows the results of the linear sweep curves with light ON/OFF cycles. The fast change between photocurrent and dark current demonstrates the high light response of these photoanodes. Besides, the current of FTO IOs/CdS NRs/CdSe clusters with the light on is higher than that of pristine CdS NRs/CdSe clusters and CdS NRs, which complies with results shown in Figure 7.9(a). The stability of the as-prepared samples had also been examined by applying a constant voltage of 1 V versus RHE, as shown in Figure 7.10. The photocurrent of the FTO IOs/CdS NRs/CdSe clusters and CdS NRs/CdSe clusters decreased gradually from 8.2 mA cm^{-2} to 6.7 mA cm^{-2} and 5.8 mA cm^{-2} to 3.4 mA cm^{-2} respectively in 2000 s testing, while photocurrent of the CdS NRs only decreased from 2.1 mA cm^{-2} to 1.5 mA cm^{-2}, showing a better photostability. XRD and SEM measurements of FTO IOs/CdS NRs/CdSe clusters were performed after the photostability test, as shown in Figure 7.11. The morphology did not show any obvious changes, and the periodic structure was kept. The XRD results also showed that the peaks of CdS remained unchanged. However, some peaks of CdSe were diminished, indicating that CdSe was not stable during the PEC test, which could be ascribed to the loss of Se element. [49]

Furthermore, IPCE spectra of FTO IOs/CdS NRs/CdSe clusters, pristine CdS NRs/CdSe clusters, and CdS NRs were measured and shown in Figure 7.9(c). FTO IOs/CdS NRs/CdSe clusters showed higher IPCE maximum (49%) compared to CdS NRs/CdSe clusters (30%) and CdS NRs (20%). Compared to CdS NRs, CdS NRs/CdSe clusters showed an extended light response range due to the lower bandgap of CdSe. The higher IPCE of FTO IOs/CdS NRs/CdSe clusters than CdS NRs/CdSe clusters proves the vital role of FTO IOs, which could improve light-harvesting efficiency and increase charge collection ability.

To further investigate the impact of FTO IOs on the electron recombination kinetics of CdS and CdSe, Open circuit voltage (V_{oc}) decay (OCVD) was measured to extract decay lifetime (τ) of the accumulated electrons. When a photoanode is under open circuit condition and constant illumination, the loss and generation of electrons would form an equilibrium. After shutting down the light, the voltage would decay with time due to the recombination between the electrons and holes.[50] Figure 7.12(a) shows the OCVD curves of FTO IOs/CdS NRs/CdSe clusters and pristine CdS NRs/CdSe clusters. τ can be

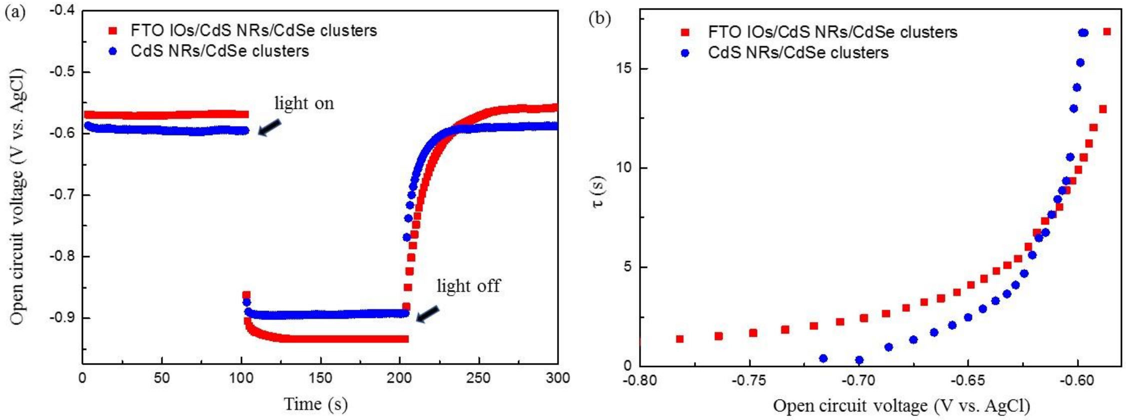

Figure 7.12 (a) OCVD measurements of FTO IOs/CdS NRs/CdSe clusters and CdS NRs/CdSe clusters. (b) The decay lifetime at different potentials.

calculated from equation (5).[51]

$$\tau = -\left(\frac{K_B T}{e}\right)\left(\frac{dV_{oc}}{dt}\right)^{-1} \qquad (5)$$

K_BT is the thermal energy and e is the charge of an electron. Figure 7.12(b) shows that FTO IOs/CdS NRs/CdSe clusters have a longer τ than pristine CdS NRs/CdSe clusters at the same V_{oc}, indicating that the introduction of FTO IOs can suppress the charge recombination.

EIS under light illumination was conducted to analyze the charge transfer resistance. The charge transfer resistance at the interface between the photoanode and electrolyte could be determined through the diameter of the middle frequency (1-10^5 Hz) semicircle shown in the Nyquist plots.[52] As shown in Figure 7.9(d), the resistance of the FTO IOs/CdS NRs/CdSe clusters is smaller than that of the pristine CdS NRs/CdSe clusters and CdS NRs, which could be due to the increased active surface area, faster collection of charge carriers, and accelerated electron-hole separation. The equivalent circuit utilized in the fitting of EIS data is presented in Figure 7.9(d). R_s and R_{ct} represent the series resistance and the charge transfer resistance at the electrode-electrolyte interface, respectively. The fitting results show that that the R_s value of FTO IOs/CdS NRs/CdSe clusters (51.2 **Ω**) was comparable to that of CdS NRs/CdSe clusters (31.8 **Ω**) and CdS NRs (42.5 **Ω**), while the

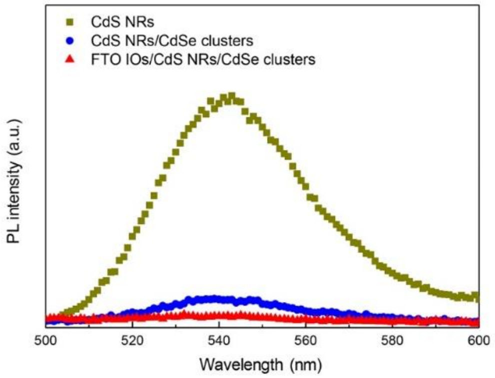

Figure 7.13 PL spectra of FTO IOs/CdS NRs/CdSe clusters, CdS NRs/CdSe clusters and CdS NRs.

R_{ct} value of FTO IOs/CdS NRs/CdSe clusters (566.9 Ω) was smaller than that of the CdS NRs/CdSe clusters (924 Ω) and CdS NRs (1120 Ω), indicating that the FTO IOs/CdS NRs/CdSe clusters could facilitate charge transportation and separation.

The photoluminescence (PL) spectra of the FTO IOs/CdS NRs/CdSe clusters, CdS NRs/CdSe clusters and CdS NRs were measured to further investigate the function of heterojunction formation and the introduction of FTO IOs, as shown in Figure 7.13. The PL intensity of CdS NRs/CdSe clusters was lower than that of CdS NRs, which could be explained by the enhanced PL quenching due to the formation of heterojunction between CdS and CdSe. The introduction of FTO IOs further decreased the PL intensity owing to the enhanced charge transfer in the FTO IOs/CdS NRs/CdSe clusters.[53] This result is consistent with the EIS measurements.

Mott-Schottky measurements were performed in 0.5 M Na_2SO_4 solution under the dark condition to investigate the impact of FTO IOs on the flat band potential (E_{fb}) of CdS/CdSe. E_{fb} can be acquired by the following equation (6).[54]

$$\frac{1}{C^2} = \frac{2}{q\varepsilon\varepsilon_0 N_d} \times \left(E - E_{fb} - \frac{kT}{e}\right) \qquad (6)$$

Where N_d, q, ε, and ε_0 are the carrier density, charge of an electron, dielectric constant of the semiconductor, and dielectric constant of the vacuum permittivity, respectively. E is

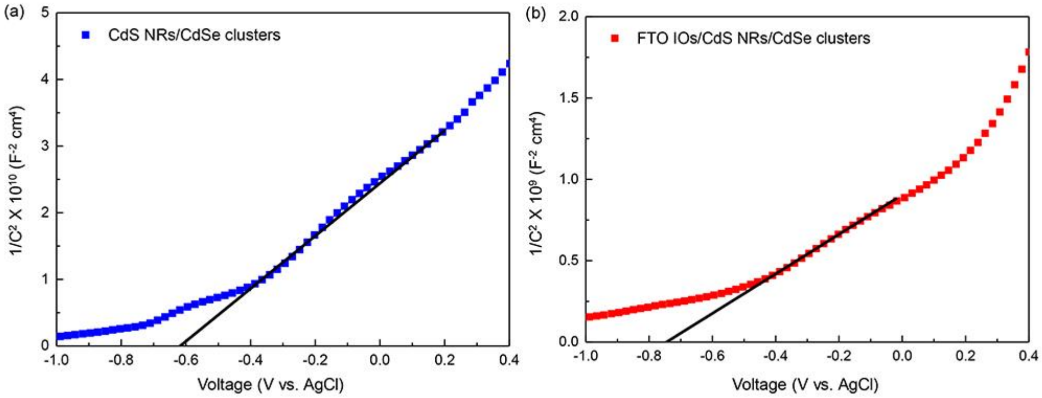

Figure 7.14. Mott-Schottky plots of (a) CdS NRs/CdSe clusters; (b) FTO IOs/CdS NRs/CdSe clusters.

the applied voltage. Figure 7.14(a) and 7.14(b) show the Mott-Schottky plots of CdS NRs/CdSe clusters and FTO IOs/CdS NRs/CdSe clusters. E_{fb} can be determined by the X-intercepts of the linear region. As shown in Figure 7.13, V_{fb} of CdS NRs/CdSe clusters and FTO IOs/CdS NRs/CdSe clusters are -0.62 V and -0.73 V respectively. The negative shift of V_{fb} indicates that FTO IOs/CdS NRs/CdSe clusters could support a better charge separation.[55] Besides, N_d is inversely proportional to the slope of the linear region. The N_d of FTO IOs/CdS NRs/CdSe clusters is 32 times higher than that of CdS NRs/CdSe clusters. The increase of carrier density can be ascribed to the introduction of conductive FTO IOs as the host skeleton, which could contribute to the charge transport during the PEC process.[23]

The PEC water splitting process of FTO IOs/CdS NRs/CdSe clusters is schematically illustrated in **Figure 7.15** based on the experimental results. Under the illumination, the incident light is split into evenly scattered light from the FTO IOs and the randomly scattered light from the CdS NRs within the hierarchical structures. The multi-scattering phenomenon enables light to be absorbed more effectively by the CdS NRs and CdSe clusters, thus enhancing their light-harvesting efficiency. The high specific surface offered by the hierarchical structures also increases the contact area with electrolyte, leading to a more efficient redox reaction. Besides, the optimal band alignment between CdS and CdSe increases the charge separation efficiency, allowing electrons to move from the higher

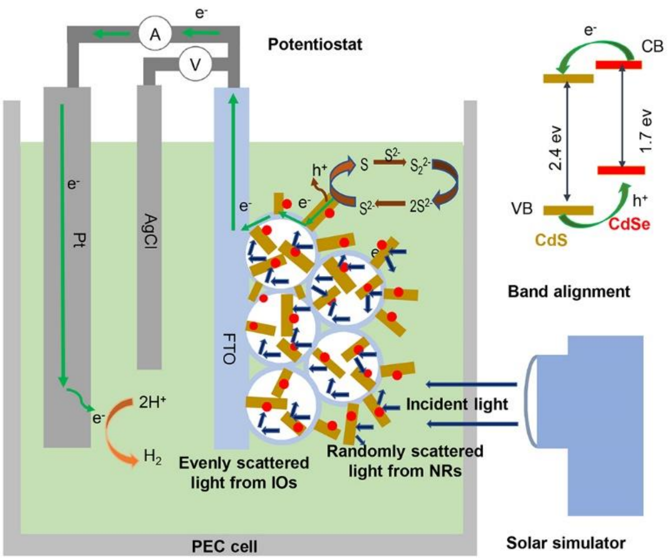

Figure 7.15 PEC water splitting process of FTO IOs/CdS NRs/CdSe clusters and the band alignment between CdS and CdSe.

conduction band of CdSe to lower conduction band of CdS while the holes move in the opposite direction and finally reach the semiconductor/electrolyte interface for sulfur oxidation. Furthermore, due to the high electrical conductivity, FTO IOs can accelerate the transport of electrons from CdSe and CdS to the Pt counter electrode for hydrogen evolution.

7.4 Conclusion

In summary, 3D periodic FTO IOs/1D CdS NRs coated with CdSe clusters as a hierarchical photoanode for efficient PEC water splitting is reported. It has accomplished an improved PEC performance as compared to CdS NRs/CdSe cluster and CdS NRs grown on bare FTO glass. The hierarchical nanostructures, which brought about multiple light scattering as reflected by the UV measurement, greatly enhanced their performance in PEC water splitting. The enhanced charge separation and transport indicated by the EIS testing, OCVD measurements, and PL spectra could be attributed to the CdS/CdSe heterojunction and the high electrical conductivity of FTO IOs. This work demonstrates that the combination of conductive 3D FTO IOs with other dimensional photoactive nanomaterials is a valid route to incorporate various enhancement strategies in one hierarchical nanostructure for the development of efficient host-guest photoanodes.

References

[1] X.T. Xu, L. Pan, X. Zhang, L. Wang, J.J. Zou, *Adv. Sci.* **2019**, *6*, 1801505.

[2] W. Yang, J. Moon, *ChemSusChem* **2018**, *12*, 1189.

[3] B. Chen, Z. Zhang, M. Baek, S. Kim, W. Kim, K. Yong, *Appl. Catal. B: Environ.* **2018**, *237*, 763.

[4] N. Karjule, R. Phatake, M. Volokh, I. Hod, M. Shalom, *Small Methods* **2019**, 1900401.

[5] H. Wu, H.N. Alshareef, T. Zhu, *InfoMat* **2019**, *1*, 417.

[6] S.-Y. Chen, J.-S. Yang, J.-J. Wu, *ACS Appl. Energy Mater.* **2018**, *1*, 2143.

[7] Z. Luo, T. Wang, J. Zhang, C. Li, H. Li, J. Gong, *Angew. Chem. Int. Ed.* **2017**, *56*, 12878.

[8] W. Wang, J. Dong, X. Ye, Y. Li, Y. Ma, L. Qi, *Small* **2016**, *12*, 1469.

[9] J.-H. Kim, D.H. Kim, J.W. Yoon, Z. Dai, J.-H. Lee, *ACS Appl. Energy Mater.* **2019**, *2*, 4535.

[10] R. Tang, S. Zhou, Z. Yuan, L. Yin, *Adv. Funct. Mater.* **2017,** *27*, 1701102.

[11] B. Zhang, L. Wang, Y. Zhang, Y. Ding, Y. Bi, *Angew. Chem. Int. Ed.* **2018**, *57*, 2248.

[12] R. Wang, L. Wang, Y. Zhou, Z. Zou, *Appl. Catal. B: Environ.* **2019**, *255*, 117738.

[13] Y. Hou, X. Zhuang, X. Feng, *Small Methods* **2017**, *1*, 1700090.

[14] C. Li, Z. Luo, T. Wang, J. Gong, *Adv. Mater.* **2018**, *30*, 1707502.

[15] B.R. Lee, M.G. Lee, H. Park, T.H. Lee, S.A. Lee, S.S.M. Bhat, C. Kim, S. Lee, H.W. Jang, *ACS Appl. Mater. Interfaces* **2019**, *11*, 20004.

[16] Q. Nie, L. Yang, C. Cao, Y. Zeng, G. Wang, C. Wang, S. Lin, *Chem. Eng. J.* **2017**, *325*, 151.

[17] B. Xu, P. He, H. Liu, P. Wang, G. Zhou, X. Wang, *Angew. Chem. Int. Ed.* **2014**, *53*, 2339.

[18] K. Yuan, Q. Cao, H.-L. Lu, M. Zhong, X. Zheng, H.-Y. Chen, T. Wang, J.-J. Delaunay, W. Luo, L. Zhang, Y.-Y. Wang, Y. Deng, S.-J. Ding, D.W. Zhang, *J. Mater. Chem. A* **2017**, *5*, 14697.

[19] M. Curti, J. Schneider, D.W. Bahnemann, C.B. Mendive, *J. Phys. Chem. Lett.* **2015**, *6*, 3903.

[20] W. Wang, C. Jin, L. Qi, *Small* **2018**, *14*,1801352.

[21] S.K. Karuturi, C. Cheng, L. Liu, L. Tat Su, H.J. Fan, A.I.Y. Tok, *Nano Energy* **2012**, *1*, 322.

[22] Y. Wang, W. Tian, L. Chen, F. Cao, J. Guo, L. Li, *ACS Appl. Mater. Interfaces* **2017**, *9*, 40235.

[23] Z. Zhang, C. Gao, Y. Li, W. Han, W. Fu, Y. He, E. Xie, *Nano Energy* **2016**, *30*, 892.

[24] I. Kondofersky, H.K. Dunn, A. Muller, B. Mandlmeier, J.M. Feckl, D. Fattakhova-Rohlfing, C. Scheu, L.M. Peter, T. Bein, D. Fattakhova-Rohlfing, C. Scheu, L. M. Peter, T. Bein, *ACS Appl. Mater. Interfaces* **2015**, *7*, 4623.

[25] L. Zhou, C. Zhao, B. Giri, P. Allen, X. Xu, H. Joshi, Y. Fan, L.V. Titova, P.M. Rao, *Nano Lett.* **2016**, *16*, 3463.

[26] Y. Sun, W.D. Chemelewski, S.P. Berglund, C. Li, H. He, G. Shi, C.B. Mullins, *ACS Appl. Mater. Interfaces* **2014**, *6*, 5494.

[27] Q. Peng, B. Kalanyan, P.G. Hoertz, A. Miller, D.H. Kim, K. Hanson, L. Alibabaei, J. Liu, T.J. Meyer, G.N. Parsons, J.T. Glass, *Nano Lett.* **2013**, *13,* 1481.

[28] Y. Sun, W.D. Chemelewski, S.P. Berglund, C. Li, H. He, G. Shi, C.B. Mullins, *ACS Appl. Mater. Interfaces* **2014**, *6*, 5494.

[29] Y. Gun, G.Y. Song, V.H. Quy, J. Heo, H. Lee, K.S. Ahn, S.H. Kang, *ACS Appl. Mater. Interfaces* **2015**, *7*, 20292.

[30] Z. Wang, X. Li, H. Ling, C.K. Tan, L.P. Yeo, A.C. Grimsdale, A.I.Y. Tok, *Small* **2018**, *14*, 1800395.

[31] H. Zhang, C. Cheng, *ACS Energy Lett.* **2017**, *2*, 813.

[32] N.D. Quang, T.T. Hien, N.D. Chinh, D. Kim, C. Kim, D. Kim, *Electrochim. Acta* **2019**, *295*, 710.

[33] T. Wang, Y. Chai, D. Ma, W. Chen, W. Zheng, S. Huang, *Nano Research* **2017**, *10*, 2699.

[34] C. Li, H. Zhang, C. Cheng, *RSC Adv.* **2016**, *6*, 37407.

[35] Z. Wang, X. Li, C.K. Tan, C. Qian, A.C. Grimsdale, A.I.Y. Tok, *Appl. Surf. Sci.* **2019**, *470*, 800.

[36] Y.-S. Chang, M. Choi, M. Baek, P.-Y. Hsieh, K. Yong, Y.-J. Hsu, *Appl. Catal. B: Environ.* **2018**, *225*, 379.

[37] P. Wang, Y. Zhang, L. Su, W. Gao, B. Zhang, H. Chu, Y. Wang, J. Zhao, W.W. Yu, *Electrochim. Acta* **2015**, *165*, 110.

[38] Y.-S. Chang, M. Choi, M. Baek, P.-Y. Hsieh, K. Yong, Y.-J. Hsu, *Appl. Catal. B: Environ.* **2018**, *225*, 379.

[39] P.Y. Kuang, Y.Z. Su, K. Xiao, Z.Q. Liu, N. Li, H.J. Wang, J. Zhang, *ACS Appl. Mater. Interfaces* **2015**, *7*, 16387.

[40] L. Wang, W. Wang, Y. Chen, L. Yao, X. Zhao, H. Shi, M. Cao, Y. Liang, *ACS Appl. Mater. Interfaces* **2018**, *10*, 11652.

[41] M. Wang, J. Jiang, J. Shi, L. Guo, *ACS Appl. Mater. Interfaces* **2013**, *5*, 4021.

[42] X. Chen, Z. Li, J. Ye, Z. Zou, *Chem. Mater.* **2010**, *22*, 3583.

[43] Y. Liu, Y.-X. Yu, W.-D. Zhang, *J. Alloys Compd.* **2013**, *569*, 102.

[44] Z. Wang, G. Yang, C.K. Tan, T.D. Nguyen, A.I.Y. Tok, *Appl. Surf. Sci.* **2019**, *490*, 411.

[45] T.S. Shyju, S. Anandhi, R. Indirajith, R. Gopalakrishnan, *J. Alloys Compd.* **2010**, *506*, 892.

[46] L. Li, W. Fang, P. Zhang, J. Bi, Y. He, J. Wang, W. Su, *J. Mater. Chem. A* **2016**, *4*, 12402.

[47] T. Ling, S.A. Kulinich, Z.-L. Zhu, S.-Z. Qiao, X.-W. Du, *Adv. Funct. Mater*. **2014**, *24*, 707.

[48] X. Feng, Y. Chen, Z. Qin, M. Wang, L. Guo, *ACS Appl. Mater. Interfaces* **2016**, *8*, 18089.

[49] L. Wang, J. Han, Y. Wu, Y. Zhang, Q. Zhang, X. Tan, Y. Yang, W. Li, Y. Bu, J.-P. Ao, *Chem. Eng. J.* **2019**, *368*, 710.

[50] C.-Y. Cho, J. Lee, D.C. Lee, J.H. Moon, *Electrochim. Acta* **2015**, *166*, 350.

[51] Z. Zhang, L. Zhang, B. Chen, M. Baek, K. Yong, *ACS Sustain. Chem*. Eng. **2018**, *6*, 13462.

[52] F. Ning, M. Shao, S. Xu, Y. Fu, R. Zhang, M. Wei, D.G. Evans, X. Duan, *Energy Environ. Sci.* **2016**, *9*, 2633.

[53] J. Yang, C. Bao, T. Yu, Y. Hu, W. Luo, W. Zhu, G. Fu, Z. Li, H. Gao, F. Li, Z. Zou,

ACS Appl. Mater. Interfaces **2015**, *7*, 26482.

[54] S. Zhou, R. Tang, L. Zhang, L. Yin, *Electrochim. Acta*, **2017**, *248*, 593.

[55] F. Zhan, J. Li, W. Li, Y. Yang, W. Liu, Y. Li, *J. Power Sources* **2016**, *325*, 591.

Chapter 8

Conclusion and Future Work

This chapter provides a summary of the research results presented in the previous chapters. A series of hierarchical nanostructures have been prepared. The relationship between surface area and light penetration, multiple light scattering, and charge separation has been investigated and discussed. Finally, future work ideas are proposed based on the outcomes of the thesis.

8.1 Summary and Conclusion

As shown in Figure 8.1, a series of hierarchical nanostructures, including 2D/0D SnO_2 NSs/TiO_2/CdS QDs, 2D/1D WO_3 NSs/CdS NRs/TiO_2, 3D/0D FTO IOs/SnO_2 NCs/TiO_2, and 3D/1D FTO IOs/CdS NRs/CdSe clusters, have been fabricated. Different targeted strategies were incorporated in these hierarchical nanostructures. Through optimizing these targeted strategies, enhanced PEC performances were observed.

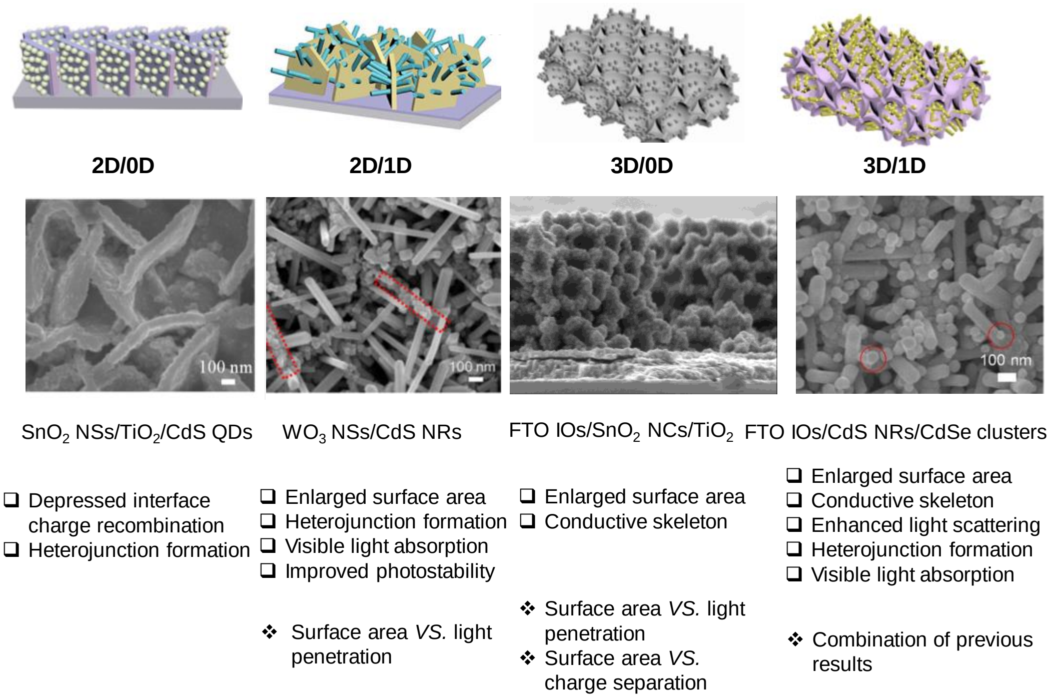

Figure 8.1 Schematic shown of the hierarchical nanostructures presented in the thesis and the corresponding targeted strategies incorporated in them.

8.1.1 Dual role of TiO_2 in SnO_2 NSs/TiO_2/CdS QDs

In the 2D/0D SnO_2 NSs/TiO_2/CdS QDs hierarchical nanostructure, a TiO_2 thin film was introduced between SnO_2 NSs and CdS QDs, which can simultaneously achieve the insulation of bare FTO substrate with electrolyte and the heterojunction formation between

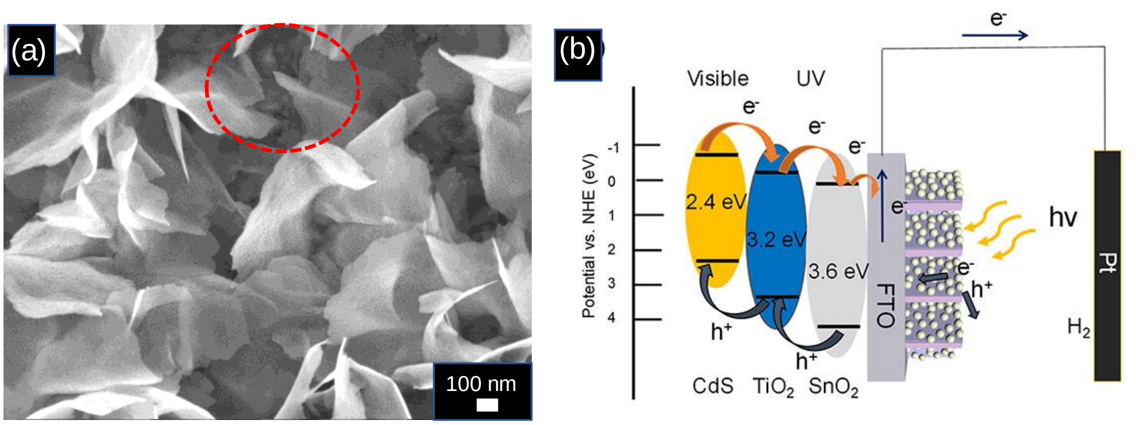

Figure 8.2 (a) The bare FTO substrate existed between adjacent SnO_2 NSs; (b) The heterojunction formation between TiO_2, CdS and SnO_2.

SnO_2 and CdS. As shown in Figure 8.2, a high density of SnO_2 NS could be grown on FTO substrate through the one-step hydrothermal reaction without the use of a seed layer. However, some bare areas of the FTO substrate could not be covered with SnO_2 NSs due to the repulsion between adjacent SnO_2 NSs. The conformal TiO_2 coating around the substrate insulated the FTO substrate from the electrolyte, avoiding the back injection of electrons and thus decreases the serious interface charge recombination. Then enhanced charge separation due to the heterojunction further decreased the bulk charge recombination. Due to the dual role of the TiO_2 thin film, SnO_2 NSs/TiO_2/CdS QDs photoanode shows a higher photocurrent near the onset potential than that of the SnO_2 NSs/CdS QDs reference photoanode. This work indicates the important role of the insulation layer between the FTO substrate and the electrolyte.

8.1.2 The co-existence of Long CdS NRs and Short CdS NRs

Compared to CdS QDs, CdS NRs have better PEC performance due to having direct path for electron transfer and large specific surface. Furthermore, a seed layer was introduced for the growth of WO_3 NSs, avoiding exposure of the FTO substrate to the electrolyte. Thus, in the second work, CdS NRs were grown on WO_3 NSs to form a 2D/1D hierarchical nanostructure. As shown in Figure 8.3, the loading amount and length of CdS NRs

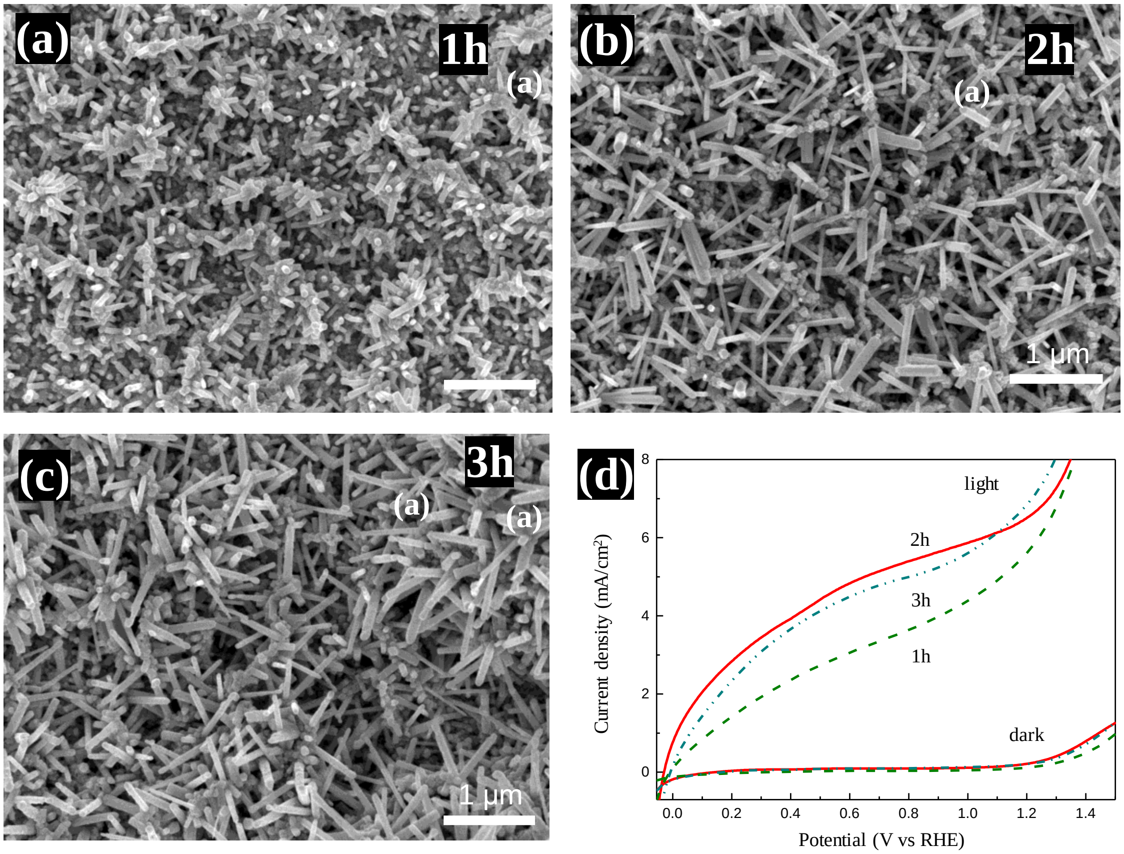

Figure 8.3 Optimizing PEC performance through morphology tuning. (a) Short CdS NRs obtained by 1h hydrothermal growth; (b) The co-existence of long CdS NRs and short CdS NRs obtained by 2h hydrothermal growth; (c) Long CdS NRs obtained by 3h hydrothermal growth; (d) The corresponding photocurrent testing results.

increase with the reaction duration. However, a co-existence of long CdS NRs and short CdS NRs presented a higher photocurrent than long CdS NRs. This is due to the aggregation of long CdS NRs on the top surface of WO_3 NSs, while the co-existence of long CdS NRs and short CdS NRs maintained the sheet structure of WO_3, providing enough space for light penetration to the bottom area. Furthermore, the photostability was improved by the introduction of an ultrathin layer of amorphous TiO_2. This work indicates that the loading amount of the photoactive materials could influence structural morphology and light penetration. Optimizing structural morphology is essential to the improvement of PEC performance.

8.1.3 Optimizing the Charge Collection and Surface Area

3D FTO IOs have high charge collection and multiple light scattering ability. To further increase the surface area, SnO_2 NCs were grown on 3D FTO IOs to form a 3D/0D hierarchical nanostructure. Similar to the previous study, the loading amount of SnO_2 NCs have an impact on the structure of FTO IOs, as shown in Figure 8.4. The excessive loading amount of SnO_2 NCs would disrupt the periodic structure of FTO IOs, blocking the light penetration to the bottom area. Although longer SnO_2 NCs can provide higher specific surface area, the charge transfer resistance also increased. The enhanced PEC performance of the 3D/0D FTO IOs/SnO_2 NCs/TiO_2 hierarchical nanostructure was achieved by simultaneously optimizing the loading amount and length of SnO_2 NCs.

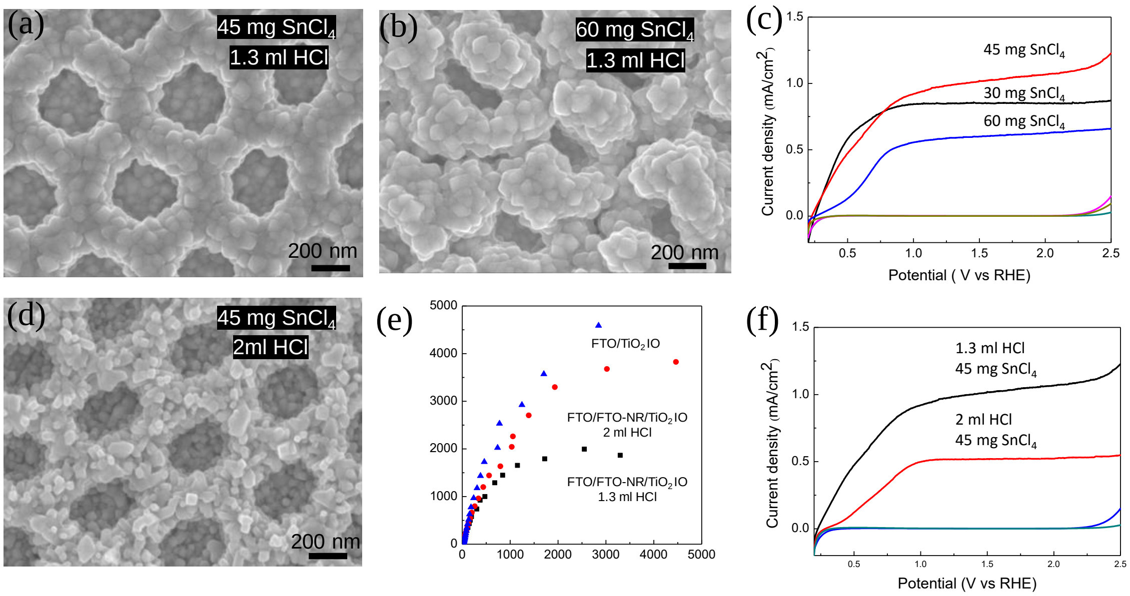

Figure 8.4 Optimizing PEC performance through tuning the loading amount and length of SnO_2 NCs. (a) Short SnO_2 NCs with moderate loading amount; (b) Short SnO_2 NCs with excessive loading amount; (c) Photocurrent testing results corresponding to different loading amounts. (d) Long SnO_2 NCs with moderate loading amount; (e) EIS testing result; (f) Photocurrent testing results corresponding to different lengths.

8.1.4 Enhanced Light Scattering

To further increase the light scattering ability, 1D CdS NRs were grown on 3D FTO IOs to form a 3D/1D hierarchical nanostructure. CdSe clusters were coated on the 3D/1D hierarchical nanostructure to increase more visible light absorption and heterojunction formation with CdS NRs. As shown in Figure 8.5, FTO IOs/CdS NRs/CdSe clusters showed a higher light scattering ability, higher charge collection ability, increased surface area and lower charge recombination. In this hierarchical nanostructure, the co-existence of long CdS NRs and short CdS NRs on FTO IOs were achieved based on the research outcome of the WO_3 NSs/CdS NRs, which is beneficial to the light penetration and thus a higher light scattering inside the hierarchical nanostructure.

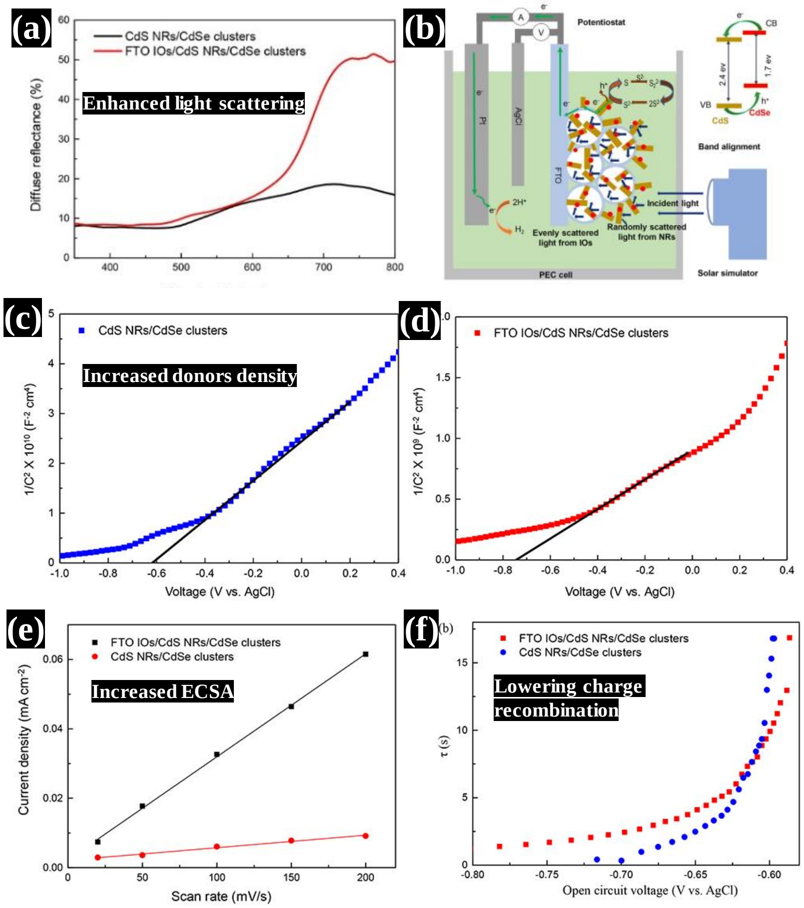

Figure 8.5 (a)-(b) Enhanced light scattering; (c)-(b) Improved conductivity; (e) Increased ECSA. (f) Lower charge recombination.

8.1.5 Conclusion

The water oxidation photocurrent (J_{H2O}) is determined by the charge transfer efficiency (η_{trans}), charge separation efficiency (η_{sep}), and light absorption efficiency (η_{abs}). J_{max} is determined by the bandgap of a semiconductor.

$$J_{H_2O} = J_{max} \times \eta_{abs} \times \eta_{sep} \times \eta_{trans} \quad (1)$$

Based on the above findings, some new factors could be included in the equations.

$$\eta_{abs} \propto surface\ area \times light\ penetration \times light\ scattering \quad (2)$$

$$\eta_{sep} \propto surface\ area \times electron\ mobility \times band\ alignment \quad (3)$$

$$surface\ area \propto {}^{1}/_{light\ penetration} \times {}^{1}/_{electron\ mobility} \quad (4)$$

The growth of nanostructured photoactive materials on the host scaffold could increase the surface. For example, 1D CdS NRs grown on 3D FTO IOs provides a larger surface area than CdS films coated on 3D FTO IOs. Increasing the length of CdS NRs could further enhance the surface area. However, it would exert a negative impact on light penetration or electron mobility. In Chapter 5, the only existence of long CdS NRs occupied all the space between WO_3 NSs, while the co-existence of long CdS NRs and short CdS NRs left enough space for light penetration. Chapter 7 showed that excessive loading of SnO_2 NCs would disrupt the periodic structure of FTO IOs and thus blocking the light penetration. Chapter 7 also showed that the increased length of SnO_2 NCs resulted in the lowering of electrons mobility. Therefore, the strategies that can increase the surface area should be thoroughly examined because they may also influence light penetration or electron collection.

Other strategies, such as band alignment and the enhanced light scattering, could be directly incorporated into the hierarchical structures to improve the charge separation process and light absorption. The main findings summarized above attested that the hypothesis proposed in the first chapter. The construction of hierarchical nanostructures enables the incorporation of different targeted strategies into one structure. After structural optimization, the PEC performance of hierarchical nanostructures can be improved.

8.2 Further Understanding of Hierarchical Nanostructures

In this thesis, four hierarchical host/guest nanostructures have been investigated for PEC applications. These four works involve most of the typical hierarchical structures, including 2D/0D, 2D/1D, 3D/0D and 3D/1D nanostructures, and many commonly used semiconductors, such as SnO_2, WO_3, TiO_2, CdS, and CdSe. Although these hierarchical nanostructures consist of different materials, they can be composed of a host scaffold for electrons transport and photoactive guest materials for light absorption. These four hierarchical host-guest nanostructures can be divided into two types. The first type is the combination of a pristine host scaffold with nanostructured photoactive materials, such as 2D/0D SnO_2 NSs/TiO_2/CdS QDs (Chapter 4), 2D/1D WO_3 NSs/CdS NRs/TiO_2 (Chapter 5), and 3D/1D FTO IOs/CdS NRs/CdSe clusters (Chapter 7). The second type is the construction of a hierarchical host scaffold and then coating with photoactive films, such as 3D/0D FTO IOs/SnO_2 NCs/TiO_2 (Chapter 6).

The introduction of host scaffolds results in the incorporation of different targeted strategies, which significantly improves the PEC performances of guest materials. However, the contribution of each host scaffold is different. The comparison between these host scaffolds could provide some guidance on the development of the optimal host scaffold. In essence, the optimal host scaffold should be suitable for various guest materials, and the most targeted strategies could be incorporated into this optimal hierarchical host/guest nanostructure.

8.2.1 2D/0D Nanostructure Versus 2D/1D Nanostructure

2D SnO_2 NSs with the high surface area is chemically stable in both acid and alkaline solutions, acting as the host scaffold in the 2D/0D SnO_2 NSs/TiO_2/CdS QDs photoanode. However, the direct coating of CdS QDs on SnO_2 NSs would result in severe interface charge recombination, as shown in Chapter 4. WO_3 NSs have a moderate electron mobility and effective visible light absorption. Besides, the pre-coating of the WO_3 seeds layer could avoid the contact of bare FTO substrate with the electrolyte, thus reducing the interface charge recombination. Therefore, WO_3 NSs were selected as the host scaffold in Chapter 5. Besides, plenty of space could be observed between adjacent SnO_2 NSs, indicating that more photoactive CdS materials could be loaded on the host scaffold. However, the reduced space would not favor light penetration or electrolyte immersion. The growth of CdS NRs could increase the loading amount and maintain enough space for light penetration. Thus, the hierarchical 2D/1D WO_3 NSs/CdS NRs/TiO_2 photoanode was fabricated and investigated in Chapter 5.

TiO_2 films have been used in both SnO_2 NSs/TiO_2/CdS QDs and WO_3 NSs/CdS NRs/TiO_2 photoanodes, but their contribution and crystallinity are different. Crystalline TiO_2 films were used to form SnO_2-TiO_2-CdS heterojunctions and insulate FTO substrates from the contact with the electrolyte. In contrast, amorphous ultra-thin TiO_2 films were utilized to enhance the photostability of CdS NRs. The sandwiched TiO_2 films between SnO_2 NSs and CdS QDs significantly increased the photocurrent and decreased the dark current in the low voltage area. However, crystalline TiO_2 films sandwiched between WO_3 NSs and CdS NRs could not achieve the same contribution. Firstly, the dark current of WO_3 NSs/CdS NRs was negligible in the low voltage area, indicating the no contact of bare FTO substrate with the electrolyte. Secondly, due to well-matched band alignment, the WO_3 NSs/CdS NRs photoanode already presented a sharply increased photocurrent in the low voltage area. Although WO_3-TiO_2-CdS heterojunctions could further accelerate the charge separation process, it could not significantly improve the PEC performance of WO_3 NSs/CdS NRs in the low voltage area. On the contrary, amorphous ultra-thin TiO_2 films could also enhance the photostability of SnO_2 NSs/TiO_2/CdS QDs. The weak photostability of CdS is caused by its more negative E_d position than $E(H_2O/O_2)$, rather than its structure.

8.2.2 2D Host Scaffold Versus 3D Host Scaffold

Based on the above comparison, 2D WO_3 NSs exhibited more advantages than 2D SnO_2

NSs as the host scaffold. However, 2D WO_3 NSs are not less stable than 2D SnO_2 NSs, especially in the alkin solution, limiting their application range. FTO IOs provide a possible solution to overcome the dilemmas for WO_3 NSs and SnO_2 NSs. The doping of fluorine could improve carrier density and mobility of SnO_2 without sacrificing the chemical stability. Although the template-assisted fabrication of FTO IOs is more time-consuming than hydrothermal growth of SnO_2 NSs, it can completely insulate the FTO substrate from the electrolyte, avoiding sever interface charge recombination. Besides, the periodic structure of FTO IOs could induce additional strong light-matter interaction, and the high surface area provides by FTO IOs allows the loading of more photoactive materials.

In chapter 7, the primary research is focused on the contribution of 3D FTO IOs host scaffold on the PEC performance of photoactive CdS NRs/CdSe clusters. A lot of experiments, such as UV-Vis, EIS, IPCE, and ECSA, have been performed to understand the role of FTO IOs. These results attested that the introduction of 3D FTO IOs could increase light scattering and charge transport efficiency, thus improving the PEC performance of CdS NRs/CdSe clusters. Besides, the PEC performance of CdS NRs/CdSe clusters and CdS NRs grown on flat FTO have also been measured and shown in Figure 7.9. The CdS NRs/CdSe clusters grown on flat FTO glass presented a higher photocurrent, IPCE, and lower charge transfer resistance than CdS NRs on flat FTO glass. These improvements could be ascribed to the introduction of CdSe clusters on CdS NRs. CdSe could extend the light absorption range of CdS due to its smaller bandgap. At the same time, the CdS/CdSe heterojunctions could further accelerate the charge separation process, as reflected by the lower charge transfer resistance.

Compared to 2D SnO_2 NSs/CdS QDs, some new enhancement strategies, such as increased light scattering, improved charge collection, and decreased interface charge recombination, have been incorporated in the 3D FTO/CdS NRs/CdSe clusters due to the introduction of 3D FTO IOs. Thus, it can be expected that the same photoactive materials coated on 3D FTO IOs would show higher PEC performance than that on 2D SnO_2 NSs.

8.2.3 Pristine Host Scaffold Versus Hierarchical Host Scaffold

The growth of 1D nanostructures on pristine 3D FTO IOs forms the hierarchical photoanode. However, the coating of uniform films on pristine 3D FTO IOs could only create core/shell IOs, rather than building a hierarchical structure. Thus, a hierarchical host scaffold should be firstly constructed, and then the direct coating of photoactive films on such a scaffold could form a hierarchical photoanode. Due to the high feasibility of films, a hierarchical host scaffold could be used to improve the PEC performance of various photoactive materials. Thus, in chapter 7, 3D/0D FTO IOs/SnO_2 hierarchical scaffold has been developed to improve the PEC performance of TiO_2 films.

In chapter 5 and chapter 8, the long CdS NRs showed higher PEC performance than short CdS NRs. However, in chapter 7, short SnO_2 NCs exhibited a better PEC performance than the long SnO_2 NCs. This phenomenon could be explained by the different roles of CdS NRs and SnO_2 NCs. CdS NRs act as the photoactive materials for light absorption. The long CdS NRs could absorb more visible light. In contrast, undoped SnO_2 NCs act as a host scaffold for electrons collection. Short SnO_2 NCs could support a faster charge collection than long SnO_2 NCs. Increasing the electrical conductivity could improve the charge collection ability of long SnO_2 NCs, making it possible for the achievement of efficient light absorption and fast electron collection at the same time.

8.2.4 Advancement of the Thesis

Compared to the published works, this thesis presented some new findings. Hierarchical 2D NSs/1D NRs nanostructures, such as 2D WO_3 NSs/1D Bi_2S_3 NRs,[1] and 2D WO_3 NSs/TiO_2 NRs,[2] have been investigated for the PEC applications. However, the arrangement of 1D NRs on the WO_3 NSs haven't been optimized. In Chapter 5, the co-existence of long CdS NRs and short CdS NRs on the WO_3 NSs achieved the optimization between light penetration and enlargement of surface area. This unique distribution of 1D NRs has also been used for the fabrication of 3D/1D hierarchical nanostructures in Chapter 8. It can be expected that other materials with the same arrangement would show higher

PEC performance. Besides, Pristine FTO IOs have been extensively used as the scaffold, such as FTO IOs/TiO_2 films,[3] FTO/TiO_2/$BiVO_4$ films.[4] However, 3D FTO IOs/0D NCs as a novel hierarchical host scaffold hasn`t been investigated before. The direct coating of photoactive films on hierarchical 3D FTO IOs/0D NCs could form hierarchical nanostructures, but it cannot be achieved on pristine FTO IOs.

8.3 Suggestions For Future Work

8.3.1 Optimal Hierarchical Nanostructures

Based on the results of these four works, the optimal hierarchical nanostructures could be achieved by the construction of a conductive 3D IOs/1D NRs hierarchical host scaffold, such as ATO IOs/ATO NRs, Al-doped ZnO IOs/Al-doped ZnO NRs, followed by the coating of various photoactive films on such host scaffold. Compared to the complex fabrication process for nanostructured photoactive materials, photoactive films could be obtained by a simple sol-gel method. In this hierarchical photoanode, light penetration and scattering can be optimized by tuning the length of 1D NRs. The electron collection ability of 3D IOs/1D NRs hierarchical host scaffold could be improved by elemental doping or oxygen vacancy engineering, which can be reflected by the carrier density and charge transfer resistance measurements. Besides, the band alignment could be achieved by the coating of double-layer films.

8.3.2 Modeling Analysis

Theoretical models could be developed by the finite difference time domain (FDTD) simulations to provide a deep understanding of light penetration and scattering, which can be reflected by the distribution of electric-field intensity $|E|$. Previous literature has reported a relevant model that contains the ZnO NSs decorated with ZnO NRs.[5] Simulation results showed that the light penetration in the bottom zone was improved due to the enlarging the space between two adjacent NSs. However, in this model, the distribution of ZnO NRs was not optimized. Chapter 6 confirmed that the co-existence of CdS long NRs and short NRs could result in a better PEC performance. Thus, the reported model could be modified to investigate the impact of NRs distributions on light penetration and absorption. Besides, Chapter 7 showed that hierarchical 3D FTO IOs/1D CdS NRs could result in multiple light scattering and thus influencing light absorption. Up to date, no models have been developed to describe this 3D/1D hierarchical nanostructure, which could be one of the future works.

8.3.2 Exploring New Materials

CdS is not intrinsically photostable for PEC water splitting. Besides, CdS is toxic due to the release of Cd^{2+} into the solution.[6, 7] Other materials should be developed for the fabrication of hierarchical nanostructures. Zinc indium sulfide ($ZnIn_2S_4$) has been investigated as a visible-light-driven photoanode for PEC water splitting.[8] Through morphology tuning, 2D/0D $ZnIn_2S_4$ NSs/NPs were reported to have better PEC performance than pristine 2D $ZnIn_2S_4$ NSs.[9] However, the photocurrent is still very low, which is around 0.37 mA cm^{-2} at 1.23 V vs. RHE. As shown in Figure 8.6, 2D $ZnIn_2S_4$ NSs were grown on FTO IOs as a hierarchical nanostructure. Through the optimization of reaction duration, 2D $ZnIn_2S_4$ NSs could be coated all over the FTO IOs without disrupting the periodic structure of FTO IOs. The preliminary photocurrent testing results are shown in Figure 8.7, FTO IOs/$ZnIn_2S_4$ NSs prepared with 2 h showed a photocurrent of 1.3 mA cm^{-2} at 1.23 V vs. RHE, which is higher than pristine 2D $ZnIn_2S_4$ NSs.

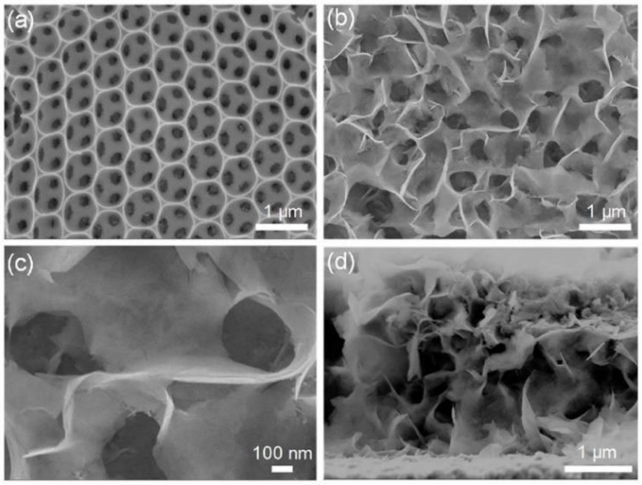

Figure 8.6 Top-view SEM images: (a) FTO IOs; (b)-(c) FTO IOs/ $ZnIn_2S_4$ NSs. (d) Cross section view SEM of FTO IOs/ $ZnIn_2S_4$ NSs.

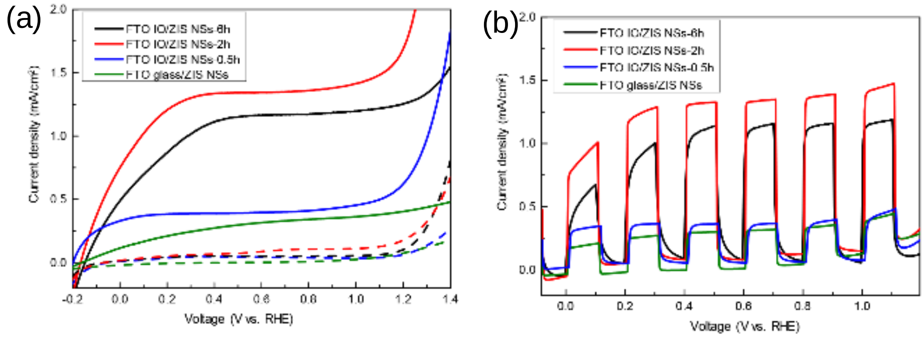

Figure 8.7 (a) Linear sweep voltammetry measurement of FTO IOs/$ZnIn_2S_4$ NSs with different hydrothermal growth duration of $ZnIn_2S_4$ NSs; (b) Linear sweep voltammetry measurement FTO IOs/$ZnIn_2S_4$ NSs under chopped light illumination.

References

[1] Y. Wang, W. Tian, L. Chen, F. Cao, J. Guo, L. Li, *ACS Appl. Mater. Interfaces* **2017**, *9*, 40235-40243.

[2] Q. Zeng, Y. Gao, L. Lyu, S. Chang, C. Hu, *Nanoscale* **2018**, *10*, 13393-13401.

[3] Y. Gun, G.Y. Song, V.H. Quy, J. Heo, H. Lee, K.S. Ahn, S.H. Kang, *ACS Appl. Mater. Interfaces* **2015**, *7*, 20292.

[4] H. Zhang, C. Cheng, *ACS Energy Lett*. **2017**, *2*, 813.

[5] Y. Liu, Z. Kang, H. Si, P. Li, S. Cao, S. Liu, Y. Li, S. Zhang, Z. Zhang, Q. Liao, L. Wang, Y. Zhang, *Nano Energy* **2017**, *35*, 189-198.

[6] B. Zhang, L. Chou, Y. Bi, *Appl. Catal. B-Environ*. **2020**, *262*, 118267

[7] M.A. Alam, C. Wan, X.-Q. Zhao, L.-J. Chen, J.-S. Chang, F.-W. Bai, *J. Hazard. Mater*. **2015**, *289*, 38-45.

[8] B. Xu, P. He, H. Liu, P. Wang, G. Zhou, X. Wang, *Angew. Chem. Int. Ed*. **2014**, *53*, 2339-2343.

[9] M. Zhou, Z. Liu, Q. Song, X. Li, B. Chen, Z. Liu, *Appl. Catal. B-Environ*. **2019**, *244*, 188-196.

APPENDIX: Error Analysis

The transport of photogenerated electrons from the photoanode to the counter electrode forms the photocurrent, which can be used to indicate the PEC performance. Thus, the accurate measurement of photocurrent is essential to the comparison of PEC performance between different photoanodes. The errors of photocurrent measurement come from the testing system and the sample preparation process. A typical photocurrent testing system consists of the solar simulator, electrochemical workstation, wires, and a PEC cell. Before testing, The accuracy of each component should be examined to avoid any artificial errors. The power of the output light varies with the distance between the solar simulator and the PEC cell. At a fixed distance, the intensity can be calibrated to 1 sun illumination (air mass 1.5, 100 mW cm^{-2}) by a standard Si solar cell. After the calibration, the placement of the PEC cell could be determined. If the PEC cell is not placed at this location, the light intensity will not be one sun, resulting in artificial errors. Besides, the PEC cell should be completed isolated from the other light source. The accuracy of electrochemical workstation and wires can be examined by performing a standard cyclic voltammetry testing.

TiO_2 NRs with high chemical stability can be prepared by a simple hydrothermal method, which can be used to do error analysis for photocurrent testing. After the calibration of the testing system, the photocurrent of six TiO_2 NRs prepared with the same conditions was examined. As shown in Figure A.1, TiO_2 NRs showed a photocurrent of 0.639 (S1), 0.653 (S2), 0.578 (S3) 0.603 (S4), 0.629 (S5), 0.603 (S6) mA cm^{-2} at 1.23 V vs. RHE. The average current is 0.6175 mA cm$^{-2,}$ and the standard deviation is 0.0277. The small deviation is caused by the sample preparation process. In a hydrothermal reaction, the FTO substrate is leaned against the wall of the container with a conductive side facing down. The container is sealed in the Teflon-lined autoclave and then transferred to the oven. The different inclination of samples may influence the growth rate and the surface states, which are responsible for the standard deviation. In the practical measurements, the middle curve, such as S5, will be selected to present the overall photocurrent. Furthermore, TiO_2 NRs are chemically stable and have high photostability. Even after the preservation in the dry box for a few months, their photocurrent doesn`t decay obviously. Thus, TiO_2 NRs can be used as a standard sample to check the accuracy of the testing system.

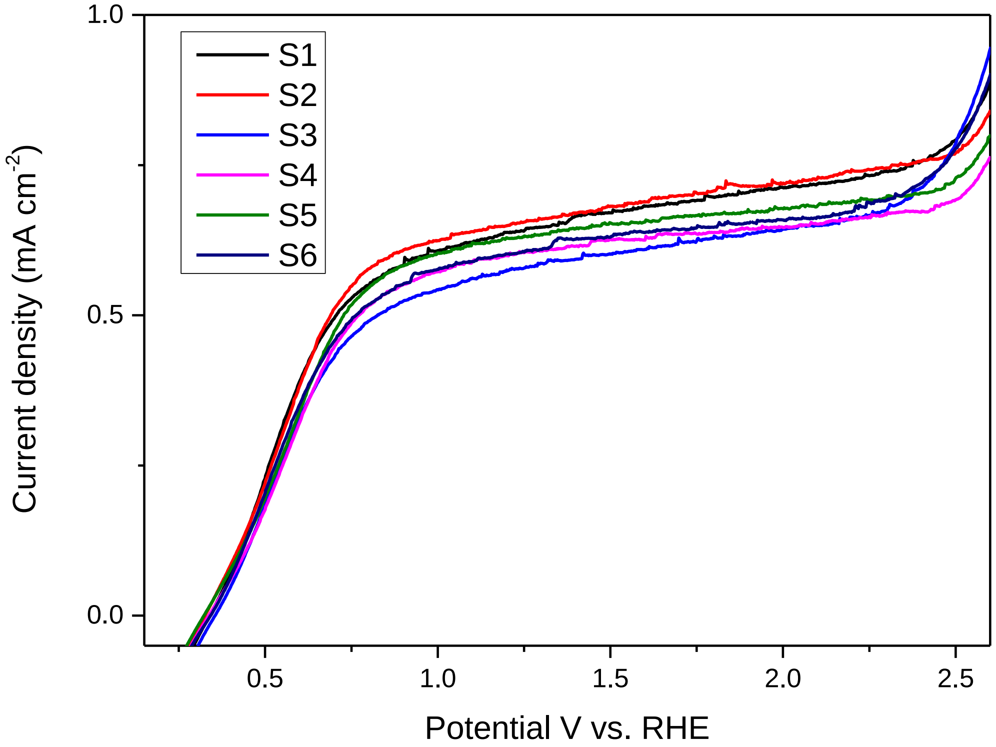

Figure A.1. Photocurrent testing of 6 TiO_2 samples.